

Creation and Experimental Validation of a Numerical Model of a Michelson Interferometer

Maurice M. Stancil

Thesis submitted to the faculty of the Virginia Polytechnic Institute and State University
in partial fulfillment of the requirements for the degree of

Master of Science
In
Mechanical Engineering

J. Robert Mahan, Chair
Brian Vick
Vinh Nguyen

December 9, 2016
Blacksburg, VA

Keywords: Michelson Interferometer, Monte-Carlo Ray-Trace Method, Thermal
Radiation, Geometric Optics

© Maurice M. Stancil, 2016

Creation and Experimental Validation of a Numerical Model of a Michelson Interferometer

Maurice M. Stancil

ABSTRACT

The study whose results are presented here was carried out in support of an ongoing larger effort to investigate and understand the impact of coherence and polarization on the performance of instruments intended to monitor the Earth's radiant energy budget. The visibility of fringes produced by a Michelson interferometer is known to be sensitive to the degree to which the incident light beam is monochromatic. Therefore, the Michelson interferometer has significant potential as a tool for quantifying the degree of temporal coherence of a quasi-monochromatic light beam. Simulation of the performance of an optical instrument using the Monte-Carlo ray-trace (MCRT) method has been shown to be an efficient method for transferring knowledge of the coherence state of a beam of light from one instrument to another. The goal of the effort reported here is to create and experimentally validate an MCRT model for the optical performance of a Michelson interferometer. The effort is motivated by the need to consolidate the knowledge and skills of the investigator in the realm of physical optics, and by the need to make a useful analytical tool available to other investigators in the larger effort.

Creation and Experimental Validation of a Numerical Model of a Michelson Interferometer

Maurice M. Stancil

GENERAL AUDIENCE ABSTRACT

The purpose of this study is to investigate and understand the effects of coherence and polarization on the performance of instruments used to monitor and measure the Earth's radiant energy budget. Coherence and polarization effects need to be understood because they have the potential to produce erroneous radiant energy budget data. Coherence is a measurable parameter describing the correlation between the electrical field phase of a single wave, or between several waves. Polarization is a measurable parameter that describes the orientation of the oscillating electric field of a propagating wave. One of the simplest ways to measure the effects of coherence and polarization is through the use of a Michelson Interferometer. Michelson Interferometers are sensitive machines that are able to produce interference patterns using a single beam of light. The clarity of the produced interference pattern is directly related to the amount of coherence and polarization present in the beam of light under examination. This is why a Michelson Interferometer is perfect for this application. A Michelson Interferometer created in a virtual workspace that utilized the Monte-Carlo ray-trace (MCRT) method has been shown to be an efficient method for transferring knowledge of the coherence state of a beam of light from one instrument to another. The Monte-Carlo ray-trace is an algorithm that facilitates the creation of virtual light rays that behave like natural light rays. The goal in using MCRT is to create and experimentally validate the level of accuracy of the virtual Michelson interferometer. The effort is motivated by the need to consolidate the knowledge and

skills of the investigator in the realm of physical optics, and by the need to make a useful analytical tool available to other investigators in the larger effort.

Acknowledgements

I would like to thank my advisor, Dr. J. R. Mahan, for giving me the opportunity to complete my Mechanical Engineering Master's Degree at Virginia Tech. Without Dr. Mahan's uncompromising patience, wisdom, and guidance I surely would not have made it as far I have.

I would like to thank my committee members, Dr. Brian Vick and Dr. Vinh Nguyen, for serving on my committee.

Lastly, I also want to thank my family for supporting me emotionally and physically during my endeavors at Virginia Tech.

Contents

Chapter 1: Motivation and Goals	1
Chapter 2: Background	3
2.1 The Michelson Interferometer	3
2.2 Operating Principles of a Michelson Interferometer	5
2.3 Coherence	13
2.4 Average Spectrum.....	19
Chapter 3: The Experimental Apparatus, Its Limitations, and the Experimental Procedure	23
3.1 Experimental Apparatus.....	23
3.2 Limitations Inherent to the Experimental Apparatus.....	27
3.3 Procedure	32
Chapter 4: Results of Experimental Effort and Discussion	43
4.1 Experimental Results for Zero Beam Path Length Difference	43
4.2 Experimental Results for a Beam Path Length Difference of One Inch.....	45
4.3 Experimental Results for a Beam Path Length Difference of Two-Inches	48
Chapter 5: Numerical Model of the Michelson Interferometer	50
5.1 Underlying Principle.....	51
5.2 Numerical Implementation	54
Chapter 6: Conclusions and Recommendations	68
6.1 Conclusions.....	68
6.2 Recommendations.....	68
References.....	69

Appendix A: A Brief Biography of Albert A. Michelson	71
Appendix B: Beam A (Mirror 1) Matlab Code.....	75
Appendix C: Beam B (Mirror 2) Matlab Code.....	85
Appendix D: Fringe Intensity Matlab Code.....	95

List of Figures

Figure 2.1: Bruker FTIR 125HR interferometer.	4
Figure 2.2: Schematic diagram of the Michelson Interferometer.	6
Figure 2.3: Schematic diagram of a Michelson interferometer using extended sources and equivalent optics.	9
Figure 2.4: (a) Illustration of constructive interference and (b) destructive interference at the screen.	10
Figure 2.5: Two conventions used for assigning modes to a concentric fringe pattern.	11
Figure 2.6: (a) A stationary wave characterized by having an average intensity that does not vary with time. (b) A non-stationary wave is characterized by having an intensity that varies with time.	15
Figure 2.7: Relationship among the complex degree of coherence $ g(\tau) $, correlation time τ_c , spectral width $\Delta\omega$, and spectral density.	21
Figure 3.1: Photograph of the interferometer with the path of the laser beam indicated and an example of the resulting circular fringe pattern shown as an inset.....	23
Figure 3.2: Schematic diagram of the interferometer depicting the location of the point source and the variation in beam width as it propagates through the device.	24
Figure 3.3: Variation in brightness produced by the laser diode (a) before and (b) after rotation by 90 deg.	26
Figure 3.4: Fringes produced (a) when the neutral-density filter is positioned perpendicular to the optical axis and (b) when the plane of the neutral density filter is rotated slightly with respect to optical axis.	28
Figure 3.5: In (a) the screen is located near the laser source at a vertical position of 22 mm, while in (b) the screen is located far from the laser source and has been translated upward to a vertical position of 20 mm.	30
Figure 3.6: Reproduction rendering of the images in Fig. 3.5. In (a) the screen is near the laser source at a vertical position of 20 mm, while in (b) the screen is farther from the source and has been translated upward about 2 mm to a vertical position of 22 mm	31

Figure 3.7: The fringe patterns observed as the two spots produced by the interferometer are aligned. (a) A strip fringe pattern will be observed if one the mirrors is slightly tilted. (b) An off-centered concentric pattern is observed as the two spots overlap. (c) A pattern of concentric rings is observed as two spots produced by two aligned mirrors are perfectly co-located.34

Figure 3.8: (a) Fringe pattern produced by a mirror with severe tilt from its optical axis. (b) Fringe pattern produced by a mirror that is only slightly tilted from its optical axis.35

Figure 3.9: (a) Fringe pattern corresponding to the measured zero path length difference. (b) Fringe pattern obtained when Mirror 1 nudged slightly from its measured position.36

Figure 3.10: Relationship between beam path length difference and fringe spacing. Fringe pattern corresponding to (a) a relatively large beam path length difference, (b) a relatively small beam path length difference, (c) a beam path length difference of zero.37

Figure 3.11: (a) The board-level camera and its connector cable. (b) The *uEye Cockpit* user interface with key buttons labeled.38

Figure 3.12: Color image after it has been converted to greyscale.40

Figure 4.1: Illumination pattern produced by a Michelson Interferometer with a near-zero difference between the path lengths of the two beams43

Figure 4.2: Histogram corresponding to the image in Fig 4.1 obtained by scanning along the horizontal red line in Fig 4.1.43

Figure 4.3: Histogram corresponding to the image in Fig 4.1 obtained by scanning along the vertical red line in Fig 4.1.44

Figure 4.4: (a) Fringe pattern produced by a Michelson interferometer at a measured beam path length difference of one inch. (b) Corresponding histogram obtained by scanning along the horizontal line Fig 4.4(a).46

Figure 4.5: (a) Fringe pattern produced by a Michelson interferometer at a measured beam path length difference of two inch (b) Corresponding histogram obtained by scanning along the horizontal line Fig 4.5 (a).48

Figure 5.1: Schematic diagram of the basic Michelson interferometer whose performance is modeled in this chapter.49

Figure 5.2: Rays making up Beam A path from the laser to Mirror 1.	54
Figure 5.3: Rays making up Beam A path from Mirror 1 through the Beam Splitter to the FPA.	54
Figure 5.4: Rays making up Beam B path from the laser to Mirror 2	55
Figure 5.5: Rays making up Beam B path from Mirror 2 through the Beam Splitter to the FPA.	55
Figure 5.6: Idealization of the variation with radial position of phase difference between rays from Beam A and Beam B in bin (m, n) on the Focal Plane Array.	57
Figure 5.7: Distribution of phase angle on the Focal Plane Array when Mirror 1 is 2 in. from the Beam Splitter (Beam A).	59
Figure 5.8: Distribution of phase angle on the Focal Plane Array when Mirror 2 is 3 in. from the Beam Splitter (Beam B).	59
Figure 5.9: (a) Experimental image and (b) simulated image for the case of zero path length difference between Beam A and Beam B.	61
Figure 5.10: (a) Experimental image and (b) simulated image for the case of a one-inch path length difference between Beam A and Beam B.	62
Figure 5.11: The upper left-hand corner of Fig. 5.10(b).	64
Figure 5.12: (a) Experimental image and (b) simulated image for the case of a two-inch path length difference between Beam A and Beam B.	66
Figure 5.13: The upper left-hand corner of Fig. 5.12(b).	67

List of Tables

Table 2.1: Relationship between spectral width and coherence time.	21
---	----

Nomenclature

English:

A	Amplitude (<i>Magnitude</i>)
E	Electric-Field complex amplitude ($V m^{-1}$)
d	Distance, Length (m)
g	Complex Degree of Coherence
G	Autocorrelation Function ($W m^{-2}$)
I	Optical Intensity ($W m^{-2}$)
k	Wavenumber (m^{-1})
m	Mode number
l	Length (m)
M_1	Mirror 1
M_2	Mirror 2
n	Variable representing any Integer Number, Index of Refraction, and Unit normal vector
p	Alternative Mode
P	Point in Fig. 2.3
P'	First Virtual Point in Fig. 2.3
P''	Second Virtual Point Fig. 2.3
r	Radius (m), Radial Position (μm)
t	Time (s)
T	Time Interval (s), Total ray length (mm)
V	Fourier Transform of complex wave function of optical wave

x, y, z

Cartesian Coordinates (mm)

Greek:

Δ

Ray Path Length Difference (μm)

δ

Increment of phase angle (rad)

λ

Wavelength (m)

ω

Angular Frequency ($rad \cdot s^{-1}$)

τ_c

Coherence Time (s)

θ

Angle (rad)

$\Delta\theta$

Angular Separation (rad)

ϕ

Phase Angle (rad)

Subscripts:

max

Maximum

0

Initial

T

Truncated, Eq. (2.25)

ν

Frequency (s^{-1})

m, n

Row, Column indices

Constants:

π

Circumference-to-diameter ratio for a circle

$-i$

Imaginary number operator, $\sqrt{-1}$

c

Speed of light in a vacuum, 2.997925×10^8 (m/s)

Chapter 1: Motivation and Goals

The motivation and goals of the research documented in this thesis are established in the current chapter. A potential problem and its possible consequences are identified and an approach for its further study is presented. Mahan, Barki, and Priestly [2016] have posed the question: Can the Earth's radiant energy budget be monitored more accurately by using instruments that are sensitive to the coherence of the incident radiation? At its source, thermal radiation is non-coherent and non-polarized. However, as it is reflected from the Earth's surface and propagates through the Earth's atmosphere (or through any optical train for that matter) it may be partially polarized and/or its degree of coherence may evolve. Radiation emerging from the Earth's atmosphere is fully characterized by its spectral distributions of wavelength, intensity, coherence, and polarization. Consider an instrument consisting of a collimator, mirrors, apertures, filters, and a detector. The relative spectral response (RSR) of such an instrument is normally established through calibration. The calibration source may be narrowband or may have an appropriate radiance when averaged over a finite spectral interval. Practical instruments intended for Earth's radiant energy budget monitoring applications are designed to minimize the effects of polarization and diffraction. However, the degree of coherence and state of polarization of the calibration source may be significantly different from those of the scene the instrument is intended to observe. In this case it may be important to include measures of coherence and polarization. Mahan, Barki, and Priestly [2016] present evidence to the contrary for the case where the dimensions of the detector are at least as large as the smallest aperture. However, diffraction effects associated with coherence

might be increasingly important as the relative size of the detector decreases with respect to the size of the aperture.

It is normally assumed that the RSR is a property of the instrument. However, if the difference in degree of coherence and state of polarization between the scene and a calibration source is significant, then the instrument RSR could be influenced by an amount that increases with this difference.

Therefore, polarization and coherence effects, if not characterized and with acceptable level of precision, can in principle contribute to the overall error allocation for Earth's radiant energy budget monitoring instruments. One approach to studying the influence of coherence on ERB measurements is through modeling. The primary goal of the current effort is to create a numerical modeling environment capable of accurate simulation of the interaction between polarized quasi-monochromatic radiation and various optical components and systems. The approach taken in the effort described in this thesis utilizes *Matlab* as the modeling environment. The model, once created, is benchmarked against the measured performance of an actual Michelson interferometer fabricated for that purpose. The following chapter establishes the theoretical background required to correctly model the propagation of quasi-monochromatic radiation through a Michelson interferometer.

Chapter 2: Background

This chapter introduces the concept of a Michelson interferometer and its operating principles. Appendix A is a brief biographical sketch of its inventor, Albert A. Michelson.

2.1 The Michelson Interferometer

According to Pederotti, Pederotti, and Pederotti [2007], in general any instrument that utilizes the interference principle and displays interference fringes produced by a change in path length can be called an optical interferometer. A minimum requirement to produce interference patterns is partial coherence. (The concept of coherence is explored in Section 2.3.) The physical implications of this requirement are that two matched laser sources can produce interference fringes easily due to their high level of coherence. On the other hand, note that two natural sources would not be able to produce fringe patterns due to their low level of coherence (both spatial and temporal). This does not mean that interference fringes cannot be produced from a natural source. Interference fringes produced from a natural source are possible, for example if a plane with two parallel slits is positioned between the source and screen. In fact, after aligning their interferometer using yellow light from a sodium lamp, Michelson and Morley used white light to obtain their actual measurements.

An interferometer creates interference fringes from coherent (or partially coherent) beams by dividing an initial beam with a beam splitter [Hecht, 2012]. The role of the beam splitter is paramount to understanding the operation of the Michelson interferometer. The role of the beam splitter is described in detail in Section 2.2. The

beam splitter produces two (or in some applications more) beams that follow different paths before being recombined to produce interference fringes.



Figure 2.1: Bruker FTIR 125HR interferometer.

One way to classify interferometers is to distinguish between the mechanisms used to divide the initial beam. In this classification system, interferometers are classified as either amplitude-divided or wavefront-divided. A wavefront-splitting interferometer divides a light wavefront emerging from two pinholes or narrow slits thereby forming spatially coherent light. After causing the two parts of the wavefront to propagate along different paths, they are allowed to recombine on a screen [Hecht, 2012]. An amplitude-splitting interferometer uses a partial reflector to divide the amplitude of the incident wave into separate beams which are later recombined. Another way to classify interferometers is based on the number of beams they use. For example, the Michelson interferometer produces interference fringes created from two beams, while the Fabry-

Perot interferometer utilizes multiple reflections between two closely spaced partially silvered surfaces. Part of the light is transmitted each time the light reaches the second surface, essentially producing interference fringes created by multiple offset beams [Hecht, 2012].

2.2 Operating Principles of a Michelson Interferometer

The Michelson interferometer has played a significant role in physics. As described in Section 2.1, this instrument was used to confirm special relativity and to invalidate the luminiferous aether theory. It has also been used to detect and measure hyper-fine structure in line spectra, and to provide a substitute standard for the meter in terms of a given number of wavelengths of light [Livingston, 1973]. A modern adaptation based on Michelson's design is currently manufactured by the Bruker Corporation. The author of this thesis has used the *Bruker FTIR 125HR interferometer* shown in Fig. 2.1 to measure the spectral variation of surface optical properties and filter transmissivity spectra.

Figure 2.2 is a schematic diagram of a Michelson interferometer adapted from Pederotti, Pederotti, and Pederotti [2007]. Beam A from a partially coherent light source enters the interferometer and is incident to a Beam Splitter where it is divided into two beams of approximately equal strength. Beam B is deflected toward a plane mirror M_1 , thereby undergoing a 180-deg phase shift, while Beam C continues on without phase shift to a second mirror M_2 . In Fig. 2.2 the Beam Splitter consists of a thin glass substrate whose front surface is coated with a dielectric layer. However other beam splitter concepts are commonly used, as discussed below. Upon arrival at mirrors M_1 and M_2 Beams B and C are reversed and their phase shifted by 180 deg, after which they are

designated Beam B' and Beam C', respectively. When Beam B' and Beam C' arrive at the Beam Splitter one-half the power of each beam is transmitted and the other half is reflected, with the reflected part once again undergoing a 180-deg phase shift. The transmitted half of B'', now designated Beam B'', and the reflected half of Beam C', designated Beam C'', have both undergone a total of 360-degree of phase shift since entering the interferometer.

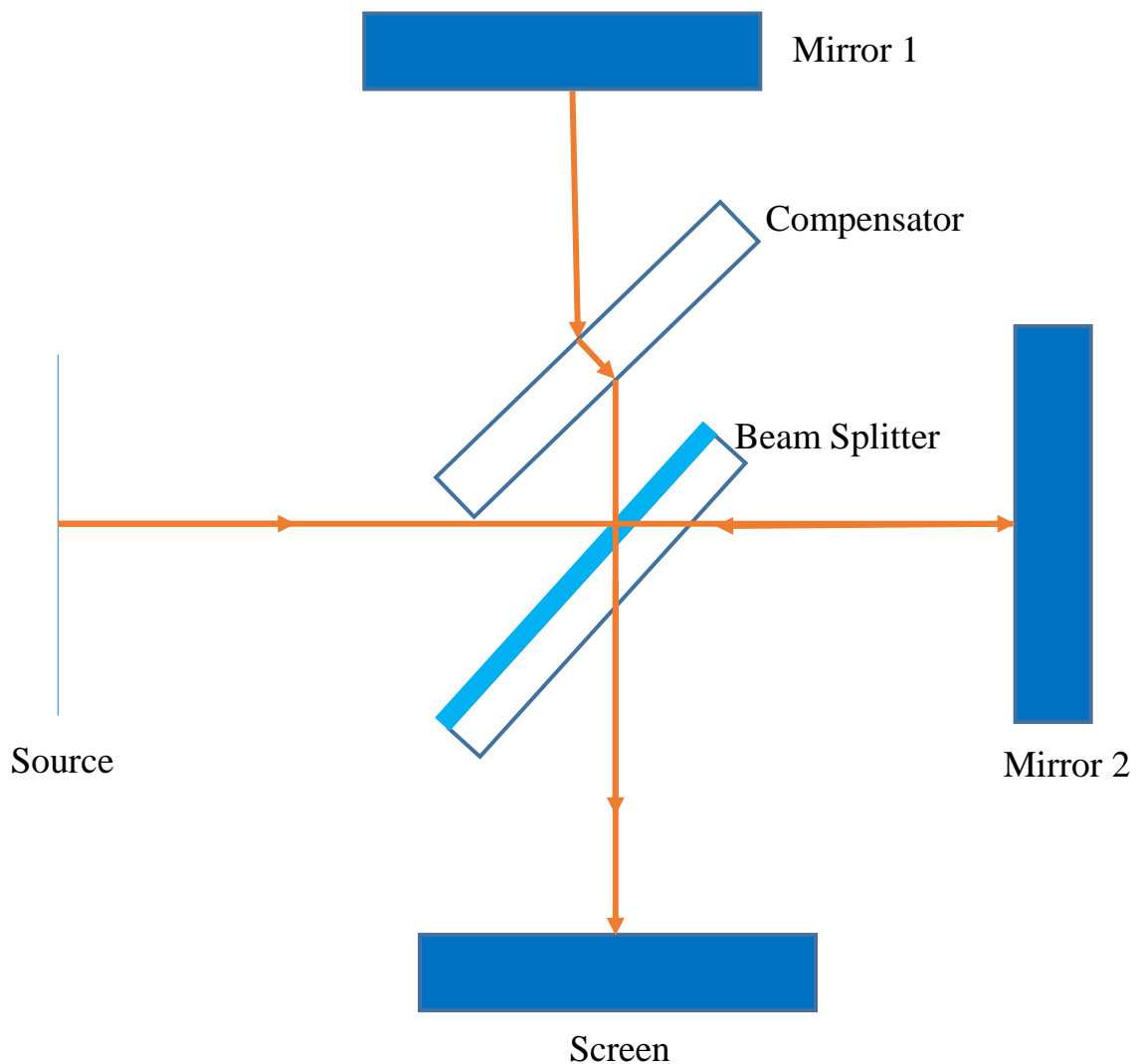


Figure 2.2: Schematic diagram of the Michelson Interferometer.

Livingston [1973] points out that an inherently zero path length difference between the two beams is desirable in some applications. In order to achieve this in the interferometer illustrated in Fig. 2.2, both Beam B and Beam B' pass through a compensator plate of the same thickness and having the same refractive index as the glass backing of the Beam Splitter, while both Beams C and C' have passed through the glass backing of the Beam Splitter. Also, Beams B'' and C'' have both passed one time each through the same thickness of the beam splitter substrate. Thus, any phase shift or deflection associated with the formation of Beams B'' and C'' due to passage through the glass elements of the interferometer are the same and thus are effectively compensated for. Any remaining variations in the path length difference that are still present after the compensator plate has been installed can be easily removed by slightly rotating it.

One commonly used alternative to the Beam Splitter illustrated in Figure 2.2 is the pellicle [https://www.thorlabs.com/NewGroupPage9.cfm?ObjectGroup_ID=898]. A pellicle beam splitter consists of an extremely thin nitrocellulose-membrane typically on the order of a few micrometers thick and therefore very fragile. The absence of a glass substrate to mechanically support the membrane eliminates chromatic dispersion related to the wavelength-dependent optical constants associated with glass. Another alternative is the *block*, or *cube*, beam splitter [Steel, 1983]. As implied by its name, the cube beam splitter consists of two half-cubes of a suitable transparent material. The half-cubes are fabricated by slicing a whole cube diagonally. A dielectric coating is applied to the diagonal face of one of the half cubes and the two halves are then rejoined to form a whole cube with the dielectric coating forming a thin layer passing diagonally through its center. A photograph of a cube beam splitter appears in Fig. 3.1 of this thesis. The

advantage of a cube, or block, beam splitter over the thin plate beam splitter illustrated in Fig. 2.2 is that the need for a compensator plate is obviated since all rays passing through or deflected by the cube beam splitter travel the same distance through the encapsulating cube material. The advantage of the cube beam splitter over a pellicle in applications where chromatic dispersion is not an issue is clearly its strength and durability. In the current effort, a laser is used as the light source, and so chromatic dispersion is not an issue.

Now if the distance between the Beam Splitter and the mirror M_1 is different from the distance between the Beam Splitter and the mirror M_2 , then Beams B'' and C'' will arrive at the screen out of phase with each other. Such a path length difference is commonly achieved by displacing one of the mirrors normal to its plane while allowing the other to remain fixed. Upon arrival at the screen the two beams will combine either constructively or destructively to a degree depending on their total path length difference traveled by individual rays making up the two beams. This interference phenomenon, considered in more detail elsewhere in this thesis, produces a fringe pattern on the screen whose visibility depends on the degree to which the incident Beam A is temporally coherent. The topic of coherence is taken up elsewhere in this chapter, but in general coherence in the present context is related to the degree to which the beam is monochromatic. The coherence, and thus the visibility of the interference fringes, decreases as the departure from monochromatic ideal increases. For example, if Beam A is produced by a laser whose output has been passed through a condensing lens, the coherence will be very high and the interference fringes will be quite apparent.

Investigation of the principles of operation of the Michelson interferometer is the subject of this thesis. The degree to which these principles can be successfully applied in a Monte-Carlo ray-trace environment to simulate the operation of an actual Michelson interferometer will be taken as the measure of success for this thesis.

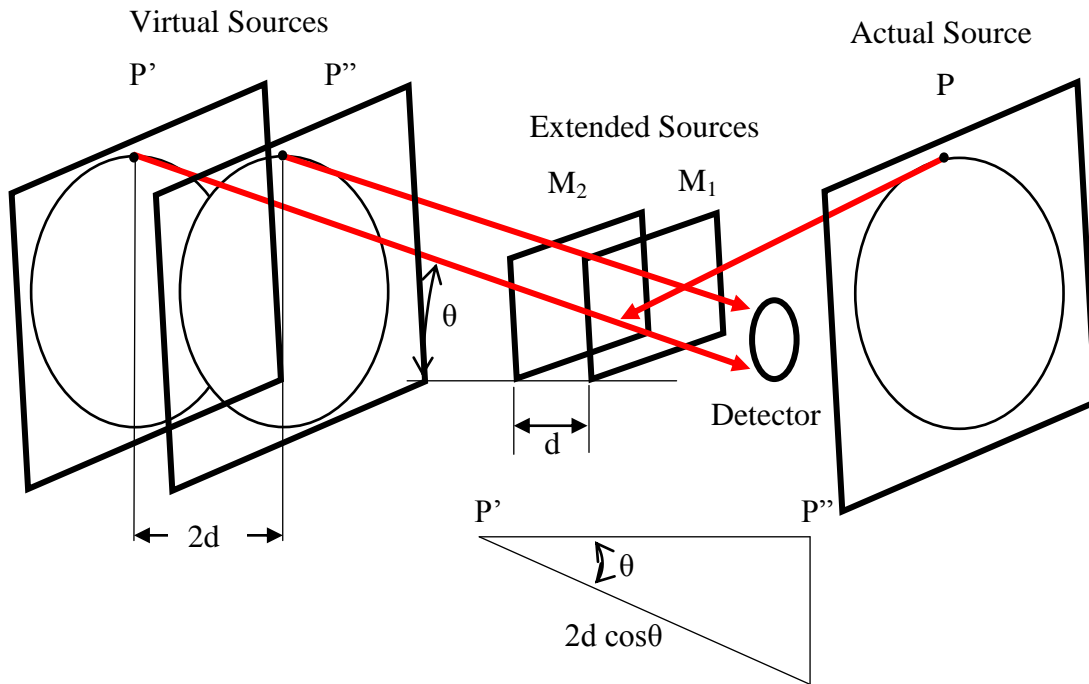


Figure 2.3: Schematic diagram of a Michelson interferometer using extended sources and equivalent optics.

The net *path length difference* Δ for the two beams produced by the interferometer is given by

$$\Delta = 2d \cos \theta, \quad (2.1)$$

where θ is the angle of a beam relative to the optical axis and d the distance along that axis. The angle θ is determined by a lens positioned between the (collimated) source and the Beam Splitter. The path length difference relationship in Eq. (2.1) is easier to visualize using the extended sources and equivalent optics illustrated in Fig. 2.3. Figure

2.3 displays a detector in the Michelson interferometer that observes two virtual extended sources created by the two mirrors, which are displaced by a specified distance from each other and at a specified angle θ from the optical axis. If the path length difference is an integer multiple of the wavelength, i.e. if

$$\Delta = m\lambda , \quad (2.2)$$

where m is an integer, the interaction of the two beams will produce constructive interference.

Constructive interference occurs when two waves are in phase when incident to the screen, as illustrated in Fig. 2.4(a). Also, the two beams will constructively interfere at each $\lambda/2$ translation of the mobile mirror assuming the path length difference is shorter than the coherence length of the source. *Coherence length* is defined and discussed in detail elsewhere in this chapter. Briefly, it is the length along a wave for which the phase remains correlated (coherent); i.e. for which knowledge about the wave at one end of the correlation length can be used to make meaningful predictions about the wave at the other end of the correlation length. If the path length difference is

$$\Delta = n\lambda/2 , \quad (2.3)$$

where n is an integer, the interaction of the two beams will produce destructive interference. *Destructive interference* occurs when two waves are 180 deg out of phase, as illustrated in Fig. 2.4(b).

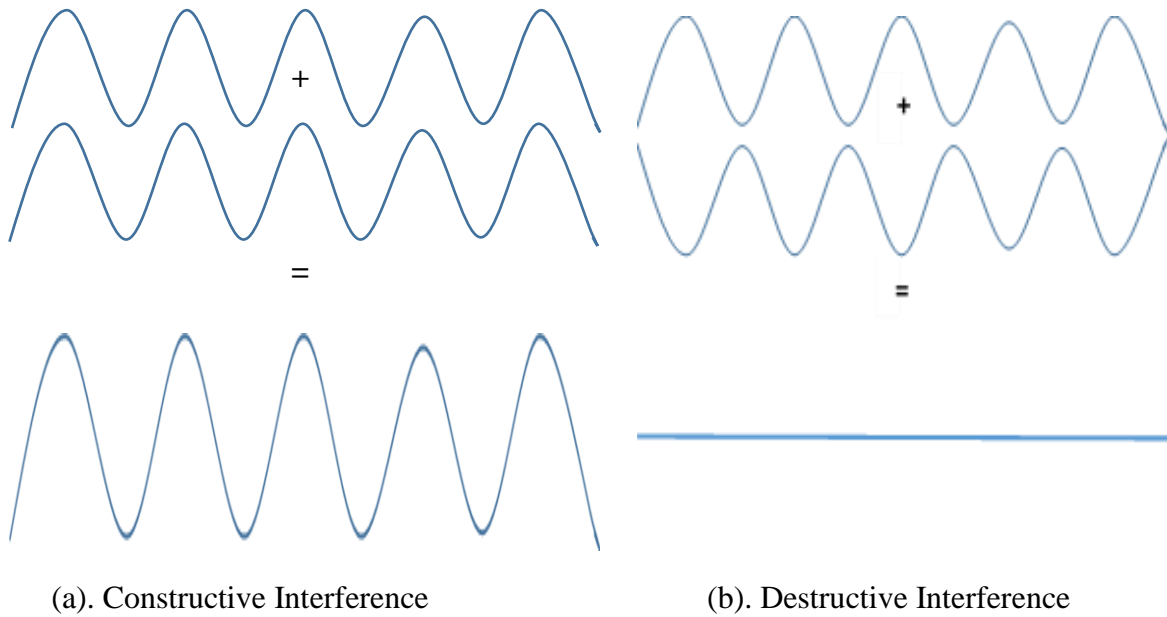


Figure 2.4: (a) Illustration of constructive interference and (b) destructive interference at the screen.

If the two beams from a point source have the same amplitude I_0 , the intensity of the fringe system of concentric circles on the screen is

$$I/I_0 = \frac{1}{2} [1 + \cos(\delta)] \quad (2.4)$$

and

$$\delta = 2\pi\Delta/\lambda . \quad (2.5)$$

The corresponding equation for dark fringes is

$$2d\cos\theta + \lambda/2 = (m + \frac{1}{2}) \lambda . \quad (2.6)$$

If the center fringe is dark as seen in Fig. 2.5 then the *order* can be written as

$$m_{\max} = 2d/\lambda , \quad (2.7)$$

where m_{\max} is a large integer. Local dark fringes decrease in order from the center as $\cos\theta$ decreases from its maximum value of unity. For example, if the center spot of a

concentric fringe pattern has an order of 100, the neighboring dark fringe would have an order of 99.

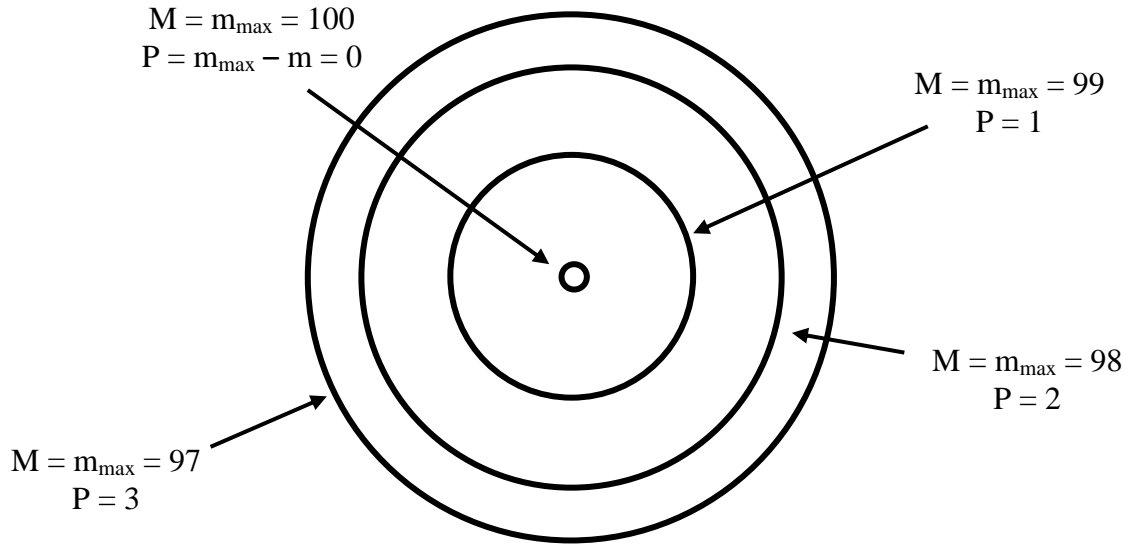


Figure 2.5: Two conventions used for assigning modes to a concentric fringe pattern.

Equation 2.6 indicates that changes in distance for a given point (where θ is constant) will correspond to a gradual change in m values. As the distance is varied the fringe pattern will appear to move depending on whether the path length difference is increasing or decreasing. The interference pattern will appear to reverse as one of the two plane mirrors is continuously moved through the point of zero path difference. Equation 2.6 implies that the *angular separation* $\Delta\theta$ between the fringes constituting the interval Δm must increase as the mirror spacing distance decreases. This reasoning leads to

$$|\theta| = \lambda \Delta m / 2d \sin \theta \quad , \quad (2.8)$$

which implies a wider separation of fringes for smaller path length differences [Pederotti, Pederotti, and Perorrti, 2007]. When a mirror traverses a normal distance Δd , the number Δm of fringes passing at or near a point is given by

$$\Delta m = 2\Delta d/\lambda \quad . \quad (2.9)$$

2.3 Coherence

Coherence, or more specifically quasi-coherence, is a key condition for the appearance of interference patterns [Serway and Vuille, 2015]. The theory of optical coherence is the study of the statistically random variations in radiation expressed in the form of correlation functions [Steel, 1983]. It is important to note that variations can be associated with either the light source, the medium through which the light is propagating, or both. Among other things, variations due to both the source and the medium are caused by molecular collisions. A natural source consists of a large number of atoms radiating at different frequencies, with randomly differing phases, and in randomly different (i.e. diffuse) directions. Molecular collisions in natural light sources can cause variations in the electric field constituting a beam. In various mediums (including fluids, atmospheres, real surfaces, and transparent solids such as common glass in the visible part of the spectrum) molecular collisions can cause scattering or wave front distortions.

It is convenient to classify light into three categories: coherent, incoherent, and quasi-coherent. *Quasi-coherence* is a state defined by a mixture of coherence and incoherence, and is the most appropriate characterization of natural light. *Coherent light* is characterized by the ability to predict its phase observed at time t at point x at a future time $t + 2x/c$ at the same point [Verydeyen, 1995]. Conversely, *incoherent light* is

characterized by the inability to predict its phase observed at time t at point x at a future time $t + 2x/c$.

The *coherence time* τ_c can be defined as the net delay that can be inserted in the wave train and still obtain interference [Verdeyen, 1995]. The relevance of this definition to the current effort is that the delay τ between the arrival of the two beams at the screen of an interferometer is proportional to the relative displacement of the two mirrors M_1 and M_2 ; i.e. $\tau = \Delta/c$, where c is the speed of light. As reported by Wolf [2007], interference fringes can be observed only when

$$\Delta\tau_c \leq 2\pi/\Delta\omega \quad , \quad (2.10)$$

where $\Delta\omega$ is the frequency band in radians per second. Since light in a given uniform medium travels at a fixed velocity c , the coherence length is simply c times the coherence time.

This establishes that an interferometer can in principle be used to measure coherence. Completely coherent light is an unachievable idealization often used in optical pedagogy. According to Wolf [2007], completely coherent light, also called *monochromatic light*, can be represented by the relation

$$E(\mathbf{r}, t) = \text{Re}[E(\mathbf{r})e^{-i\omega t}] \quad , \quad (2.11)$$

where $E(\mathbf{r})$ is the complex amplitude or field, and $E(\mathbf{r}, t)$ is the three-dimensional vector field representing the true amplitude or field. The symbol E as used here can represent either the electric field or magnetic field amplitude. Equation (2.11) represents the solution of a time-harmonic electric field, a field that oscillates in time at fixed angular frequency ω . This wave function is perfectly periodic and predictable, and therefore coherent [Wolf, 2007]. The unpredictable variations of incoherent light can best be

described using statistical techniques [Steel, 1983]. According to Selah and Teich [2007], the use of statistical averaging allows for the acquisition of information needed to distinguish random waves from one another. This averaging determines the value of non-random measures, which can act as an optical fingerprint used to distinguish the type of optical source.

To within a dimensional constant the intensity of coherent light is

$$I(\mathbf{r},t) = |E(\mathbf{r},t)|^2 . \quad (2.12)$$

For natural light $E(\mathbf{r}, t)$ and $I(\mathbf{r}, t)$ are random functions of time and position. Due to this randomness, a time-averaged intensity

$$I(\mathbf{r},t) \sim |E(\mathbf{r},t)|^2 \quad (2.13)$$

must be used. Continuing Selah and Teich's [2007] formalism, we imagine that a wave is produced repeatedly under the same conditions yielding a different wave function each time. These wave functions are then averaged so that the average intensity at each point and time can be acquired. If the statistical averages implied by Eq. 2.13 do not vary in time, the wave is said to be *statistically stationary*. Care must be taken not to confuse stationarity with constancy. If the average intensity varies in time and space, then the wave is said to be *non-stationary*. Figure 2.6 depicts both a stationary wave and non-stationary wave and their characteristic average intensity. An estimate of the intensity of a stationary wave can be obtained by time-averaging over a sufficiently long time period. This is mathematically equivalent to averaging a large number of several iterations of the wave, as described above.

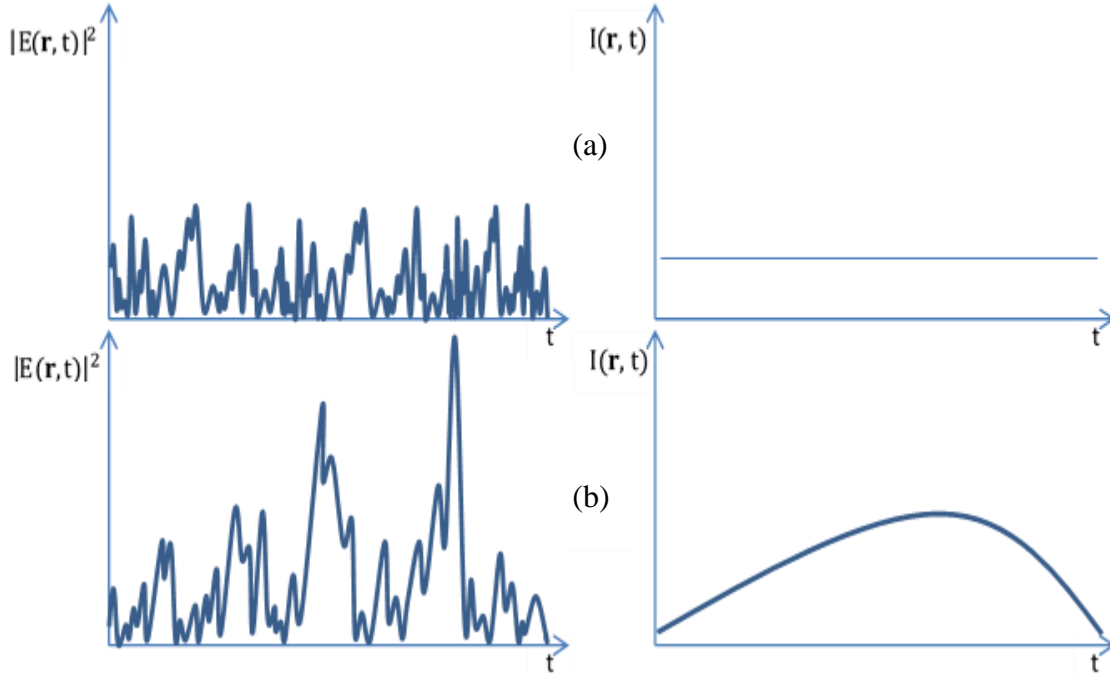


Figure 2.6: (a) A stationary wave characterized by having an average intensity that does not vary with time. (b) A non-stationary wave is characterized by having an intensity that varies with time.

The local intensity in the case of a stationary wave is

$$I(\mathbf{r}) \sim \lim_{T \rightarrow \infty} \frac{1}{2T} \int_{-T}^T |E(\mathbf{r}, t)|^2 dt, \quad (2.14)$$

where T is the time interval over which the wave is said to be stationary.

Once again following Selah and Teich's [2007] development, in a stationary wave random variations in $E(\mathbf{r}, t)$ (when \mathbf{r} is fixed) can be averaged over a time scale which can be considered the memory of the random function. The function will appear smooth within its memory time, but time-varying over a longer time period. A quantitative measure of this temporal behavior is established by defining a statistical average known as an *autocorrelation function*. This function describes the extent to which the wave function varies at two instants of time separated by a specified time delay. Thus, the correlation time is the characteristic time scale of the process that underlies the

generation of the wave function. The autocorrelation function $G(\tau)$ of a stationary complex random function $E(t)$ (suppressing \mathbf{r} in the notation since the position is fixed) is the time average of the product of the complex conjugate of the wave function $E^*(t)$ and the wave function itself corresponding a time delay τ ; that is,

$$G(\tau) = E(t)^*E(t + \tau). \quad (2.15)$$

Continuing with Selah and Teich's [2007] development, the autocorrelation function is also known as the *temporal coherence function*. For a given value of τ , $E(t)$ and $E(t + \tau)$ may be temporally correlated to a certain degree. The phase of the product $E(t)^*E(t + \tau)$ is the angle between the phasors $E(t)$ and $E(t + \tau)$. A wave function $E(t)$ is said to be temporally correlated in a range of time delay τ for which these phasors have a constant relationship. This constant relationship means the product of the phasor $E(t)^*E(t + \tau)$ has a preferred direction in complex (Real, i Imaginary) space, and its magnitude (the temporal coherence function) $G(\tau)$ will be non-zero. During a time when temporal coherence is not present, $E(t)$ and $E(t + \tau)$ will be uncorrelated. This means that product of phasor $E(t)^*E(t + \tau)$ will not have a preferred direction and so the angle between the phasors will vary randomly between 0 and 2π . Furthermore, the average $G(\tau)$ will equal zero. In the special case where $E(t)$ is the electric field strength (V/m) the corresponding intensity is, to within a dimensional constant,

$$I = G(\tau) \text{ with } \tau = 0. \quad (2.16)$$

This means that the temporal coherence function contains information about both the intensity $I = G(0)$ and the degree of coherence of stationary light. A measure of coherence that is insensitive to the intensity is provided by the normalized autocorrelation function,

$$g(\tau) = \frac{G(\tau)}{G(0)} = \frac{\langle E(t) * (t+\tau) \rangle}{\langle E(t) * (t+\tau) \rangle} . \quad (2.17)$$

Still following Selah and Teich [2007], the normalized autocorrelation function is also known as the *complex degree of temporal coherence*. The magnitude of this function must lie between zero and unity, i.e.

$$0 \leq |g(\tau)| \leq 1 \quad (2.18)$$

The quantity $|g(\tau)|$ is a measure of the coherence between $E(t)$ and $E(t + \tau)$. When $E(t) = Ae^{(j\omega_0 t)}$ with constant amplitude A (monochromatic light), the complex degree of coherence can be written

$$g(\tau) = \exp(j\omega_0\tau) , \quad (2.19)$$

where j is $\sqrt{-1}$. Monochromatic light can be represented

$$g(t,\tau) = A(t)\exp[j\omega_0(t + \tau)] . \quad (2.20)$$

In this case $|g(\tau)| = 1$ for all τ . This means that $E(t)$ and $E(t + \tau)$ are completely correlated for all time delays. Natural light is generally not monochromatic and so $|g(\tau)|$ is usually observed to decrease from its maximum value of $|g(0)| = 1$ with increasing τ as fluctuations become increasingly uncorrelated.

Consider the case where the magnitude of the coherence function $|g(\tau)|$ decreases monotonically with time delay τ , which is generally the case with quasi-periodic time series. Then the *coherence time* τ_c is defined as the same time delay required for the magnitude of the coherence fluctuation to reach a prescribed value such as $1/2$ or $1/e$. Figure 2.6 depicts the magnitude of the complex degree of coherence for sections of the wave train that exhibit a short or long coherence time. For $\tau < \tau_c$ the variations are said to be strongly correlated, and for $\tau > \tau_c$ the variations are said to be

weakly correlated. According Selah and Teich [2007], the *power-equivalent width*, which can be written as

$$\tau_c = \int_{-\infty}^{\infty} |g(\tau)|^2 d\tau, \quad (2.21)$$

is commonly used as the definition of coherence time. The coherence time of monochromatic light is infinite since $|g(\tau)| = 1$ everywhere. Referring to Wolf [2007], the coherence of a beam of light is characterized by its coherence length

$$l_c = c\tau_c. \quad (2.22)$$

The light wave in question is said to be effectively coherent if the coherence length is much greater than all optical path-length differences encountered [Selah and Teich, 2007].

2.4 Average Spectrum

In consonance with the formalism of Selah and Teich [2007], observation of $E(t)$, even if that were possible, would not readily provide useful information about the spectral nature of the light source being used. In order to extract useful statistical information about a light source, a Fourier decomposition of $E(t)$ must be utilized. The amplitude of the spectral component having angular frequency ω is given by the Fourier transform written as

$$V(\omega) = \int_{-T/2}^{T/2} E(t) \exp(-2\pi j\omega t) dt, \quad (2.23)$$

where

$$T = \frac{\int_{-\infty}^{\infty} f(t)^2 dt}{\int_{-\infty}^{\infty} f(t) dt}. \quad (2.24)$$

In Eq. (2.24) $f(t)$ is a so-called window function that defines a window of time during which $E(t)$ is observed. The average energy per unit area of those components with frequencies in the interval between ω and $\omega + d\omega$ is $\langle |V(\omega)|^2 \rangle d\omega$, so that $\langle |V(\omega)|^2 \rangle$

represents the spectral density of light (energy per unit area per unit frequency). Ideally a true stationary function contains infinite energy; therefore, the power spectral density is a more useful concept. To determine that density, first the energy spectral density of $E(t)$ is analyzed over a time-width T by finding the truncated Fourier transform

$$V_T(\omega) = \int_{-T/2}^{T/2} E(t) \exp(-2\pi j\omega t) dt. \quad (2.25)$$

Second, the energy spectral density $\langle |V(\omega)|^2 \rangle$ is determined. The *power spectral density* (PSD) is defined as the energy per unit time $(1/T)\langle |V_T(\omega)|^2 \rangle$. The time window can now be extended to infinity by taking the limit $T \rightarrow \infty$, resulting in an expression for the PSD,

$$S(\omega) = \lim_{T \rightarrow \infty} \frac{1}{T} \langle |V_T(\omega)|^2 \rangle. \quad (2.26)$$

Note that the PSD is considered to be non-zero only for positive frequencies because $E(t)$ is defined in a manner such that $|E(t)|^2$ is inherently positive. Continuing the development, $S(\omega) d\omega$ represents the average power per unit area contained by frequencies between ω and $\omega + d\omega$. This means that $S(\omega)$ is the intensity spectral density ($W \cdot s/m^2 \cdot r$), otherwise known as *the spectral density*. The total average intensity is the integral

$$I = \int_0^{\infty} S(\omega) d\omega. \quad (2.27)$$

The autocorrelation function $G(\tau)$ and spectral density are a Fourier transform pair related by

$$S(\omega) = \int_{-\infty}^{\infty} G(\tau) \exp(-j\pi\omega\tau) d\tau. \quad (2.28)$$

The spectrum of light is centered on a central frequency ω_0 . The Fourier-transform relationship between $S(\omega)$ and $G(\tau)$ reveals that their widths are inversely proportional. This implies that a broad-spectrum source has a short coherent time and narrow spectrum source has a long coherence time. Figure 2.7 summarizes the relationship between the

complex degree of coherence, the spectral width, and the spectral density. This relationship indicates that a long coherence time is characteristic of a narrow spectral width. However, a short coherence time is characteristic of wide spectral width. For monochromatic light, $G(\tau) = \exp(j\omega_0 \tau)$ and the spectral density $S(\omega) = I\delta(\omega - \omega_0)$ contains a single frequency ω_0 , where δ is a delta function or impulse function. This implies $\tau_c = \infty$ and $\Delta\omega = 0$. Filters are often used to reduce the spectral width, effectively increasing the coherence time of the light source. However, this increase in coherence comes at the loss of light energy. The spectral width can be treated as the full width of $S(\omega)$ at half its maximum value or FWHM. The relationship between the coherence time and spectral width depends on the spectral profile, as illustrated in Table 2.1.

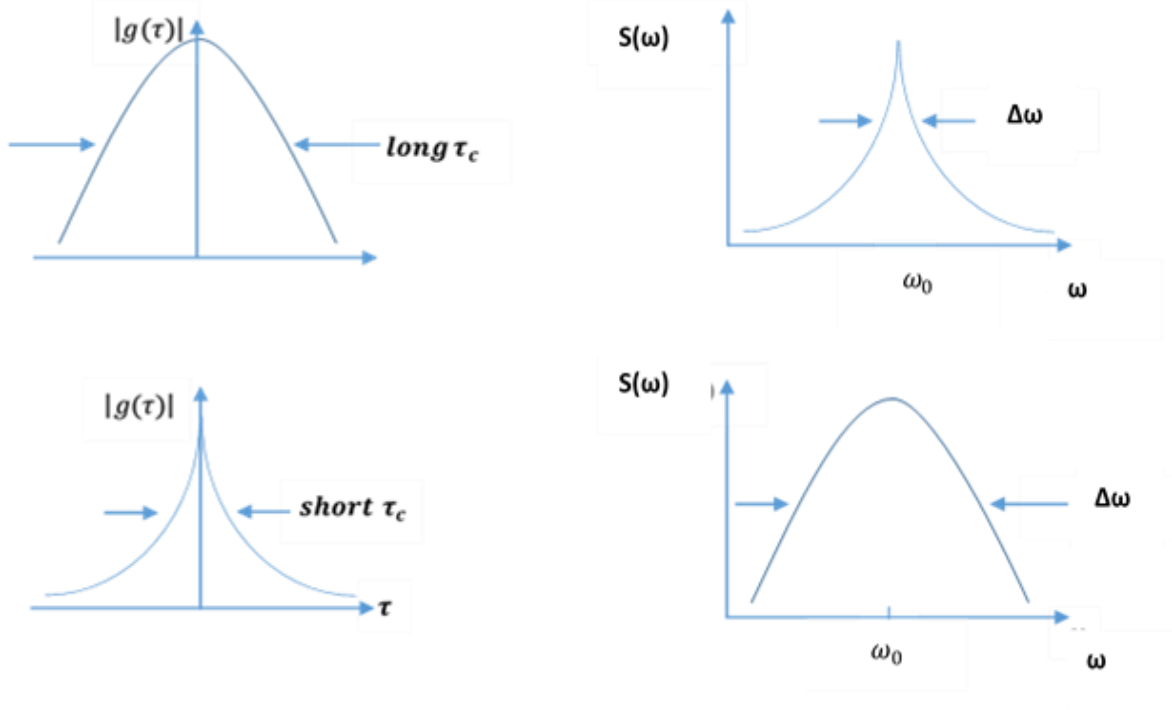


Figure 2.7: Relationship among the complex degree of coherence $|g(\tau)|$, correlation time τ_c , spectral width $\Delta\omega$, and spectral density.

Table 2.1: Relationship between spectral width and coherence time.

Spectral Density	Rectangular	Lorentzian	Gaussian
Spectral Width	$\frac{1}{\tau_c}$	$\frac{1}{\pi\tau_c} \approx \frac{0.32}{\tau_c}$	$\frac{\sqrt{2\ln 2/\pi}}{\tau_c} \approx \frac{0.66}{\tau_c}$

Another convenient definition of spectral width is

$$\Delta\omega_c = \frac{\left(\int_0^\infty S(\omega) d\omega\right)^2}{\int_0^\infty S^2(\omega) d\omega}. \quad (2.29)$$

This means that regardless of the profile the spectral width is

$$\Delta\omega = 1/\tau_c, \quad (2.30)$$

Chapter 3: The Experimental Apparatus, Its Limitations, and the Experimental Procedure

This chapter provides a detailed description of the experimental apparatus, its inherent limitations, and the experimental procedure required to assess its performance.

3.1 Experimental Apparatus

With the exception of minor modifications described in this chapter, the interferometer used in this effort was assembled from a kit purchased from *Thorlab Industries* (Part No. EDU-BT1). A photograph of the experimental apparatus appears in Fig 3.1, which also shows an example of the circular fringe pattern it produces. Where appropriate the following description is based on English units of measure rather than the preferred SI units. This is a practical consideration based on the fact that the optical bench hole pattern is laid out in inches rather than in millimeters. Also, specifications for all of the optical components are cited in English units. The apparatus consists of a *Thorlab* 532-nm laser diode module (Part No. CPS532-C2) held in a *Thorlab* small V-clamp with PM3 clamping arm (Part No. VC1). These components are attached to a *Thorlab* 2-in.-long post (Part No. TR2) using a 1/4-in. set screw. The laser assembly is mounted to a *Thorlab* 2-in. post holder (Part No. PH2) which in turn is mounted on the edge of a *Thorlab* 12- x 12- x 1/2-in. aluminum breadboard with 1/4-in.-20 (M6) taps (Part No. MB12), using a *Thorlab* 1- x 3- x 3/8-in. post holder mounting base (Part No. BA1). The first *Thorlab* 32-mm thick, 1-in. diameter protected aluminum mirror, Mirror 1, (Part No. ME1-G01) is installed in a *Thorlab* kinematic mount for 1-in. diameter optics (Part No. KM100).

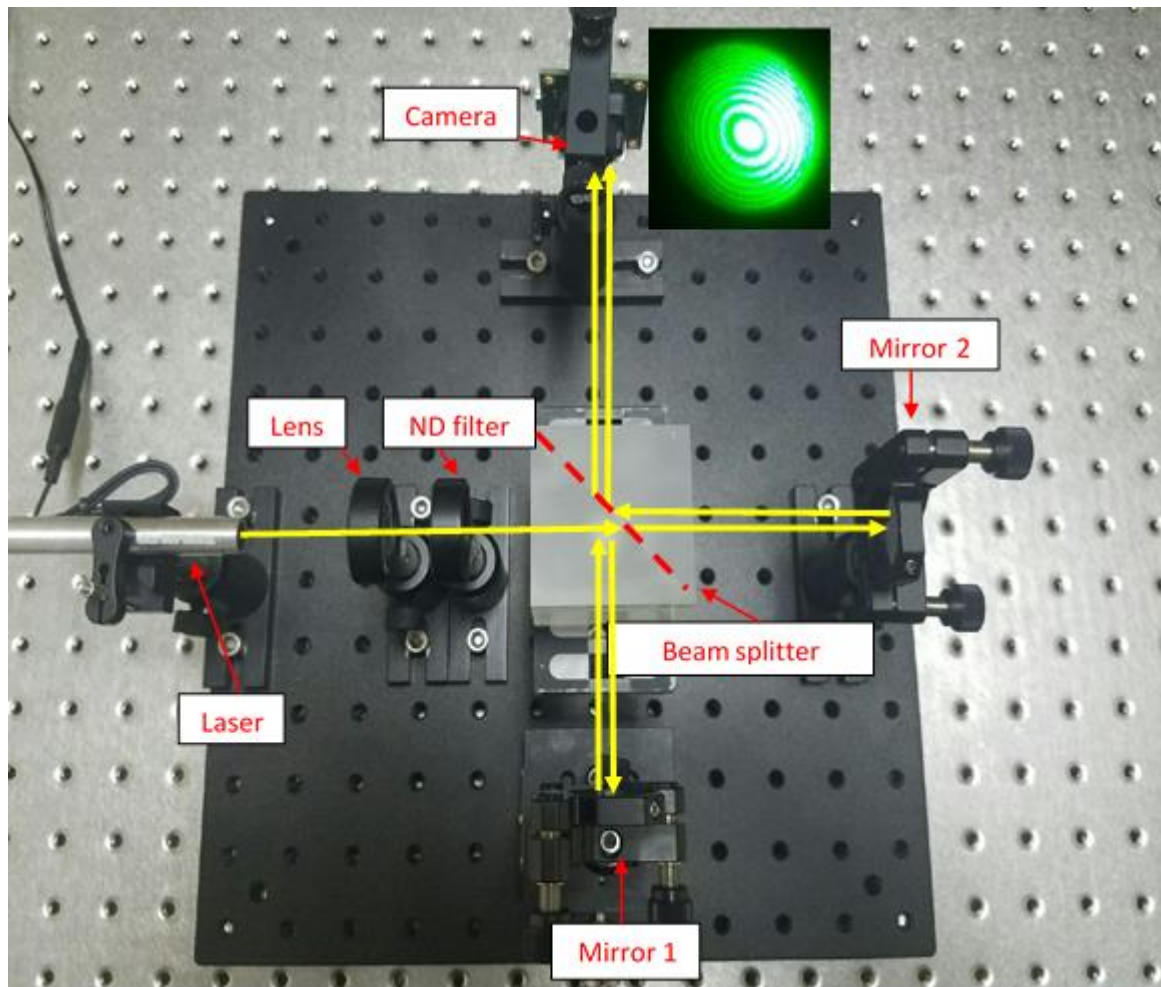


Figure 3.1: Photograph of the interferometer with the path of the laser beam indicated and an example of the resulting circular fringe pattern shown as an inset.

These components are attached to a *Thorlab* 2-in.-long post (Part No. TR2) using an 8-32 (Part No. M4) set screw. The mirror assembly is retained by a *Thorlab* 2-in. post holder (Part No. PH2) and secured with a *Thorlab* 1- x 3- x 3/8- in. post holder mounting base (Part No. BA1) and is positioned on the optical breadboard 10-in. from the laser assembly. Mirror 1 is positioned in a manner that allows the reflected beam to be directed at the aperture of the laser module. A *Thorlab* 2- x 3- x 3/8-in. post holder mounting base (Part No. BA2) is used as a stage and is attached using a 1/4-in. cap screw to a *Thorlab* 2-

in.-long post (Part No. TR2) which is supported by a *Thorlab* 2-in. post holder (Part No. PH2). The stage assembly is mounted to the optical breadboard using a *Thorlab* 1- x 3- x 3/8-in. (Part No. BA1). The stage assembly is positioned between the laser and the first mirror, 6.0 in. from the laser and 4.0 in. from the mirror. An *Edmund Optics* 50-mm VIS, non-polarizing cube beam splitter (Stock No. 49-009) is positioned on the stage assembly so that the beam is split at a 90-deg angle. A second mirror assembly, Mirror 2, (identical to the first) is mounted onto a *Thorlab* 1/4-in. travel single-axis translation stage with an end-mounted adjuster screw, 4.0 in. from the beam splitter. Mirror 2 is positioned at a 90-deg angle from the laser module and the first mirror.

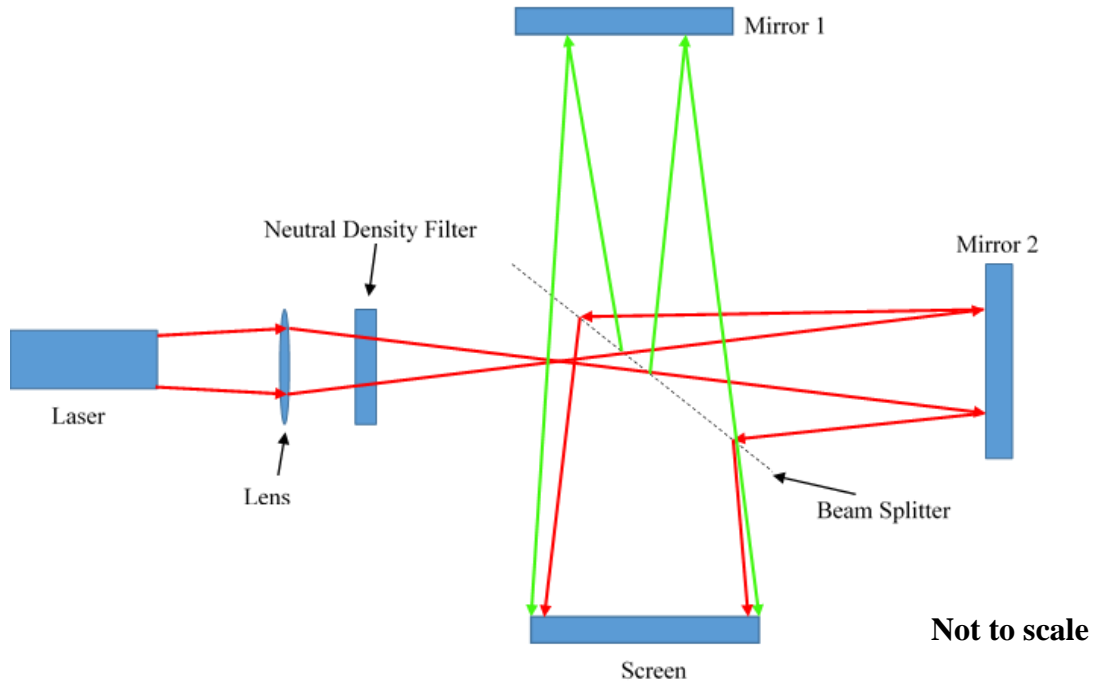


Figure 3.2: Schematic diagram of the interferometer depicting the location of the point source and the variation in beam width as it propagates through the device.

Figure 3.2 is a schematic representing the evolution of the beam waist during propagation. The variation in beam diameter is a result of focusing the beam rather than collimating it. The schematic diagram also shows the location of the focal point.

An *Edmund Optics* EO-10012C ½-in. CMOS Color USB 2.0 Board-Level Camera (Stock No. 68-089) is retained in an *Edmund Optics* 25-mm Bar-Type Lens/Filter Holder (Stock No. 55-529). These components are attached to a *Thorlab* 2-in.-long post (Part No. TR50/M) using a 1/4-in. set screw. The camera assembly is then clamped by a *Thorlab* 2-in. post holder (Part No. PH2) and mounted to the optical breadboard with a *Thorlab* 1- x 3- x 3/8-in. post holder mounting base (Part No. BA1). The camera is mounted on the end of the optical breadboard facing Mirror 1, 6.0 in. from the beam splitter. The camera is positioned such that the beam falls as nearly as possible on the center of the aperture.

Camera operations are controlled with the program *uEye Cockpit*, which was downloaded from the *Edmunds Optic* website. The 1.0-in. diameter N-BK7 Bi-Convex Lens $f=75.0$ mm (Part No. LB1901) focusing lens is held by a lens mount for 1.0-in. diameter optics and secured with a SM1 threaded retaining ring (Part No. SM1RR). These components are attached to a to a 2.0-in. long post (Part No. TR2) and placed in a 2-in post holder (Part No. PH2). The lens assembly is then mounted midway between the laser and the beam splitter, 2.0 in. from both. An *Edmunds Optics* OD 2.5 VIS, 25-mm diameter reflective neutral-density filter (Stock No. 43-811) is mounted in a *Thorlab* lens mount for 1.0-in. optics (Part No. LMR1) and secured with a SM1 threaded retaining ring (Part No. SM1RR). The neutral-density filter is required to attenuate the beam intensity to a level does not saturate or damage the board level camera. These components are then

attached to a *Thorlab* 2.0-in.-long post (Part No. TR2) and placed in a *Thorlab* 2-in. post holder (Part No. PH2). The filter assembly is then mounted directly behind the lens, 1.0 in. from the beam splitter.

3.2 Limitations Inherent to the Experimental Apparatus

It is important to note that neither this experimental apparatus nor its components are high-precision, high-performance devices. This limitation reduces the precision of the apparatus, thereby increasing the uncertainty in the data. This results in significant departures from theory of the data obtained. The relative low cost of this experimental apparatus implies that it is mainly intended for demonstrations as opposed to high-precision measurements. This section explores the specific limitations of the apparatus.

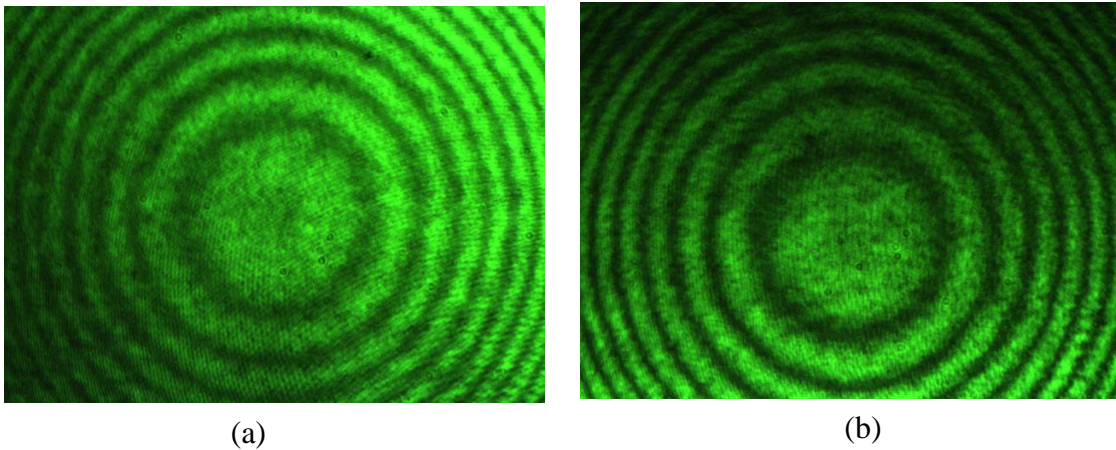


Figure 3.3: Variation in brightness produced by the laser diode (a) before and (b) after rotation by 90 deg.

The laser diode provided by *Thorlab* is not a high-performance, high-precision device. The fringe pattern on the screen suffers from two different imperfections: (1) astigmatism and (2) nonuniformity of background intensity. The beam spot produced is not perfectly circular nor is it symmetrical. Astigmatism has a negligible effect on the

interpretation of data obtained. The *Thorlab* laser diode is also not uniformly bright across the beam. This feature is captured in Fig 3.3, which shows fringe patterns for two different rotations of the laser in its clamp. Image 3.3(b) depicts a vertical variation in brightness when the laser diode is rotated approximately 90 deg from its original orientation in Fig. 3.3(a). The variation in brightness affects the visibility of the fringe pattern.

As already pointed out in reference to inset in Fig 3.1, the fringes produced by a Michelson interferometer form a concentric pattern of light and dark rings. The non-uniformity of the laser diode reduces the visibility of the fringes, which makes it difficult for image processing software to clearly distinguish the boundary between a dark fringe and a neighboring light fringe. This inability to distinguish light from dark contributes to a reduction in visibility of the fringes.

The interferometer kit did not arrive with a neutral density filter; however, one is required to protect the board-level camera. Without the filter, saturation and perhaps even damage to the camera may occur. The problem with incorporating a reflective neutral density filter in this experimental apparatus is that it produces reflections that lead to secondary illumination of the camera objective. This resulting noise further reduces the ability to distinguish between light and dark fringes.

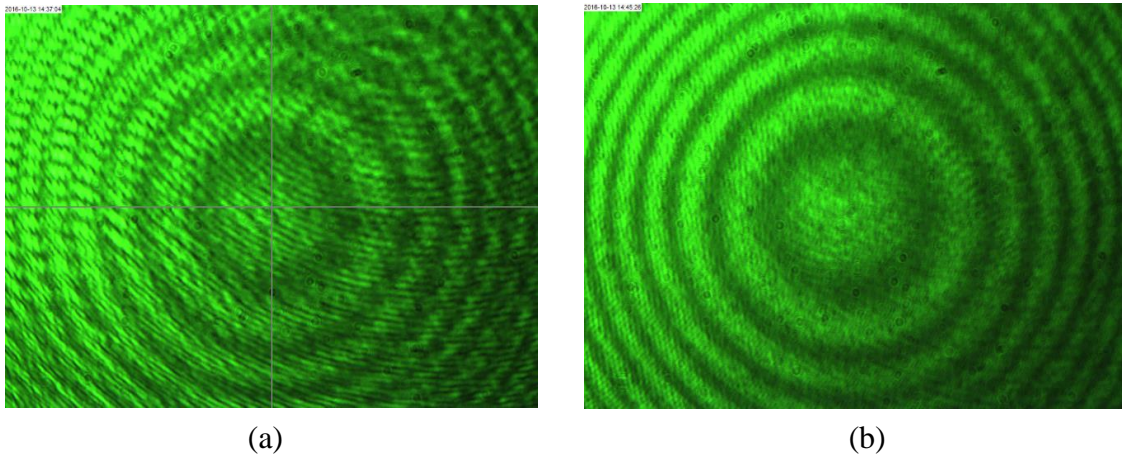
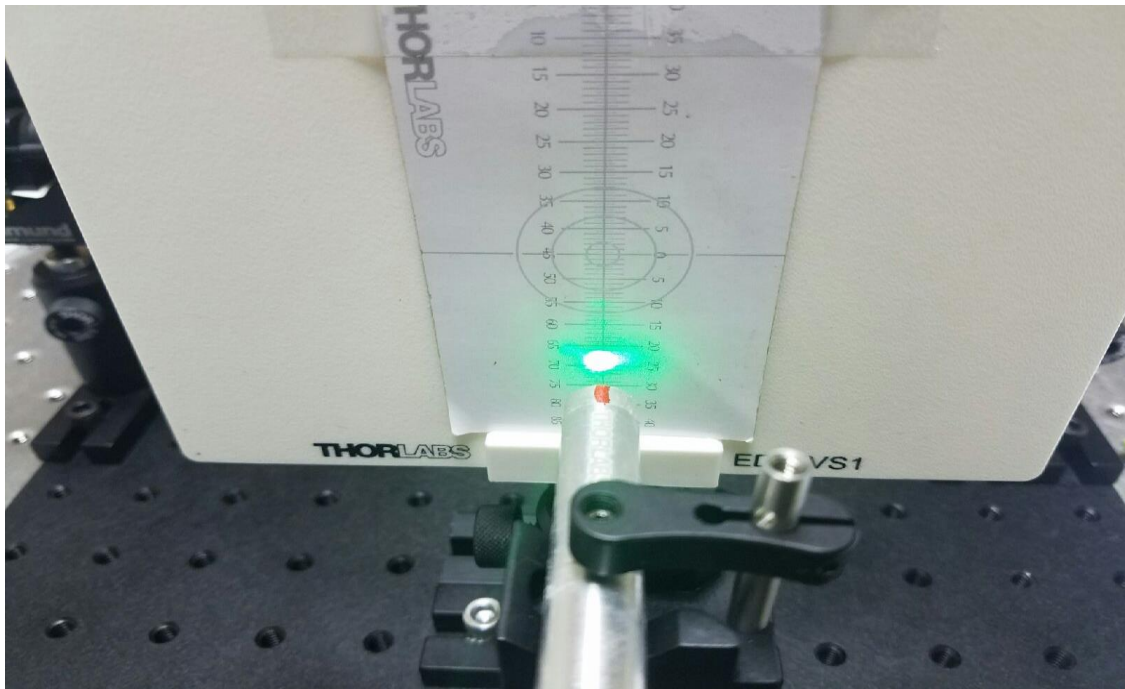


Figure 3.4: Fringes produced (a) when the neutral-density filter is positioned perpendicular to the optical axis and (b) when the plane of the neutral density filter is rotated slightly with respect to optical axis.

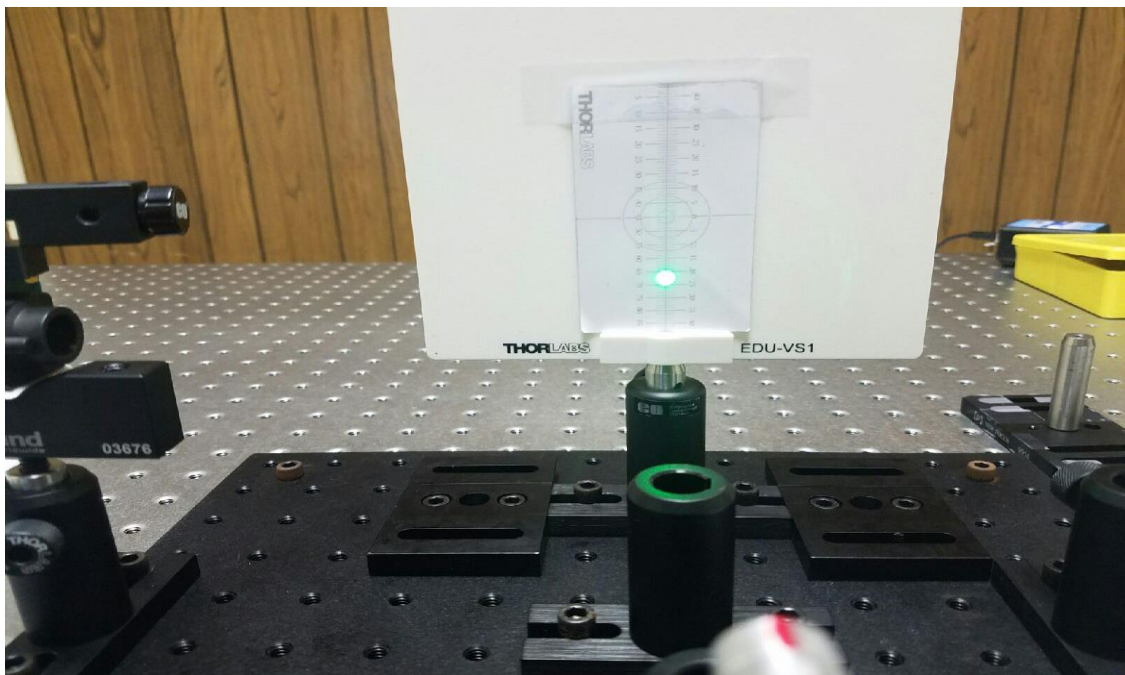
As shown in Fig. 3.4(a), when aligned normal to the optical axis, the neutral density filter creates unintended reflections between components which are revealed as secondary concentric patterns in the background of the primary concentric pattern. This causes a reduction in resolution and an increase in noise. In Fig. 3.4(b), the neutral-density filter has been rotated only a few degrees to a position where the background interference is much less evident than in Fig. 3.4(a). This is because rotating the filter off the optical axis causes the reflections to be deflected out of the optical path, thus preventing secondary background interference patterns. A high level of coherence is necessary to produce a distinct fringe pattern, but this requirement makes the apparatus sensitive to unwanted reflections.

The optical axis of the laser diode is also not positioned well within its enclosure. This is a manufacturing flaw that further exacerbates the low-precision, low-performance nature of the laser diode itself. The error in optical alignment is evident

when the laser module is placed in its V-clamp holder, which is parallel to the optical bread-board. Normally the center line of a laser beam, when perfectly parallel to the mounting surface, should depart very little in its vertical and horizontal directions as it propagates. If the laser center line is observed to deflect from optical axis, it is either misaligned in the V-clamp holder or the diode must be misaligned within its enclosure. A misalignment error in the V-clamp is manageable, but encapsulation misalignment cannot be easily addressed since the module is not intended to be opened by the user. Figures 3.5 and 3.6 both demonstrate that the beam varies in a vertical direction by about 2-mm as the beam propagates, while holding alignment in the horizontal plane.



(a)



(b)

Figure 3.5: In (a) the screen is located near the laser source at a vertical position of 22 mm, while in (b) the screen is located far from the laser source and has been translated upward to a vertical position of 20 mm.

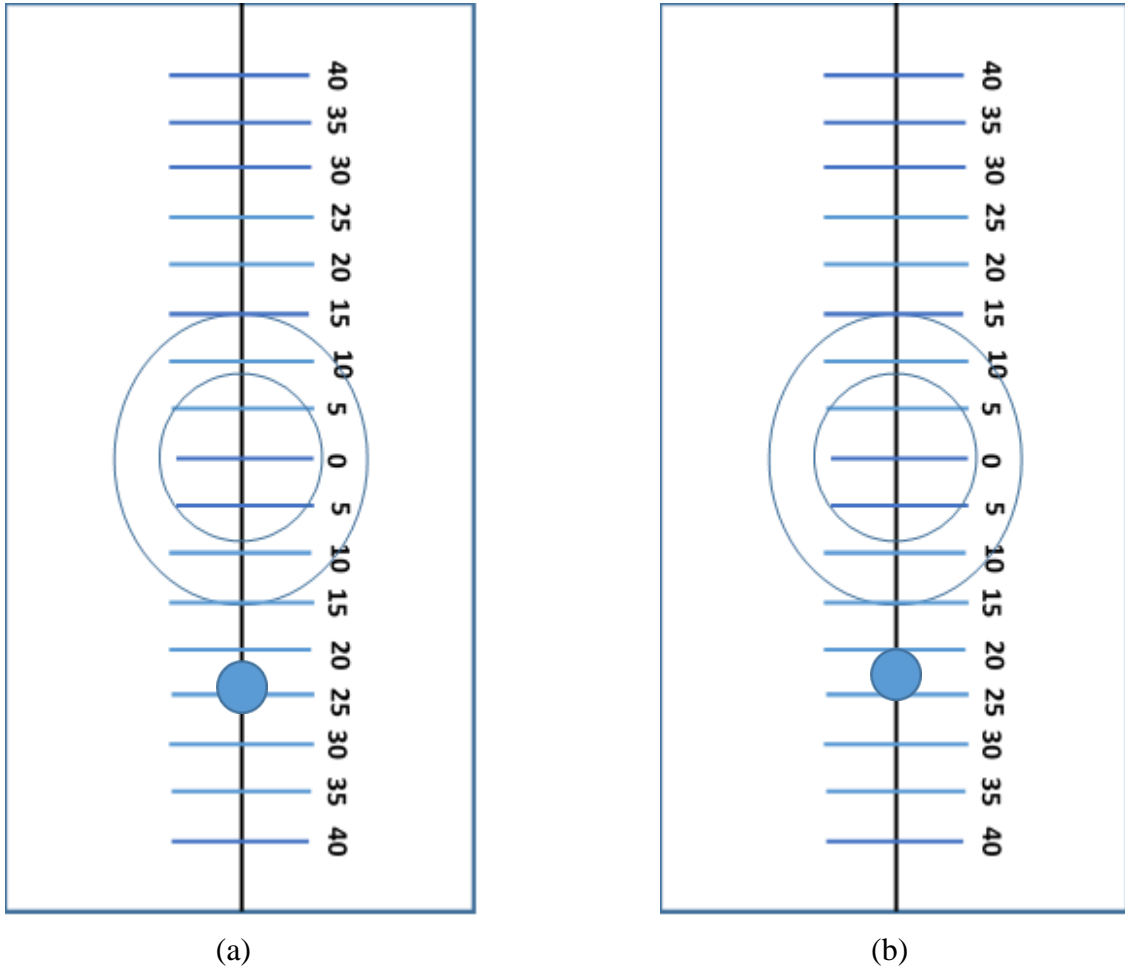


Figure 3.6: Drawing of the images in Fig. 3.5. In (a) the screen is near the laser source at a vertical position of 20 mm, while in (b) the screen is farther from the source and has been translated upward about 2 mm to a vertical position of 22 mm.

Figures 3.5 and 3.6 show that as the distance from the focal point of the condensing lens to any other optical element evolves, the point where the beam intersects the optical element is displaced vertically.

3.3 Procedure

This section describes the step-by-step procedure for obtaining the measurements reported in this thesis.

Step 1. Switch on the laser. Allow the laser to remain on for 30 to 40 min before obtaining measurements. This time delay allows for stabilization of the laser. After the allotted time has passed, note the shape and uniformity of the intensity of the output beam spot. These features are important because they affect the characteristic shape and intensity of the resulting interference pattern. In this step success is limited by the fact that the laser beam spot is not perfectly circular and its intensity is nonuniform.

Step 2. Alignment of the Mirror 1 requires a dimly illuminated room because of the limited intensity of the laser diode. It is also helpful to have available a small white card. The texture of this card needs to be sufficiently rough to diffuse the laser light so that strong stray radiation does not reach the eyes of operator. The small size of the card assists in locating the beam when fine precision is necessary. The nature of the V-clamp holding the laser diode is such that its vertical alignment is held at the most parallel position possible with respect to the optical breadboard. Holding the white card, while blocking half the beam in the path between the neutral density filter and the Beam Splitter, it may be confirmed that that beam spot leaving the neutral density filter and then striking the beam splitter is centered. Mirror 1 is adjusted in its post at a height that allows the output beam spot from the Beam Splitter to strike the center of the mirror. The mirror is attached to a kinematic mount controlled by two nobs that allow for a free range of motion. By turning these nobs and placing the white card partially in the path of the laser beam, it may be confirmed that beam striking the first mirror is as well aligned as possible by eye.

Step 3. At this point an additional beam spot can be observed (using the white card) emitted from one of the sides of the beam splitter not facing the laser diode or

Mirror 1. The beam splitter cube must be rotated until both beam spots are on a similar size scale. Confirmation of this similarity is key for alignment of Mirror 2. Mirror 2 is aligned in the same fashion to Mirror 1. The height of the post in the mount is adjusted so that beam spot being emitted from the unblocked side strikes the center of the Mirror 2. Just as the Mirror 1, Mirror 2 is held by a kinematic mount controlled by two nobs that allow for a free range of motion. The white card is held between Mirror 2 and the beam splitter (blocking half of the beam) to ensure the reflection from the mirror strikes the exact point from which the beam spot is emitted on the beam splitter.

Step 4. The two mirrors are now generally aligned. The camera assembly is now positioned facing the last remaining open side of the beam splitter. Blocking half of the output beam near the camera aperture with the white card, two beam spots, such as the top two spots depicted in Fig. 3.7, are confirmed to lie in the same general area of the camera aperture. These two beam spots are the result of the initial beam being split and projected on the same plane. Here fine adjustments of both kinematic mounts are necessary to align both spots so that they lie an even distance on either side of the camera aperture.

Step 5. The fine adjustment requires adjusting both beam spots so that they overlap perfectly over the center of the camera aperture. Fig. 3.7 shows some of the fringe patterns that may be observed as fine alignment is achieved. If the mirrors are perfectly flat, as the spots move towards each other an off centered concentric ring pattern is observed as seen in Fig. 3.7 image (c). As the spots are more closely overlapped the ring pattern appears to shift towards the center of the camera aperture. In the event that one of the mirrors is tilted off its optical axis, a ring center pattern cannot be. As the two spots overlap a stripped fringe pattern is observed, illustrated in Fig. 3.7 image (a) and Fig. 3.8 image (a). This pattern appears to be centered at infinity.

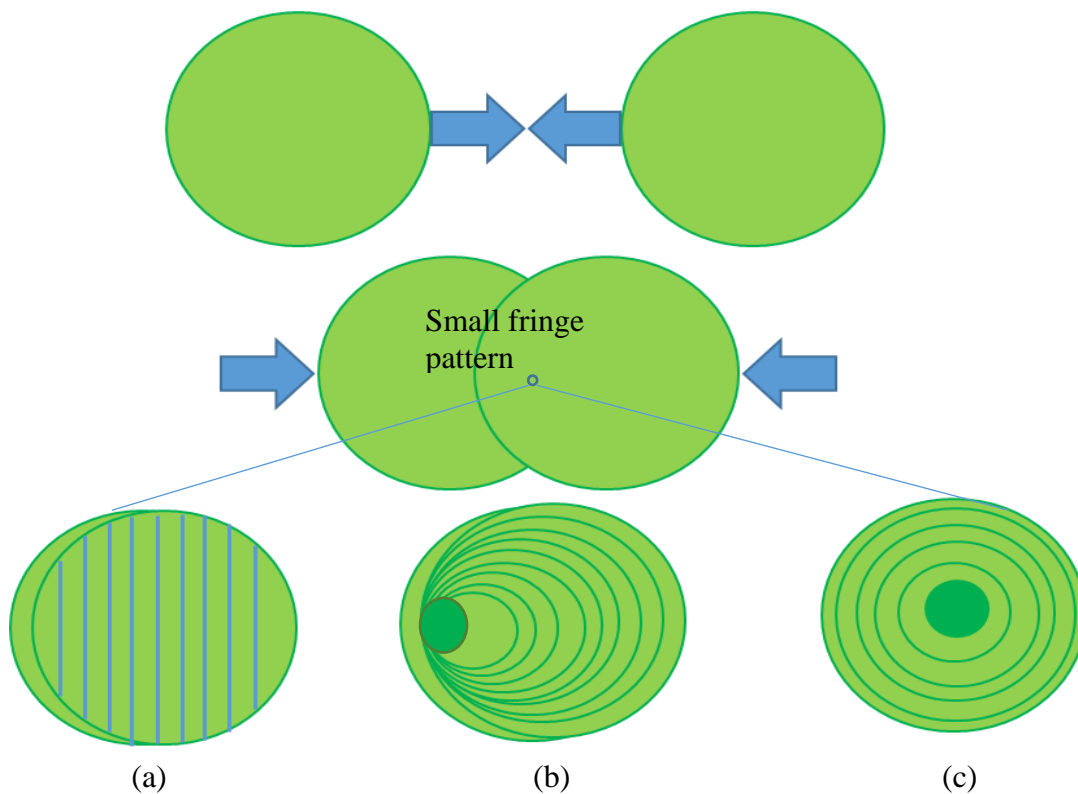
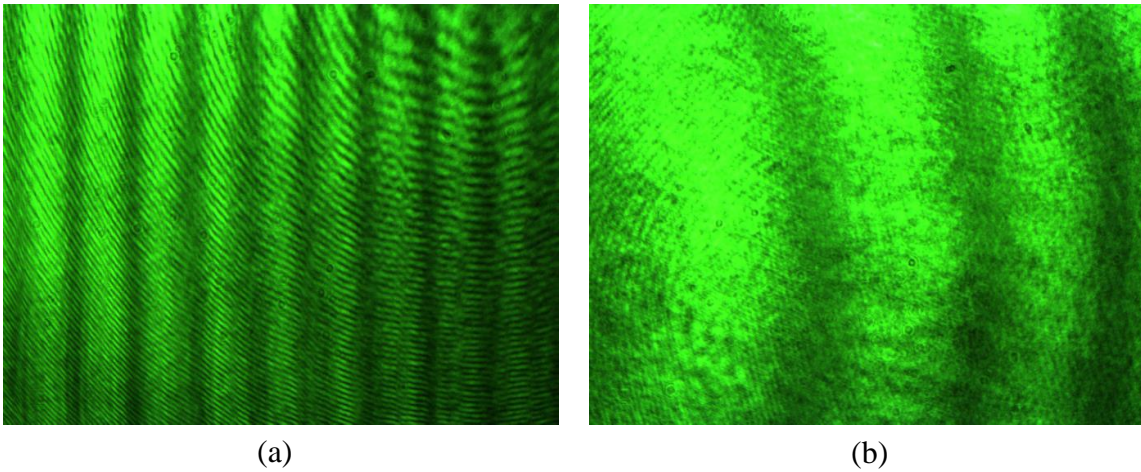


Figure 3.7: The fringe patterns observed as the two spots produced by the interferometer are aligned. (a) A strip fringe pattern will be observed if one the mirrors is slightly tilted. (b) An off-centered concentric pattern is observed as the two spots overlap. (c) A pattern of concentric rings is observed as two spots produced by two aligned mirrors are perfectly co-located.

Step 6. A near perfect concentric ring pattern similar to the image in Fig 3.7 (c) is the result of near perfect alignment and confirms that the mirrors are as perpendicular to the optical axis as possible. The experimental apparatus is now aligned. One of the mirrors may now be displaced along its optical axis to vary the optical path length of one of the beams. Note that increases/decreases of the optical path length on the micrometer scale result in very little variation in the fringe pattern produced. Small changes in optical path length difference cause the rings of the pattern to appear to move inward if the optical difference is reduced and appear to move outward if the optical path length difference is increased. This is according to the theory of Chapter 2. As the magnitude of the optical path length difference is increased from zero to one inch, the spacing between rings decreases dramatically.



3.8: (a) Fringe pattern produced by a mirror with severe tilt from its optical axis. (b) Fringe pattern produced by a mirror that is only slightly tilted from its optical axis.

The images in Fig. 3.8 are offered in support of the discussion of the images in Fig. 3.7. They show actual fringe patterns produced from a mirror that is titled severely and slightly in Fig. 3.8(b). It is important to note that using this apparatus at zero path length should produce a uniformly illuminated screen. A single ring is observed in Fig.

3.9(a) even when the position of both mirrors is determined using a Vernier caliper to measure a zero-path length difference. This implies that a Vernier caliper, whose least count is 1 mm, has insufficient resolution. A bright screen is expected theoretically through the knowledge that path traveled by the beam to both mirrors is the same. If the distance traveled is the same, both beams should arrive at the screen in phase, meaning that interference is uniform everywhere on the screen. Figure 3.9(b) shows an almost uniformly illuminated screen obtained after Mirror 1 is slightly nudged an unknown distance, thereby achieving an essentially zero beam path length difference. A secondary fringe pattern may be discerned in the background, however. This is an artifact of secondary reflections from the neutral-density filter.

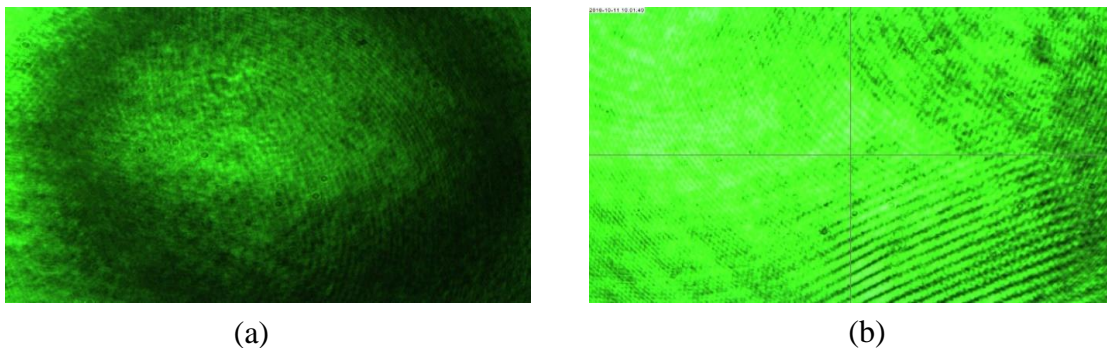


Figure 3.9: (a) Fringe pattern corresponding to the measured zero path length difference. (b) Fringe pattern obtained when Mirror 1 nudged slightly from its measured position.

Figure 3.10 illustrate the relationship between beam path length difference and the corresponding fringe pattern density. As the optical path length difference is reduced to 0.5 in., the center spot appears to increase in size and as the number rings decreases. As the optical path length difference is reduced further to as close to zero as possible, the center spot is observed to grow to almost completely fill the camera viewing area. At

what appears to be zero path length difference there will be only one ring, but if nudge a few nanometers almost completely bright area is observed.

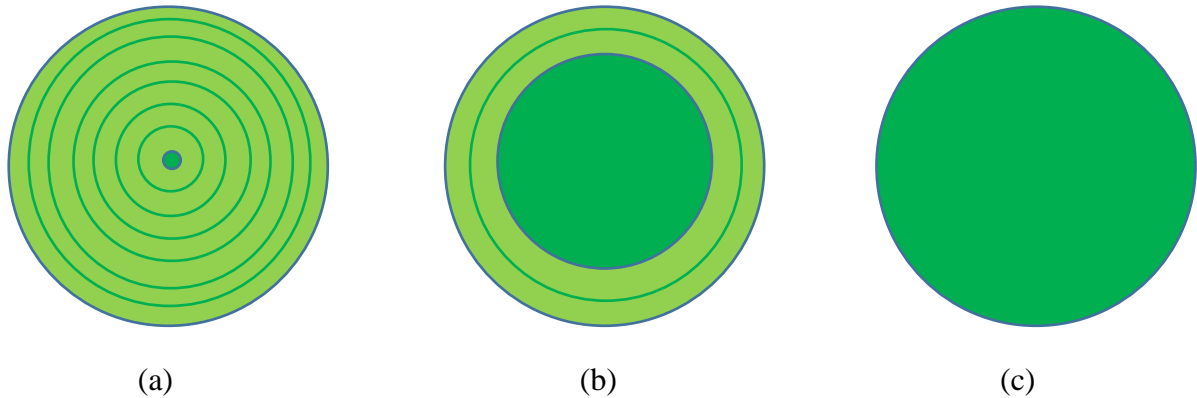
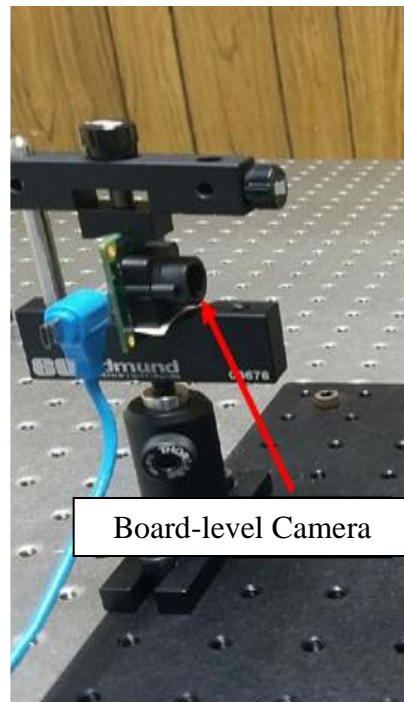
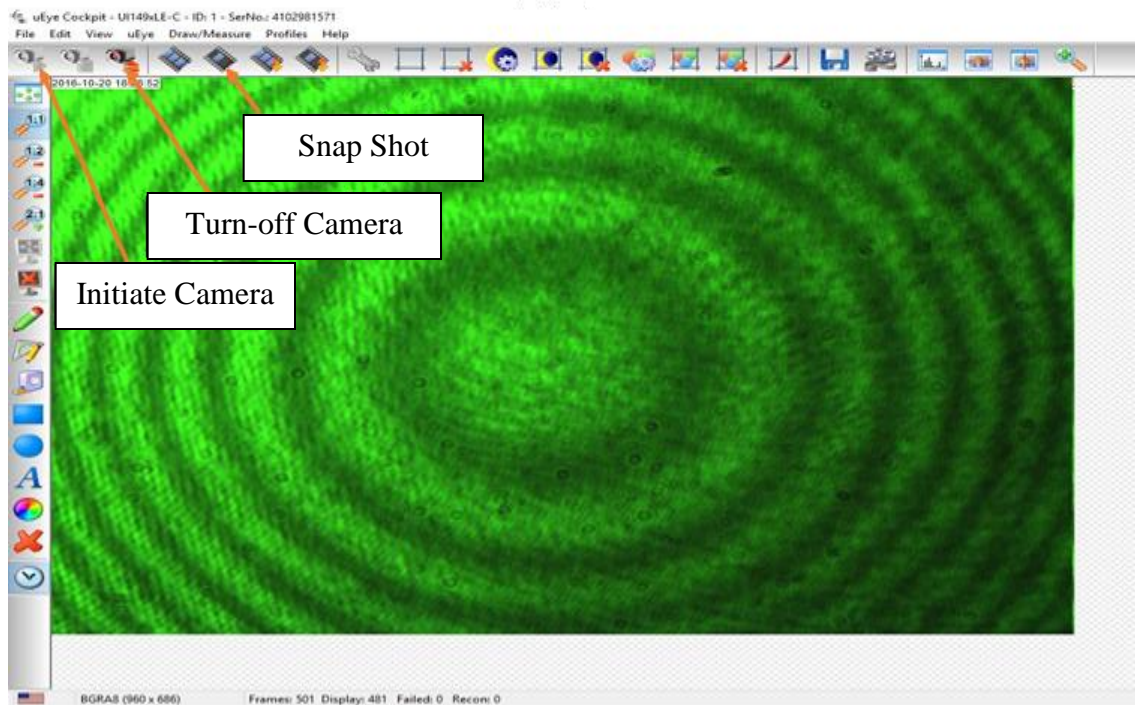


Figure 3.10: Relationship between beam path length difference and fringe spacing. Fringe pattern corresponding to (a) a relatively large beam path length difference, (b) a relatively small beam path length difference, (c) a beam path length difference of zero.

Step 7. Once fringe patterns are observed at the screen corresponding to a given beam path length difference, the screen is replaced with the board-level camera, which is connected to a computer running the program *uEye Cockpit*. Once connected and the program loaded, a play button initiates the camera video mode. If the apparatus has been aligned properly, the fringe pattern is displayed in *uEye Cockpit* as seen in Fig. 3.1. A slight displacement of one of the mirrors might be required to center the image. When centering, it is sometimes helpful to use the crosshair feature located under the *Draw/Measure* tab.



(a)



(b)

Figure 3.11: (a) The board-level camera and its connector cable. (b) The *uEye Cockpit* user interface with key buttons labeled.

Step 8. After a satisfactory fringe pattern is obtained an image may be recorded by selecting the “snap shot” icon displayed in Fig. 3.11(b). The image is now ready to be processed, so a program with image-processing software is required. For this thesis, *Mathematica* is used to process the image.

Step 9. Once the image file has been uploaded into *Mathematica* using the script:

```
Import[C:\\Users\\msmaur8\\Desktop\\Filename.bmp]
```

the image will appear indicating that it is ready to be processed. Processing the image involves extracting intensity values from every single pixel in the image of the fringe pattern. These intensity values are used to construct histograms and subsequently to verify the radii of the fringes, as described in Chapter 4.

Each pixel of the board-level camera actually consists of three separate pixels, one behind the other. One pixel is sensitive to red light (R), one to green light (G), and the third to blue light (B). Each pixel then carries information about the intensity in all three wavelength intervals. The image stores discrete intensities ranging from 0 to 255 for each of the three colors. The laser used in the research described in this thesis has a narrow spectral band centered around 532 nm. This results in high-intensity values for the green channel, and very low intensities for the red and blue channels, as expected. The [R, G, B] data are therefore in a convenient format for creating images, but are difficult to use for extracting numerical results. Therefore, the [R, G, B] data are converted to a gray scale which combines the [R, G, B] data for each pixel into a single number.

Therefore, the existing greyscale image processing capability is used. Greyscale image processing allows irrelevant color information to be suppressed, effectively reducing the volume of data and the noise caused by including information from the R

and B channels. Greyscale uses principles of colorimetry to match the luminance of the grayscale image to the luminance of the original color image, and thus converts the pixel containing the three intensities [R, G, B] into a single intensity value for each pixel with an intensity value between 0 and 1 [Poynton 1998]. The script used to convert the color image into a greyscale image is

```
grayImage=ColorConvert[, "Grayscale"] .
```

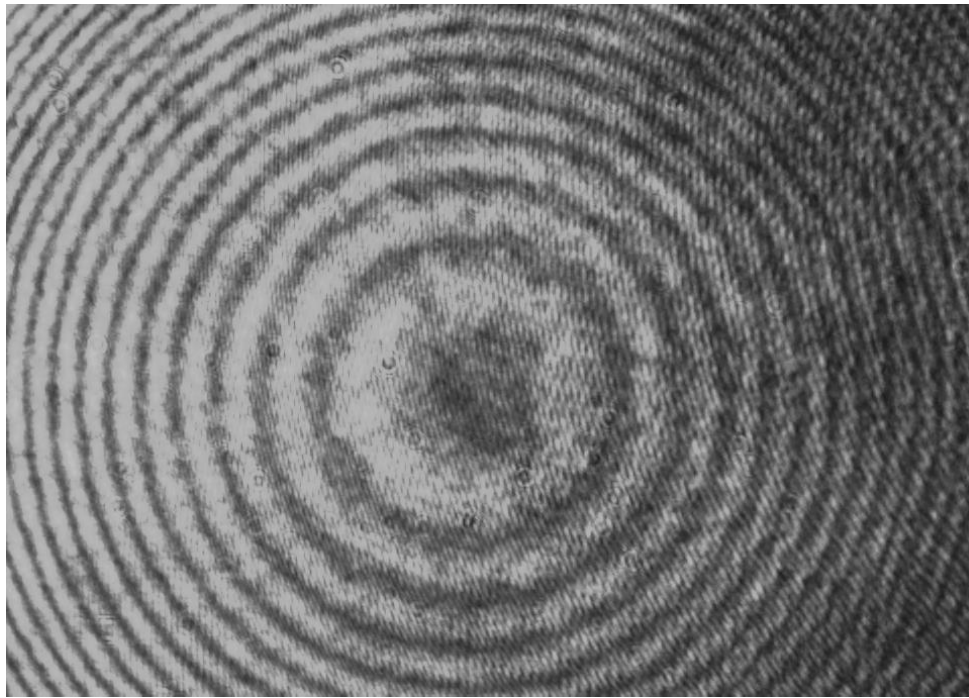


Figure 3.12: Color image after it has been converted to greyscale.

Step 10. The intensity values can be extracted after the color image has been converted to greyscale, as illustrated in Fig. 3.12. The script used to extract the intensity values is

```
t=intensVals=Flatten@ImageData[grayImage]
```

Step 11. *Mathematica* is used to insert the intensity values into a 960 x 686 matrix.

The data are then exported to *Microsoft Excel* as a comma-separated value (CSV) using the script

Export ["User specified filename .csv", h]

Once in *Microsoft Excel* histograms maybe created by plotting any row or column of intensities.

Chapter 4: Results of Experimental Effort and Discussion

Experimental data collected during the course of the research carried out in this thesis are presented and their implication is discussed.

4.1 Experimental Results for Zero Beam Path Length Difference

Figure 4.1 represents an illumination pattern produced by the Michelson interferometer when the path length difference for the two beams is adjusted as near as possible to zero. The focal plane array is observed to be almost uniformly illuminated with no discernable pattern. This is the expected result that agrees well with the theory presented in Chapter 2. It is relevant to note that these data justify earlier observations made in Chapter 3, Section 3.2, concerning the nonuniformity of the laser source brightness. The nonuniformity of illumination in Figure 4.1 is characterized by the reduction in intensity on the right side of the image compared to the left side. This feature is also captured by the histogram in Fig. 4.2 which, without this source distortion, would be expected to indicate an essentially uniform intensity. However, the histogram reveals that, on average, the intensity values corresponding to the left side of the image are higher than the values corresponding to right side of the image. Also, a significant amount of noise is present in the histogram.

Fig 4.3 is a histogram created from the intensity values obtained from a vertical scan of the pixels passing through the center of the screen along the path of the vertical red line in Fig 4.1. This histogram provides further evidence of an illumination nonuniformity. The histogram in Fig. 4.3 shows that intensity values are higher at the top of image than at the bottom of the image. This is once again a departure from expectations for an ideal interferometer, which should produce a uniform illumination.

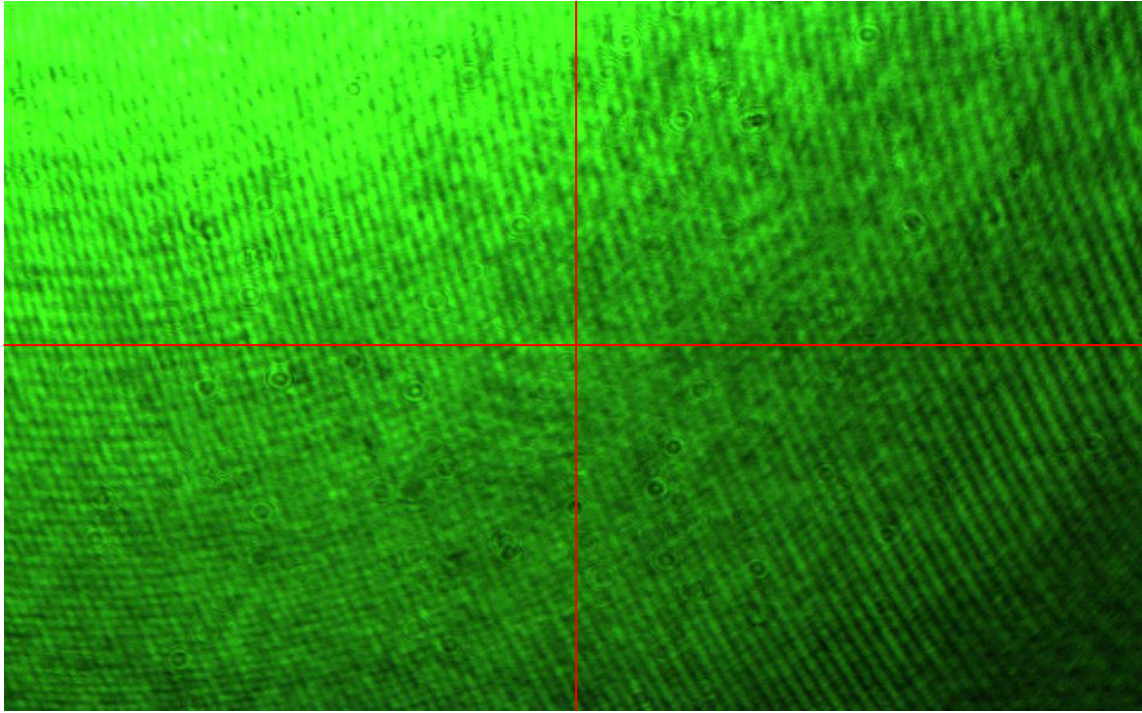


Figure 4.1: Illumination pattern produced by a Michelson Interferometer with a near-zero difference between the path lengths of the two beams.

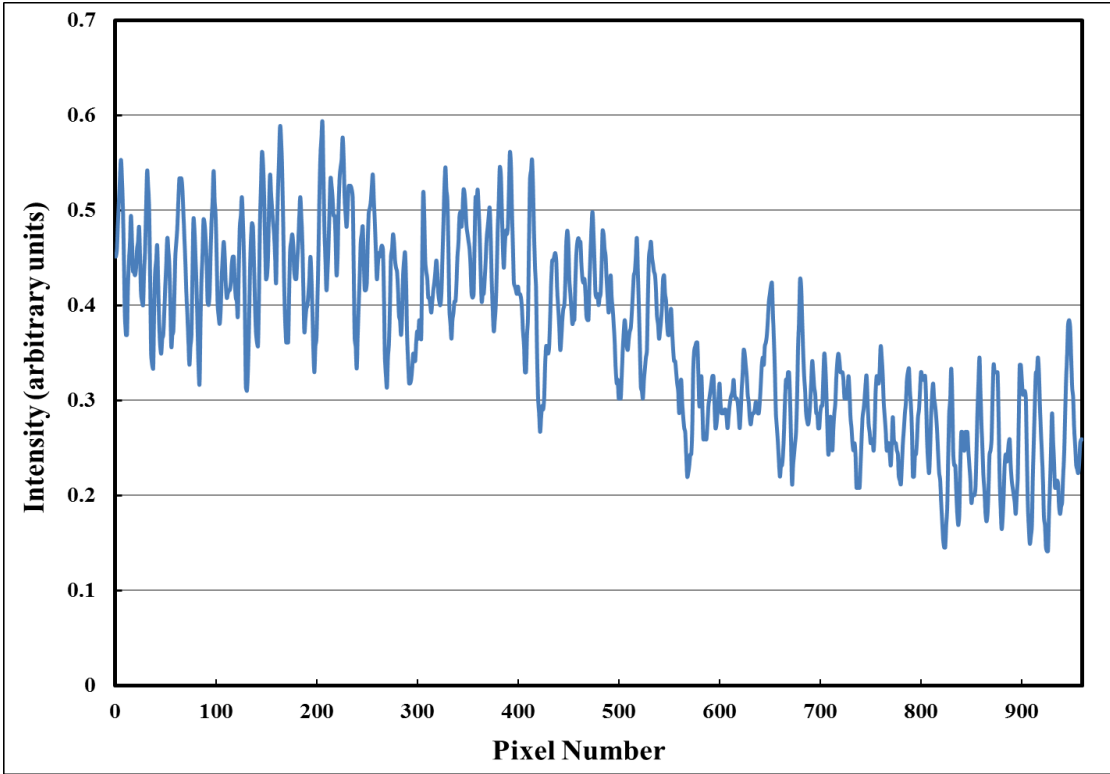


Figure 4.2: Histogram corresponding to the image in Fig 4.1 obtained by scanning along the horizontal red line in Fig 4.1.

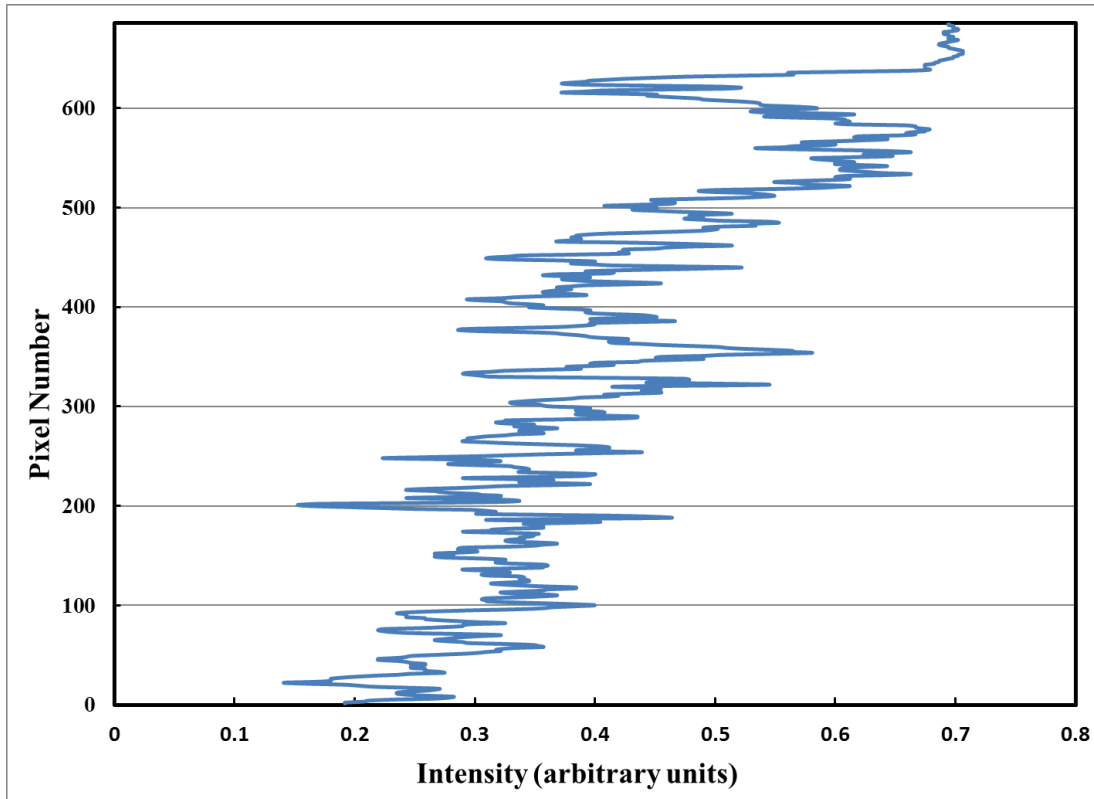


Figure 4.3: Histogram corresponding to the image in Fig 4.1 obtained by scanning along the vertical red line in Fig 4.1.

4.2 Experimental Results for a Beam Path Length Difference of One Inch

Figure 4.4 (a) shows the fringe pattern produced by the Michelson interferometer when the beam path length difference is set as near as possible to one inch (25.4 mm). This figure exhibits a distinct pattern composed of alternating concentric dark and bright rings. This is the expected result which coincides with the theory presented in Chapter 2. The manifestation of a concentric ring pattern demonstrates that alignment efforts were successful. If one of the mirrors is slightly tilted, the concentric pattern would be replaced by a pattern of longitudinal fringes or, if the tilt is sufficiently severe, by no pattern at all. The vertical yellow lines connecting Fig 4.4 (a) and 4.4 (b) indicate the relationship

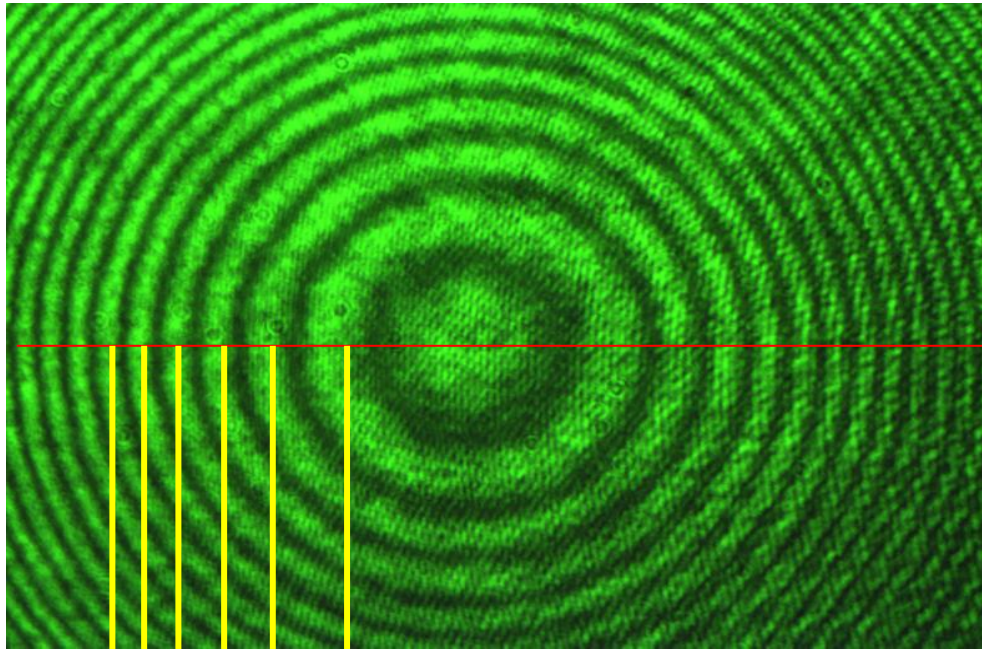
between the bright ring diameters in Fig 4.4 (a) and the peaks in the histogram of Fig 4.4 (b).

Even though a circular fringe pattern is clearly visible, the specific boundary between successive dark and light rings is difficult to distinguish. This ambiguity arises because of noise in the signal which introduces uncertainty in the interpretation of fringe radii elsewhere in this chapter. Nonuniformity of illumination is demonstrated in Fig. 4.4 (a) by the reduction in contrast from the left side of the image to the right side and, to a lesser extent, from the top to the bottom. This reduction in contrast is especially evident in the histogram of Fig. 4.4 (b). The histogram consists of a wave train with peaks corresponding to bright rings, or constructive interference, and dark rings, or destructive interference.

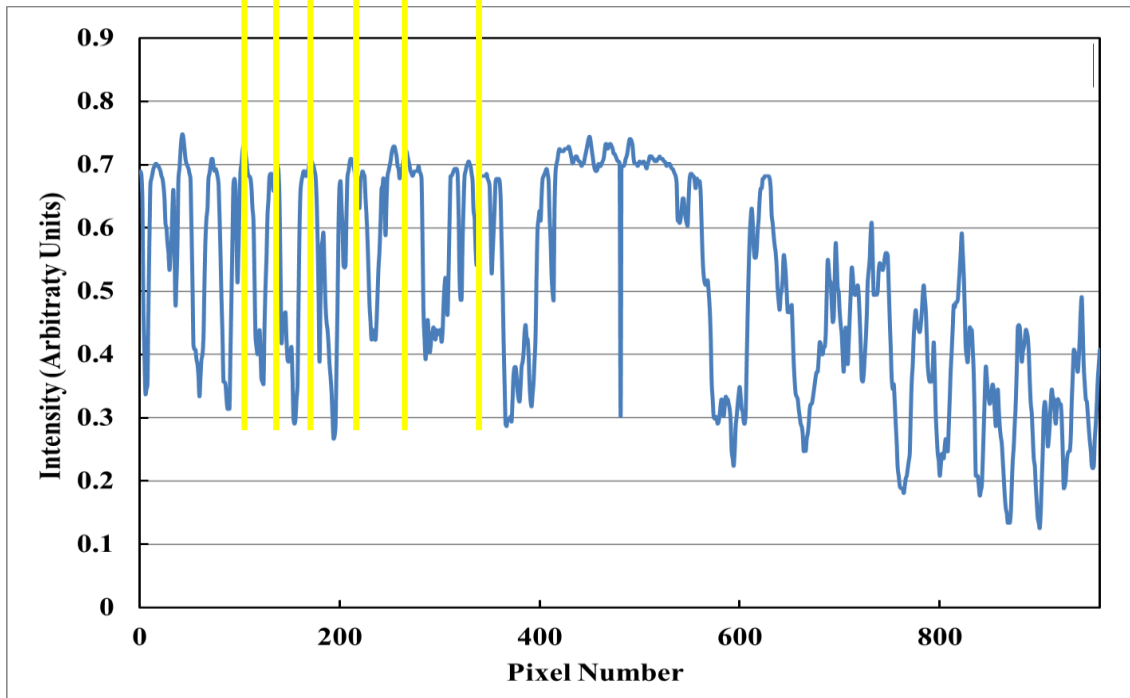
4.3 Experimental Results for a Beam Path Length Difference of Two-Inches

Figure 4.5 (a) illustrates a fringe pattern produced by the Michelson interferometer when the beam path length difference is set as nearly as possible to two inch (50.8 mm). The figure exhibits a distinct concentric ring pattern, composed of dark and bright rings. This is an expected result based on the theory discussed in Chapter 2. The vertical yellow lines connect the diameters of bright rings in Fig 4.5 (a) with the peaks in the histogram in Figure 4.4 (b). The background of the fringe pattern has a near uniform brightness across the screen. The histogram confirms this because the gradient in intensity from one side of the image to the other is less severe than in the one-inch beam path length case.

The fringe pattern displayed in Fig 4.5(a) is less distinct than the pattern displayed in Fig. 4.4(a), because it contains a higher level of background noise. The noise in the signal seems to be exacerbated by increasing beam path length difference. This occurs because an increase in beam path length difference reduces the average number of rays per bin. The high level of noise reduces the visibility of the fringes.



(a)



(b)

Figure 4.5: (a) Fringe pattern produced by a Michelson interferometer at a measured beam path length difference of two inch (b) Corresponding histogram obtained by scanning along the horizontal line Fig 4.5 (a).

Chapter 5: Numerical Model of the Michelson Interferometer

The current chapter describes a numerical model of the Michelson Interferometer which has been composed in the Matlab environment based on the Monte-Carlo ray-trace method. The principles of geometric optics have been applied to a large number of individual rays emitted in a collimated beam by laser and followed through their interactions with a lens, a beam splitter, plane mirror, and focal plane array (FPA). Shown schematically in Fig. 5.1 is the basic Michelson Interferometer whose performance is modeled in the current chapter.

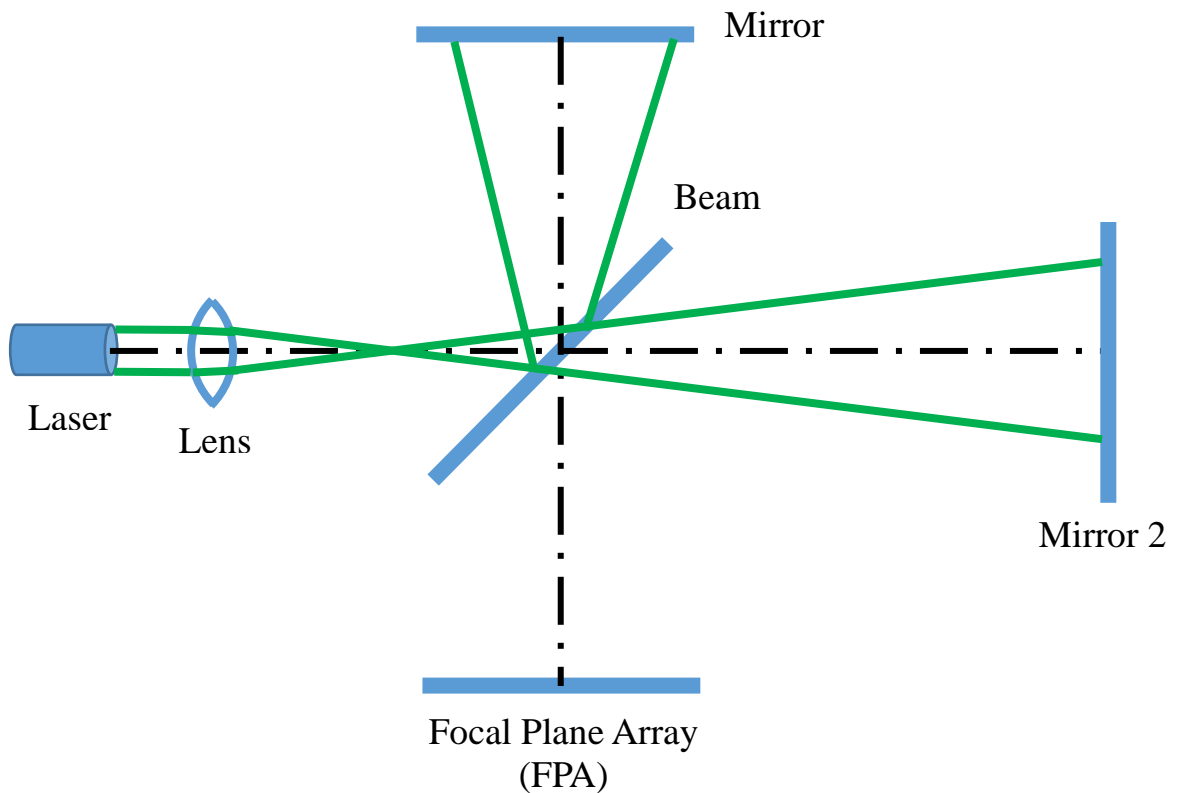


Figure 5.1: Schematic diagram of the basic Michelson interferometer whose performance is modeled in this chapter.

5.1 Underlying Principles

The method begins by establishing the geometry. In the case at hand the source of the rays is a laser which emits collimated radiation from a circular aperture. The rules for determining the source points of the individual rays are based on statistics, as described by Mahan [2002, pp. 346-347]. Under the assumption of a uniform source the equations for the radial position r and angular position ϕ are

$$r = \frac{D}{2} \sqrt{R_r} \quad (5.1)$$

and

$$\phi = 2\pi R_\phi. \quad (5.2)$$

Because the laser is considered to be a collimated source the direction cosines of each ray are $(L_0, M_0, N_0) = (0, 0, 1)$. Furthermore, all the emitted rays are considered to be in phase since lasers are known to be coherent sources.

The first optical element the ray encounters is the front surface of the condensing lens, whose equation is

$$S(x, y, z) = x^2 + y^2 + (z - z_c)^2 - R^2 = 0, \quad (5.3)$$

where z_c is the location on the interferometer optical axis of the center of the sphere and R is its radius. The point of intersection of the ray on the front surface of the lens is determined by solving the equations of the line containing the ray,

$$(x - x_0)/L = (y - y_0)/M = (z - z_0)/N = t, \quad (5.4)$$

simultaneously with Eq. (5.3). In Eq. (5.4) t is the distance from the source point (x_0, y_0, z_0) to the point of intersection (x_1, y_1, z_1) , or

$$t = [(x - x_0)^2 + (y - y_0)^2 + (z - z_0)^2]^{1/2}. \quad (5.5)$$

The next step is to apply Snell's Law,

$$\sin(\theta_2)/\sin(\theta_1) = n_1/n_2 , \quad (5.6)$$

where θ_1 is the angle of incidence of the ray with respect to the local surface normal, θ_2 is the angle of the refracted ray makes with the negative of the local surface normal, n_1 is the refractive index of the medium in which the incident ray propagates, and n_2 is the refractive index of the lens material. The vector form of Snell's Law is

[www.starkeffects.com/snells-law-vector.shtml]

$$\mathbf{v}_1 = \left(\frac{n_1}{n_2}\right) [\mathbf{n} \times (-\mathbf{n} \times \mathbf{v}_0)] - \mathbf{n} \sqrt{1 - \left(\frac{n_1}{n_2}\right)^2 (\mathbf{n} \times \mathbf{v}_0) \cdot (\mathbf{n} \times \mathbf{v}_0)}, \quad (5.7)$$

where $\mathbf{v}_1 = L_1 \mathbf{i} + M_1 \mathbf{j} + N_1 \mathbf{k}$ is the unit vector in the direction of the refracted ray, \mathbf{n} is the local unit vector at the surface of the lens, and $\mathbf{v}_0 = L_0 \mathbf{i} + M_0 \mathbf{j} + N_0 \mathbf{k}$. The local unit normal vector is

$$\mathbf{n} = \nabla S / |\nabla S| = x/R \mathbf{i} + y/R \mathbf{j} + (z - z_c)/R \mathbf{k} . \quad (5.8)$$

The process described above is repeated for the back surface of the condensing lens. The result for each ray is the set of direction cosines (L, M, N) converging to the focal point of the lens. The rays diverge from the focal point to the Beam Splitter where every second ray is deflected toward Mirror 1 (Beam A), with the remaining rays continuing on to Mirror 2 (Beam B). The rays constituting Beam A, upon arrival at the surface of the Beam Splitter, undergo a 90-deg deflection toward Mirror 1 with a 180-deg phase shift. The rays constituting Beam B pass through the Beam Splitter without change of direction or phase. The direction of each ray, upon arrival at the Mirrors 1 and 2, is reversed and shifted in phase by 180 deg. Beam B, upon arrival at the Beam Splitter a second time is deflected toward the Focal Plane Array (FPA), as described in Chapter 2.

The net result is that each ray arriving at the FPA will undergo a net phase shift equal to $360 \text{ deg} + 2\pi d/\lambda$, where d is the path length from its source point to the point on the FPA and λ is the wavelength of the laser. Then two rays, one from Beam A and one from Beam B, arriving at the same point on the FPA undergo a net phase difference of $2\pi (d_A - d_B)/\lambda$.

It is highly unlikely that two beams will intercept the FPA at precisely the same point (y, z) . It is therefore necessary to identify the rays that are incident on the same pixel of the FPA. If two rays from the same beam are incident to the same pixel they will of necessity have essentially the same phase relative to their phase at the source. During execution of the program the y, z -coordinates of the point of incidence on the FPA of a given ray are converted to the indices (m, n) ; that is, the point (y, z) lies within a pixel, or bin, in row m and the column n . The phase of all rays incident to bin (m, n) is then the average of the phases of the individual rays incident to that bin. The final step is illustrated in Fig. 5.1. The figure shows the radial variation of phase, measured from the center of the FPA, for rays from Beam A and rays from Beam B. The phase changes more rapidly with radial position r for Beam A if Mirror 1 is further from the Beam Splitter than Mirror 2. This means that the average phase angle of rays from Beam A in bin (m, n) is larger than the average phase angle of rays from Beam B in the same bin. The intensity of the combined radiation from Beams A and B incident to bin (m, n) is then given by

$$I(m, n) \propto E_A^* E_B = E_{A0}^2 + E_{B0}^2 + 2E_{A0}E_{B0} \cos[\phi_A(m, n) - \phi_B(m, n)] . \quad (5.9)$$

For the special case where $E_{A0} = E_{B0} = E_0$,

$$i(m, n) = \frac{E_A^* E_B}{2E_0^2} = 1 + \cos[\phi_A(m, n) - \phi_B(m, n)] , \quad (5.10)$$

where i is now a non-dimensional relative intensity.

5.2 Numerical Implementation

The Matlab code which implements the forgoing principles is reproduced in Appendices B through D. The first step is to compute the (x, y, z) coordinates of the points of intersection of each ray with the various optical elements making up the Michelson interferometer. As explained in the previous section this involves solving the equations for the various surfaces simultaneously with the equations of the line containing the ray. These points may then be connected to form the path followed by each ray. Figure 5.2 illustrates the ray paths from the source through the front and back surfaces of the condensing lens, through its focal point, and to the Beam Splitter, where they are deflected 90 deg to Mirror 1. Figure 5.3 illustrates the ray paths from Mirror 1 through the Beam Splitter to the Focal Plane Array. Note that these two figures are not drawn to the same scale. The intersections of the rays with the lens, the mirror, and FPA form disks and the intersection with the Beam Splitter forms an ellipse (not shown in these views). Similarly, Fig. 5.4 illustrates the ray paths from the source through the front and back surfaces of the condensing lens, through its focal point, through the Beam Splitter, and onto Mirror 2; and Fig. 5.5 illustrates the ray paths from Mirror 2 to the Beam Splitter where it is deflected 90 deg, and on to the Focal Plane Array. These two figures are also not drawn to the same scale.

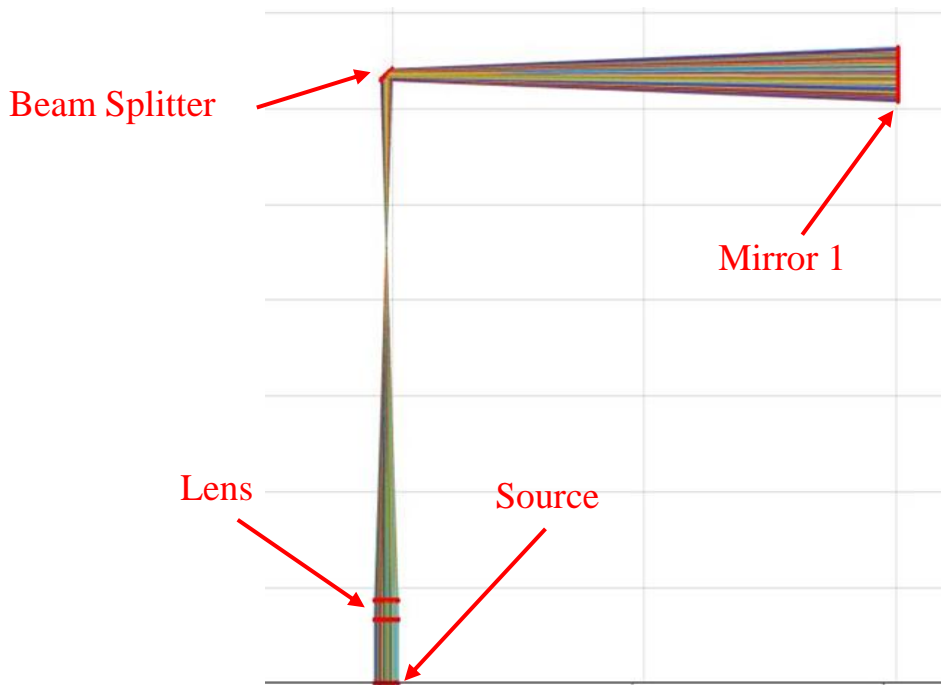


Figure 5.2: Rays making up Beam A path from the laser to Mirror 1.

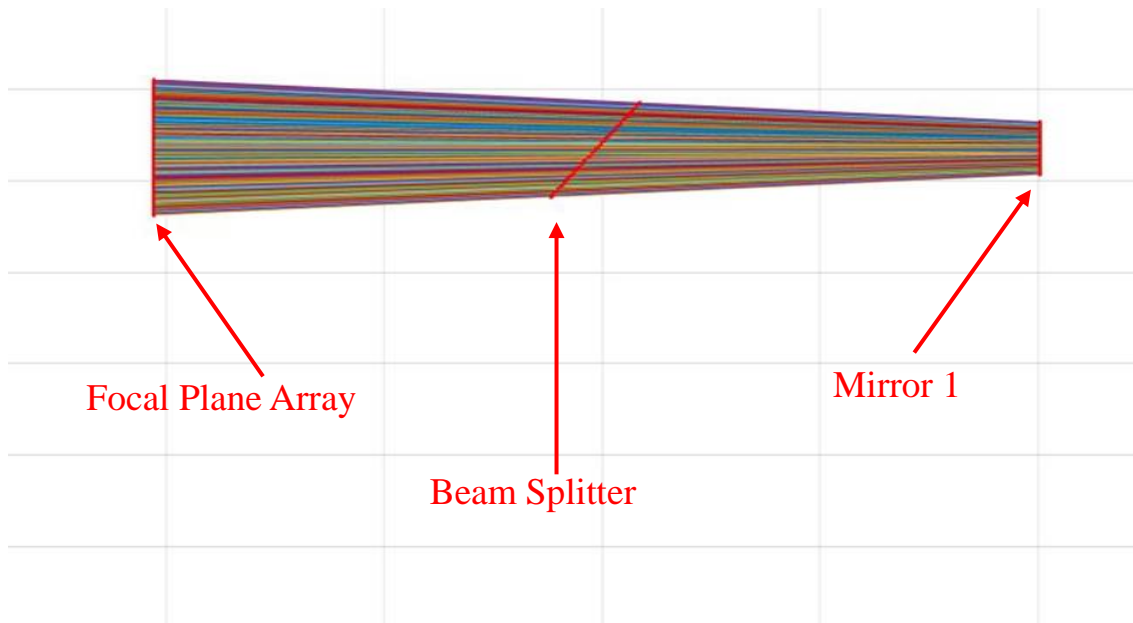


Figure 5.3: Rays making up Beam A path from Mirror 1 through the Beam Splitter to the FPA.

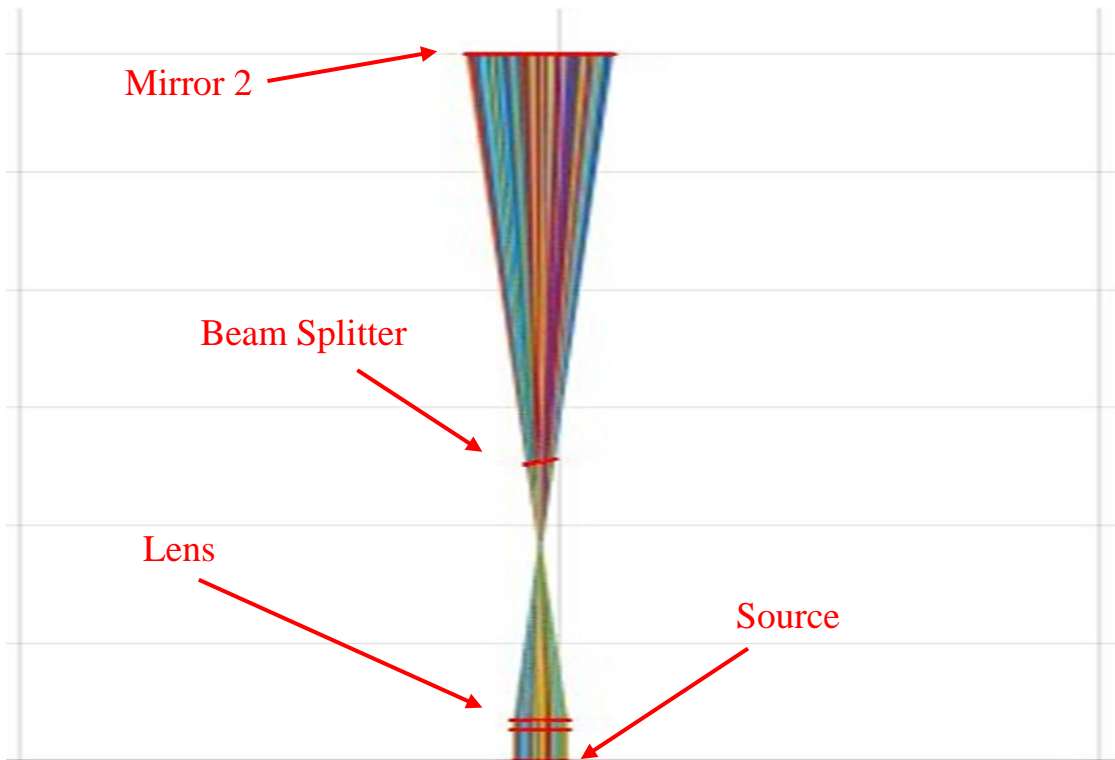


Figure 5.4: Rays making up Beam B path from the laser to Mirror 2.

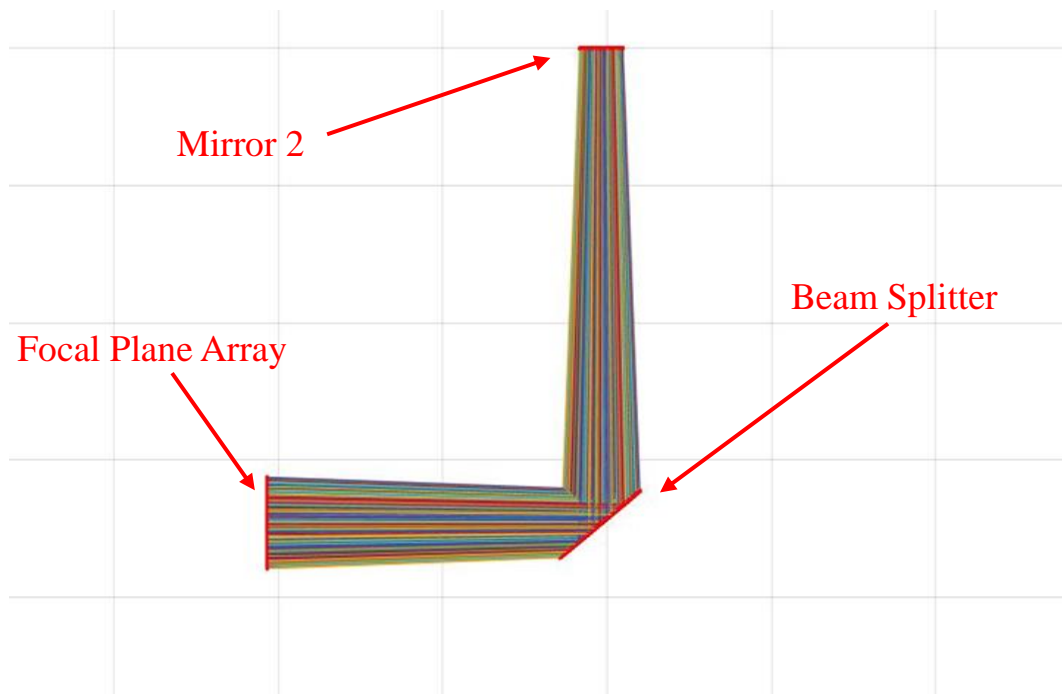


Figure 5.5: Rays making up Beam B path from Mirror 2 through the Beam Splitter to the FPA.

The next step is to find the length of each ray from its point of emission in the aperture of the laser to its point of incidence on the Focal Plane Array,

$$T = \sum_1^N (t_1)_n, \quad (5.11)$$

where N is the total number of ray segments and n refers to n^{th} segment. In doing this care must be taken to use the maximum number of significant figures available because the path length itself is measured in millimeters but the difference in path length of rays from the two beams is measure in micrometers. In Matlab the *format long* command provides 15 significant figures. Then for example if in bin (m, n) the ray length from Beam A is 12345678.1234567 and the ray length from Beam B is 12341234.5678910, the most significant figures common to both rays, 12340000.0000000, can be subtracted from both numbers, yielding 5678.1234567 for Beam A and 1234.5678910 for Beam B. In the following development, T_A and T_B are ray lengths that have been adjusted by subtracting off the most significant figures common t both beams.

Thus, in the example $T_A = 5678.1234567$ and $T_B = 1234.5678910$. That is, the integer number of cycles common to both rays, 12,340,000, is of no consequence. Following this convention ϕ_A and ϕ_B may be written

$$\phi_A = 2\pi T_A/\lambda \text{ and } \phi_B = 2\pi T_B/\lambda . \quad (5.12)$$

It is instructive to plot the variation of the resulting phase angles with position (m, n) on the Focal Plane Array. Figure 5.6 is an idealization of the expected radial variation of ϕ_A and ϕ_B .

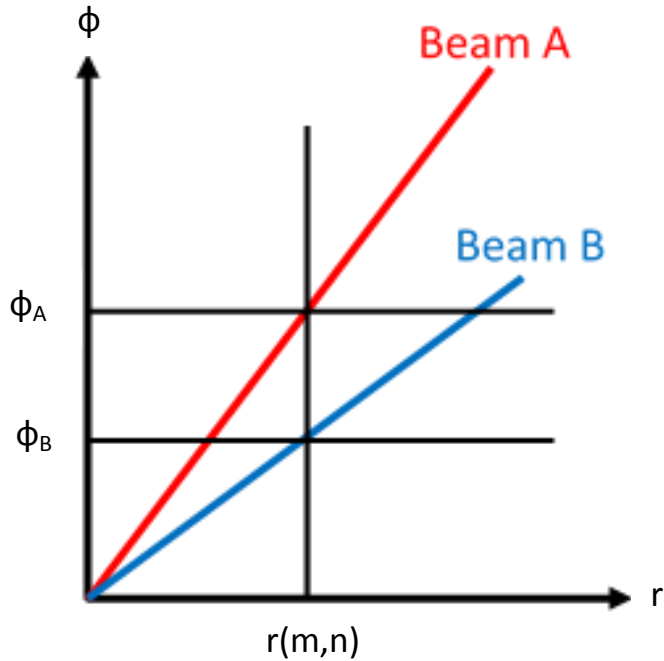


Figure 5.6: Idealization of the variation with radial position of phase difference between rays from Beam A and Beam B in bin (m, n) on the Focal Plane Array.

The active field of the board-level camera used in the research described in this thesis consists of a 960-by-686 array of pixels, each pixel measuring a few micrometers on a side. A vendor representative claimed that the pixels measure between three to five micrometers on a side, but the specifications provided with the product indicate pixel sizes of 1.67-by-1.67 μm . In any case the distance to the focal plane array from the camera entrance aperture is unknown; therefore, the exact size of the pixels is irrelevant.

Figures 5.7 and 5.8 show the distribution of the phase angle on the Focal Plane Array for Beams A and B, respectively.

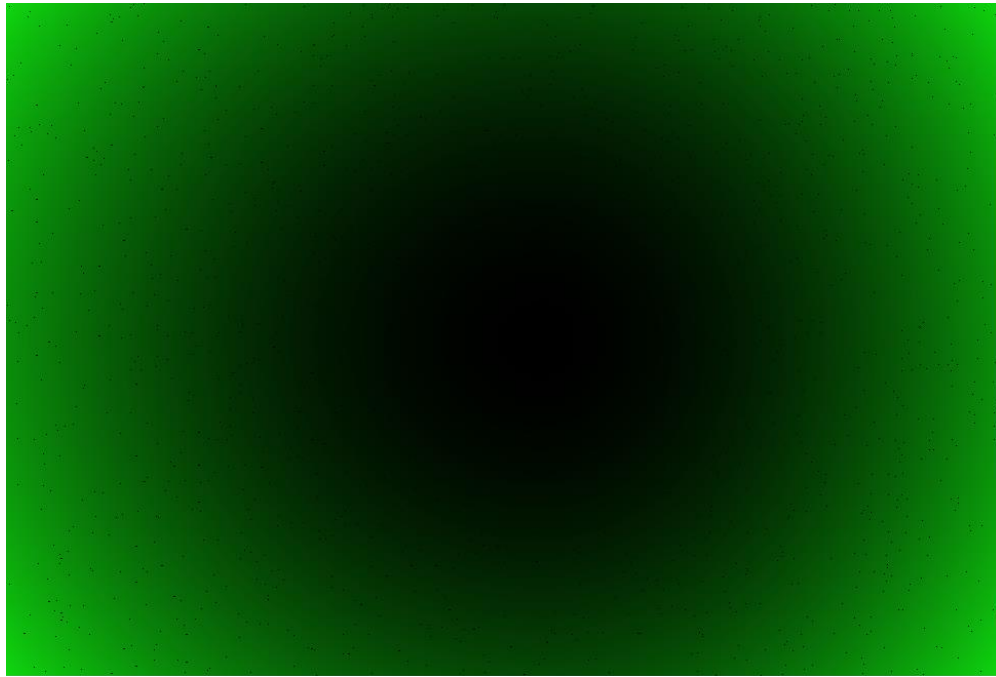


Figure 5.7: Distribution of phase angle on the Focal Plane Array when Mirror 1 is 2 in. from the Beam Splitter (Beam A).

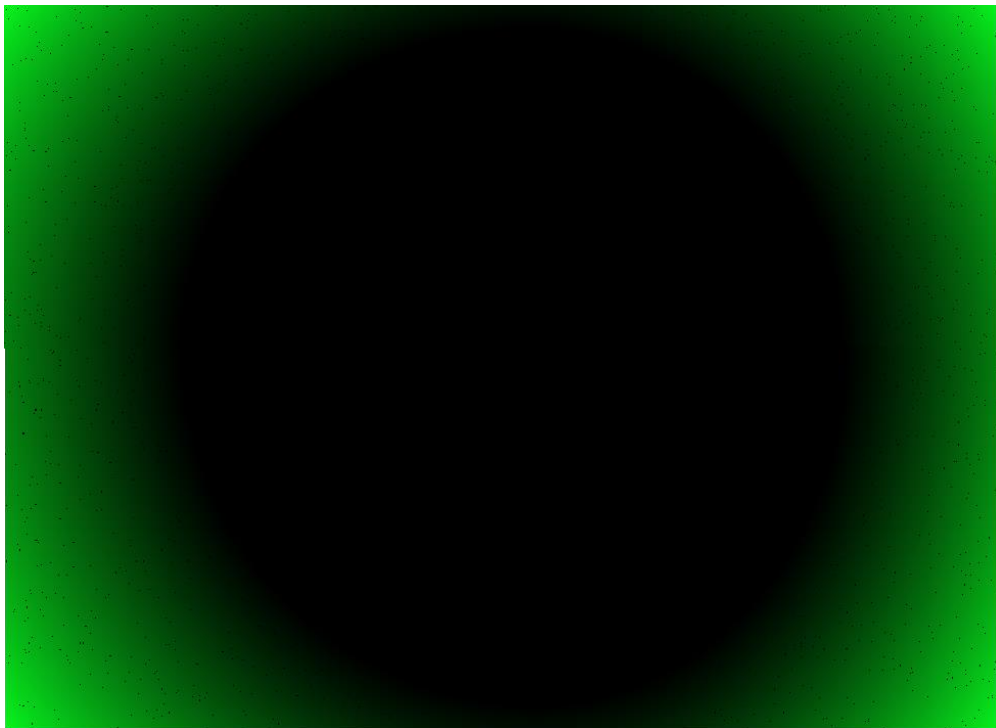


Figure 5.8: Distribution of phase angle on the Focal Plane Array when Mirror 2 is 3 in. from the Beam Splitter (Beam B).

The actual smooth radial variation of phase is not well captured in Figs. 5.7 and 5.8 because of limitations in the color conditioning rules available in Microsoft Excel. The individual pixels visible as “flakes” in the lighter regions of these figures and elsewhere in this thesis are due to bins which did not gather any rays and therefore reflect a phase of zero degrees.

Figure 5.9 is a comparison of the experimental screen intensity, already shown in Fig. 4.1, with the simulated screen intensity for the case of zero path length difference between Beam A and Beam B. Both images have 960 horizontal pixels and 686 vertical pixels. However, after compression of the images to fit the available margins, individual pixels cannot be discerned. Therefore, the simulated image in Fig. 5.9(b) is perfectly uniform while the experimental image in Fig. 5.9(a) shows the departure from uniformity already discussed in Chapter 4.

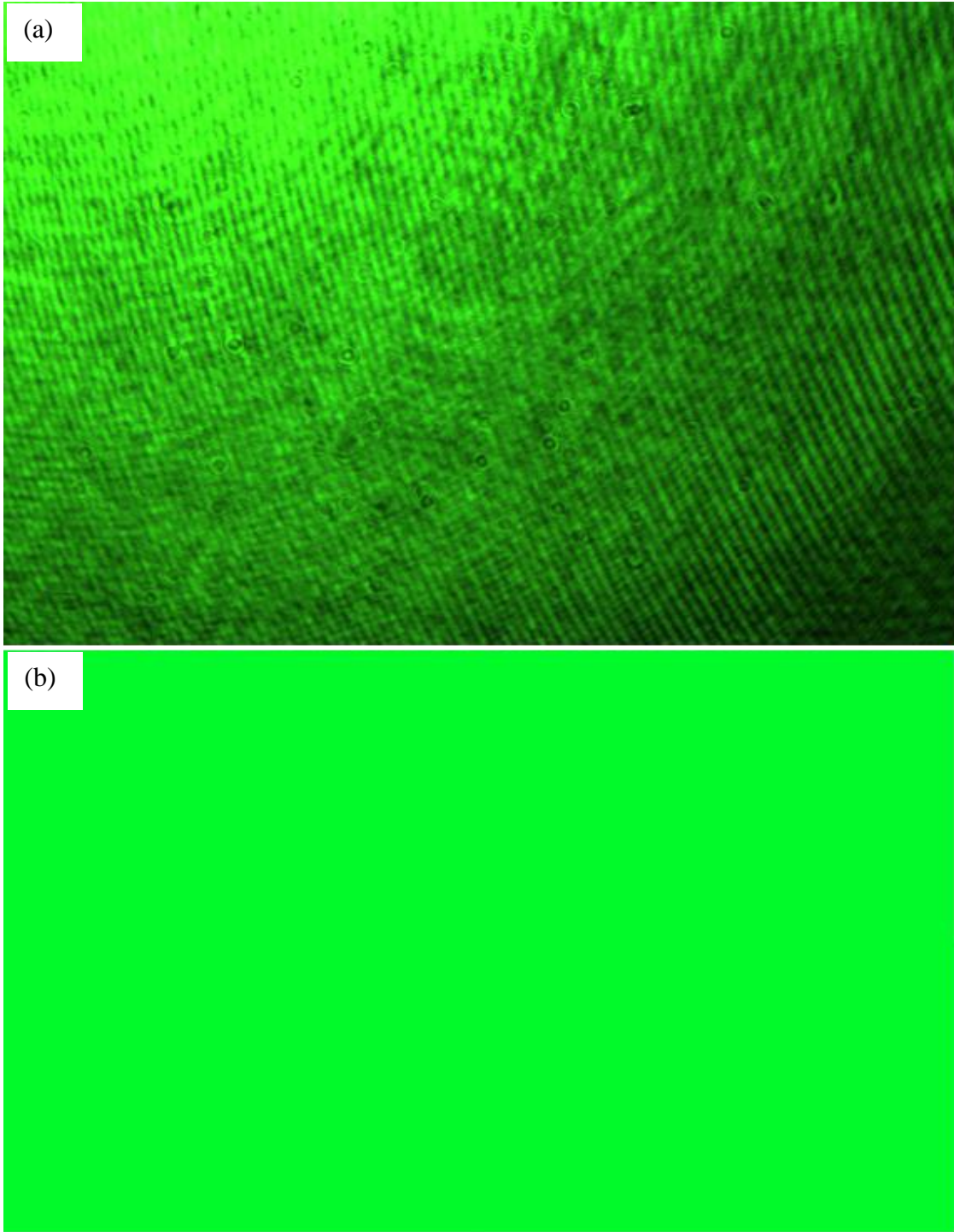


Figure 5.9: (a) Experimental image and (b) simulated image for the case of zero path length difference between Beam A and Beam B.

Figure 5.10 is a comparison of the experimental screen intensity, a version of which has already been shown in Fig. 4.4(a), with the simulated screen intensity for the case of a one-inch path length difference between Beam A and Beam B.

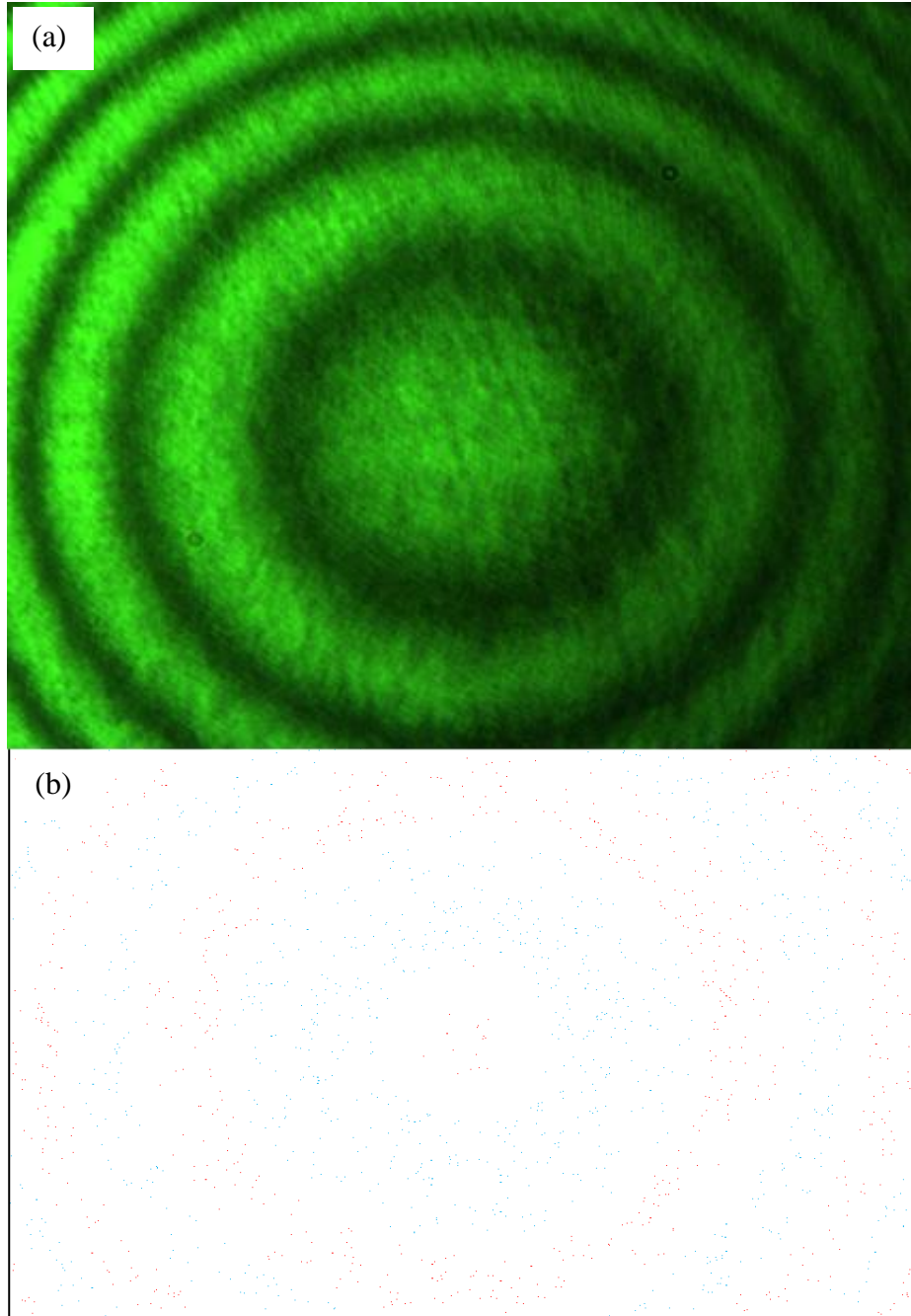


Figure 5.10: (a) Experimental image and (b) simulated image for the case of a one-inch path length difference between Beam A and Beam B.

An uncertainty exists in the distance from Beam Splitter to the Focal Plane Array within the board-level camera used to obtain the experimental data. Also, recall that the center of the experimental image is not located at the center of the Focal Plane Array, as discussed in Section 3.2, Figs. 3.5 and 3.6. For these reasons, direct comparison of the experimentally obtained image of Fig. 5.10(a) and the simulated image of Fig. 5.10(b) is not possible.

Appearances to the contrary, fringes are present in Fig. 5.10(b). This image is based on tracing 10,000,000 rays into 658,560. Therefore, on the average only about 15 rays are available per pixel. This means that the outermost pixels are significantly underpopulated and that in general the image is under-sampled. This, added to the exceedingly small size of the pixels, makes individual pixels difficult to discern. In this situation, it is impossible to image a smooth variation in intensity while conditioning with a two-color rule in Microsoft Excel. For that reason, the conditioning rule used to create Fig. 5.10(b) is:

If $0.0 \leq \text{intensity} \leq 0.1$, fill the cell with blue; and if $0.9 \leq \text{intensity} \leq 1.0$, fill the cell with red.

This results in a thin pattern of red flakes populating the “bright” rings (constructive interference), and a thin pattern of blue flakes populating the “dark” rings (destructive interference). With these caveats in mind careful study of Fig. 5.10(b) does in fact reveal a pattern of concentric fringes, and that the orders of the experimentally obtained fringes are at least similar to the orders of the simulated fringes. In order to improve the visibility of the fringes the upper left hand quadrant of Fig. 5.10(b) is

reproduced in Fig. 5.11. This has the effect of increasing the area of each pixel by a factor of 16, thereby rendering them more visible.

Figure 5.12 is a comparison of the experimental screen intensity, a version of which has already been shown in Fig. 4.5(a), with the simulated screen intensity for the case of a two-inch path length difference between Beam A and Beam B.

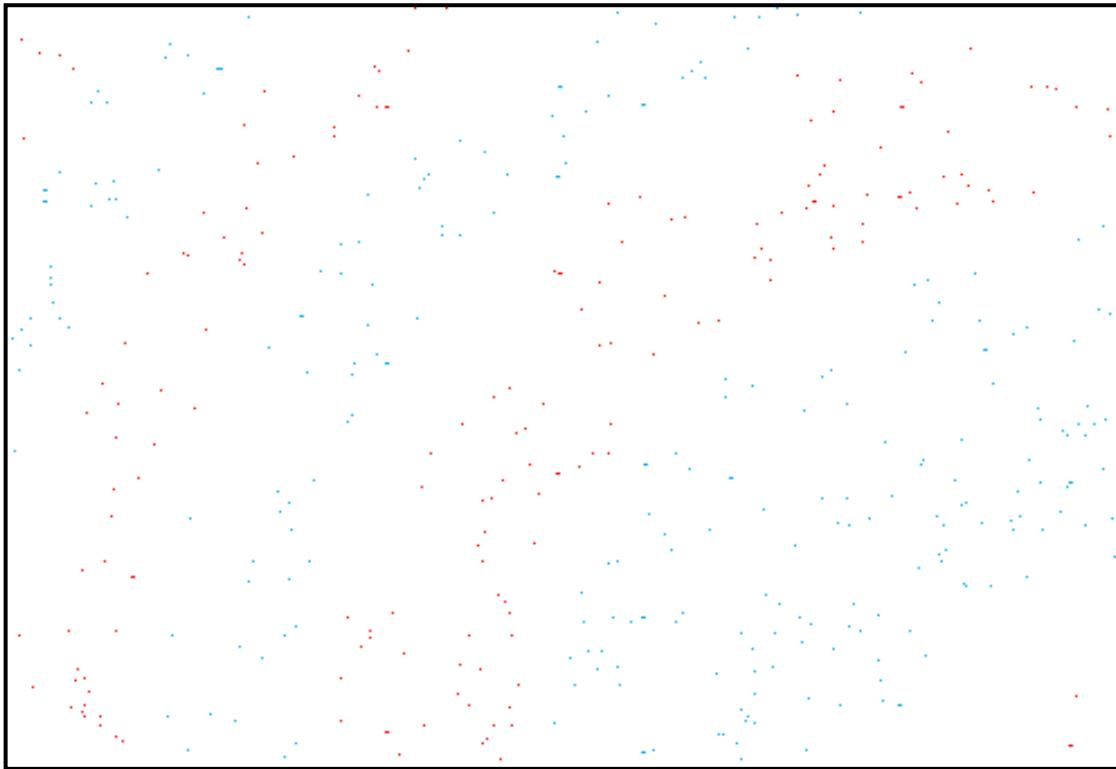


Figure 5.11: The upper left-hand corner of Fig. 5.10(b).

Once again, direct comparison of the experimentally obtained image of Fig. 5.11(a) and the simulated image of Fig. 5.11(b) is not possible, for the reasons given in the discussion of Fig. 5.10. As before, on the average only about 15 rays are available per pixel, and so the image is badly under-sampled making individual pixels difficult to discern. For that reason, the conditioning rule used to create Fig. 5.12(b) is:

If $0.0 \leq \text{intensity} \leq 0.01$, fill the cell with blue; and if $0.8 \leq \text{intensity} \leq 1.0$, fill the cell with red.

This results once again in a thin pattern of red flakes populating the “bright” rings (constructive interference), and a thin pattern of blue flakes populating the “dark” rings (destructive interference). In an attempt to improve the visibility of these pixels, the upper left-hand corner of Fig. 5.12 is reproduced to a larger scale in Fig. 5.13.

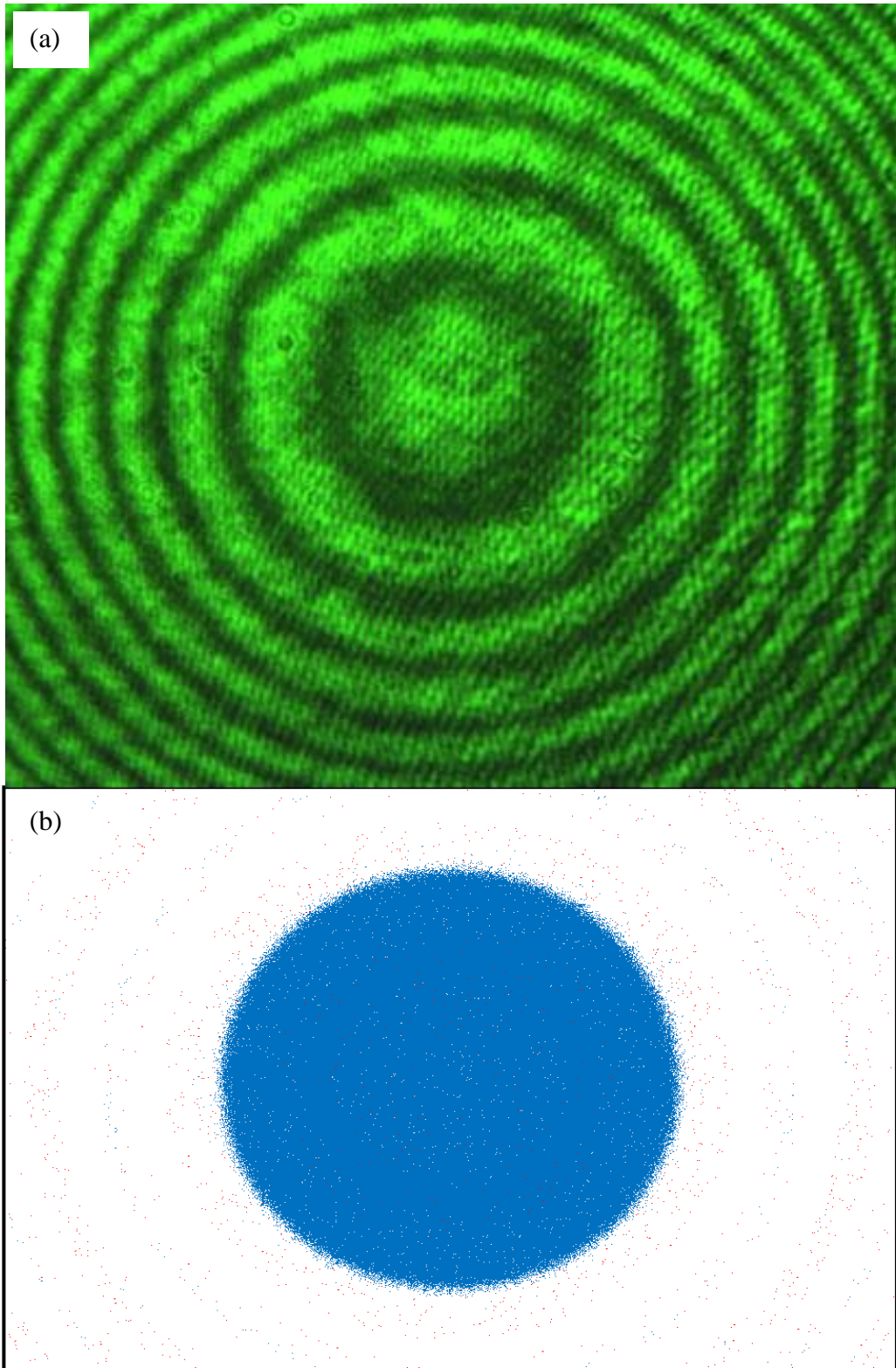


Figure 5.12: (a) Experimental image and (b) simulated image for the case of a two-inch path length difference between Beam A and Beam B.

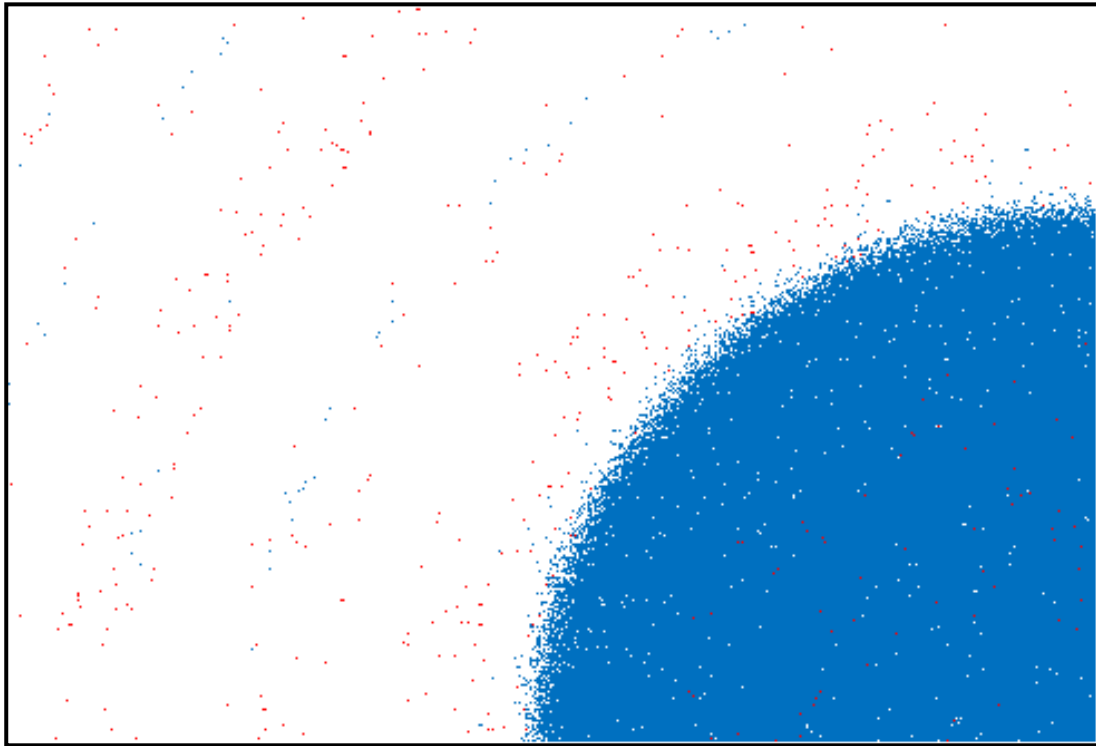


Figure 5.13: The upper left-hand corner of Fig. 5.12(b).

In summary, the Monte-Carlo ray-trace based simulation of the Michelson interferometer produces at least adequate agreement with the measured performance. In a head-to-head comparison, the simulated and experimentally obtained fringe orders are essentially the same.

Chapter 6: Conclusions and Recommendations

In this chapter the conclusions that can be drawn from the effort documented in this thesis are listed as well as recommendations for further research.

6.1 Conclusions

The following conclusions can be drawn from this effort:

1. Ray-trace-based simulation methodology has been demonstrated to be capable of simulating the performance of a Michelson interferometer.
2. Under-sampling problems arise when simulating an image from a high-resolution board-level camera because of limited available computing power and the resolution of available plotting tools.
3. When undertaking experimental validation of a numerical model it is important that the experimental apparatus be capable of yielding results with the desired level of accuracy

6.2 Recommendations

The following recommendations are made for future effort:

1. Before continuing with larger investigation, a research-grade Michelson interferometer must be obtained.
2. The numerical model should be implemented on a platform having a greater processing power than a typical laptop computer.
3. The numerical model should be used to investigate the response of the Michelson interferometer to quasi-monochromatic light.

References

Bennet, Jean M., McAllister, D. Theodore, and Cabe, Georgia M., "Albert A. Michelson, Dean of American Optics-Life, Contributions to Science, and Influence on Modern-Day Physics" *Applied Optics*, Vol. 12, pp. 2255-2256, October, 1973.

Dongen, Jeroen van, "On the Role of the Michelson–Morley Experiment: Einstein in Chicago", *Archive for History of Exact Sciences*, Vol. 63 No. 6, pp. 655–663, July, 2009.

Hecht, Eugene, *Optics 4th Edition*, Addison Wesley, San Francisco, California, 2002

Jaffe, Bernard, *Michelson and Speed of Light*, Anchor Books, Garden City, New York, 1960.

Kashyap, Kapil, Singh, Hardeep, Singh, Preeti, and Kumar, Kumar, "Compensation of Dispersion in Optical Fiber Using Fiber Bragg Grating" *International Journal of Advance Research in Science and Engineering*, IJARSE, Vol. 2, pp. 124, April, 2013.

Katz, Deborah M., *Physics for Scientist and Engineers: Foundations and Connections 1st Edition*, Wadsworth, Inc., Belmont, California, 2016.

Livingston, D.M., *The Master of Light, A Biography of Albert A. Michelson*, Scribner, New York, 1973.

Mahan, J. Robert, Barki, Anum R., and Priestly, Kory J." An Initiative to include coherence and polarization in Earth Radiation Budget Measurement" *Applied Optics*, Vol. 55, pp. D54-D59, December, 2016.

Mahan, Robert, *Radiation Heat Transfer*, John Wiley & Sons, Inc., New York, 2002

Pederotti, Frank L., Pedrotti,S.J., and Pedrotti, Leno M., *Introduction to Optics 3rd Edition*, Peason Education, Inc., Franklin Lakes, New Jersey, 2007.

Poynton, Charles A. "Rehabilitation of gamma", *Proc. SPIE 3299, Human Vision and Electronic Imaging III*, 232, July 17, 1998; doi:10.1117/12.320126.

Russell, Jesse, Cohn, Ronald, *Michelson Interferometer*, Book on Demand, Madison, Wisconsin, 2012.

Saleh, B.E.A, Teich, M.C., *Fundamentals of Photonics 2nd Edition*, John Wiley & Sons, Inc., Hoboken, NJ, 2007.

Serway, Raymond A., Vuille, Chris, *College Physics 9th Edition*, Brooks/Cole Publishing Co., Pacific Grove, 2015.

Stachel, John, "Einstein and Michelson: The Context of Discovery and Context of Justification", *Astronomische Nachrichten* Vol. 303 No. (1): 47–53, 1982.

Steel, W.H., *Interferometry 2nd Edition*, Cambridge University Press, New York, 1983.

Verdeye, Joseph T., *Laser Electronics 3rd Edition*, Prentice Hall, New Jersey, 1995.

Wolf, Emil, *Introduction to the Theory of Coherence and Polarization of Light*, Cambridge University Press, New York, 2007.

Appendix A: A Brief Biography of Albert A. Michelson

A logical starting point for this chapter is the life and times of the creator of the interferometer, Albert A. Michelson. This leads naturally to an in-depth discussion about the operating principles of his invention, the Michelson interferometer. The chapter concludes with a discussion of the concept of coherence and how it relates to the question posed in the previous chapter. The following brief summary of the life and career of Albert A. Michelson draws principally upon two published biographies: “Michelson and the Speed of Light” by Bernard Jaffe [1960], and “A Biography of Albert A. Michelson” by D. M. Livingston [1973]. Additional supplemental sources are cited where appropriate.

Albert Abraham Michelson was born in Strelno, Prussia, on December 19, 1852. Two years after his birth, the Michelson family moved to San Francisco, where he received his early education. After graduating from high school in 1859, young Michelson was appointed to the United States Naval Academy in Annapolis, Maryland, by President Ulysses S. Grant. Upon graduation from Annapolis in 1873 and after spending two years in the fleet, Michelson was appointed to the position of instructor of physics and chemistry at the Naval Academy, where he served from 1875 to 1879. He spent the following year at the Nautica Almanac Office in Washington, D.C., after which he traveled abroad for the next two years, as was the custom of young “gentlemen” of the time. While in Europe, he studied at the *Collège de France* and at the universities of Heidelberg and Berlin. In 1882, he was appointed to the position of professor of physics at the Case School of Applied Science in Cleveland, where he remained until 1889. It was at Case that he entered into a very fruitful collaboration with Edward W. Morley.

Together Michelson and Morley conducted the celebrated research that eventually led to the award of the 1907 Nobel Prize in Physics. Following a brief appointment as professor of physics at Clark University from 1889 to 1892, he was named professor and head of the Department of Physics at the University of Chicago in 1892. He held this position until he was forced by reason of failing health to resign in 1929. He would later become emeritus professor shortly before his death in 1931.

Michelson made several significant contributions to the field of optics. One of his early contributions was made while at the Naval Academy in Annapolis in 1877, where he was tasked with developing a demonstration of Foucault's method for measuring the velocity of light. His apparatus was based on Foucault's original design of 1862. Both Foucault's design and Michelson's improvement incorporated two plane mirrors, one fixed and one revolving at the rate of about 130 R/s. Using his improved design Michelson measured a velocity of 186,508 M/s, deemed the most accurate value available at the time. This effort brought him his first recognition as a scientist. It was during his time in Berlin that Michelson was able to modify Foucault's original approach for measuring the velocity of light. His new device, which was intended to confirm the existence of the so-called *luminiferous aether*, was capable of detecting subtle changes in the speed of light. It eventually came to be called the Michelson Interferometer.

According to Russell and Cohn [2012], A Michelson Interferometer introduces a beam of light to a beam splitter orientated at a 45-deg angle. The two beams produced are directed down mutually perpendicular paths. The beams, after being reflected from the fixed plane mirror, return to the beam splitter where they are recombined. The recombined beam is then transmitted to a viewing plane, where it produces an

interference pattern. Characteristics of the interference pattern depend on the coherence of the source, the path length difference between the two beams of light, and the medium through which the beams propagate. Contemporary understanding of sound as a wave required molecular vibration within in a medium, such as air. Therefore, it was commonly assumed that light also needed the molecules assumed to be make up the luminiferous aether in order to propagate. Michelson postulated that the aether was stationary and formed an absolute reference frame with respect to the universe. It would therefore follow that it should appear to be moving from the perspective of an observer on the sun-orbiting Earth. Thus, it was hypothesized that light would sometimes travel in the same direction as the relative motion of the aether, and other times in the opposite direction. Michelson's idea was to measure the speed of light in different directions in order to measure the speed of the aether relative to Earth, thus establishing its existence.

According to Russell and Cohn [2012], Michelson knew in 1878 that the velocity of the Earth was about 30 km/s. Based on that knowledge, he predicted that using a 600-nm light source, the presence of the stationary luminiferous aether would create a path length difference of about 0.04 nm which would result in an observable displacement in the fringe pattern produced as the apparatus was rotated 360 deg. When he conducted the experiment, he was unable to detect the expected displacement in the fringe pattern due to the aether. However, Michelson continued to refine his apparatus in the hope of detecting the luminiferous aether. In 1882, while at the Case School of Applied Science in Cleveland, he collaborated with Edward Morley. Morley contributed further improvements to Michelson's initial design resulting in an improved iteration of the apparatus, called the *Michelson-Morley interferometer*. The new apparatus was very

similar to Michelson's original design but was much more sensitive. Several factors contributed to this increase in sensitivity. First, the new apparatus incorporated more mirrors which permitted the use of longer path lengths. Second, the new apparatus was located in a basement which reduced uncertainties caused by building vibrations. Finally, the apparatus was mounted on a rotatable stone block floating in a mercury-filled basin. Even with this exquisitely sensitive apparatus, Michelson and Morley were unable to detect the aether. Nonetheless, Michelson and Morley's experiment revolutionized physics. When Albert Einstein published his groundbreaking theory of special relativity, he abandoned the aether concept [Doegan, 2009]. In 1909, Michelson received an honorary PhD from the University of Leipzig, Germany.

There is some debate about whether the Michelson–Morley experiment influenced Einstein's reasoning as he elaborated the theory of special relativity. Referencing some of Einstein's interviews, many historians argue that based on his statements the experiments played no significant role in his thought process, while others insist that his statements suggest that he was influenced by the Michelson-Morley experiment [Doegan, 2009]. Regardless of what the critics claim, the Michelson-Morley experiment was an important early contribution to the notion of the constancy of the speed of light.

Appendix B: Beam A (Mirror 1) Matlab Code

```
% Michelson Interferometer Simulation Mirror 1%

clear;
clc;
close all;

% Define Variables %

WaveLength = 532.0; % Wavelength(nm)
WaveLength = WaveLength * 10 ^-6; % Conversion from (nm) to (mm)
rSource = 2.4 ;    % Radius laser module aperture (mm)
ThetaMax = 0.0;   % Maximum cone angle for the bundle launched from source
rayCount = 1000000; % Number or rays launched
rCurve = 76.6;    % Radius of Curvature of the lens (mm)
LensThickness = 4.1; % Thickness of the focusing Lens (mm)
zLens = 5.0;      % Distance from tip of laser diode to the center of lens mount (mm)
zCFront = zLens - ( LensThickness / 2.0 ) + rCurve; % zCFront is the distance from the
source to the fornt hemsisphere of the lens (mm)
zCBack = zLens + ( LensThickness / 2.0 ) - rCurve; % zCBack is the distance from the
source to the back hemisphere of the lens (mm)
xPrimeS = - 152.4; % x-coordinate location for Focal Plane Array (mm)
yPrimeS = 0.0;    % y-coordinate location for Focal Plane Array (mm)
zPrimeS = 127.0;  % z-coordinate location for Focal Plane Array (mm)
xPrime1 = 101.6;  % x-coordinate location for Mirror 1 (mm)
yPrime1 = 0.0;    % y-coordinate location for Mirror 1 (mm)
zPrime1 = 127.0;  % z-coordinate location for Mirror 1 (mm)
xPrimeB = 0.0;    % x-coordinate location for Beamsplitter (mm)
yPrimeB = 0.0;    % y-coordinate location for Beamsplitter (mm)
zPrimeB = 127.0;  % z-coordinate location for Beamsplitter (mm)
xRange = 200.0;   % Negative to Postive x- value plot range (mm)
yRange = 140.0;   % Negative to Postive y- value plot range (mm)
zMINUSRange = 0.0; % Negative z-value plot range (mm)
zPLUSRange = 200.0; % Positive z-value plot range (mm)
n1 = 1.002772;    % Refractive index of air
n2 = 1.51681;     % Refrative index of lens
factor = 10.0;
PixelHeight = 0.005 * factor; % The dimension of the pixel height (mm)
PixelWidth = 0.005 * factor;  % The dimension of the pixel width (mm)
M = floor( 686 / factor );    % # of Rows or Height of Array
N = floor( 960 / factor );    % # of Coulumns or Width of Array
format long      % Activate 15 significant digits

%%% Initialize Matrices %%%
```

```
X1 = zeros( rayCount, 1 );
Y1 = zeros( rayCount, 1 );
Z1 = zeros( rayCount, 1 );
X2 = zeros( rayCount, 1 );
Y2 = zeros( rayCount, 1 );
Z2 = zeros( rayCount, 1 );
X3 = zeros( rayCount, 1 );
Y3 = zeros( rayCount, 1 );
Z3 = zeros( rayCount, 1 );
X4 = zeros( rayCount, 1 );
Y4 = zeros( rayCount, 1 );
Z4 = zeros( rayCount, 1 );
X5 = zeros( rayCount, 1 );
Y5 = zeros( rayCount, 1 );
Z5 = zeros( rayCount, 1 );
X6 = zeros( rayCount, 1 );
Y6 = zeros( rayCount, 1 );
Z6 = zeros( rayCount, 1 );
X7 = zeros( rayCount, 1 );
Y7 = zeros( rayCount, 1 );
Z7 = zeros( rayCount, 1 );
X8 = zeros( rayCount, 1 );
Y8 = zeros( rayCount, 1 );
Z8 = zeros( rayCount, 1 );
X9 = zeros( rayCount, 1 );
Y9 = zeros( rayCount, 1 );
Z9 = zeros( rayCount, 1 );
X10 = zeros( rayCount, 1 );
Y10 = zeros( rayCount, 1 );
Z10 = zeros( rayCount, 1 );
X11 = zeros( rayCount, 1 );
Y11 = zeros( rayCount, 1 );
Z11 = zeros( rayCount, 1 );
X12 = zeros( rayCount, 1 );
Y12 = zeros( rayCount, 1 );
Z12 = zeros( rayCount, 1 );
XX = zeros( 2, 1 );
YY = zeros( 2, 1 );
ZZ = zeros( 2, 1 );
MM = zeros( rayCount, 1 );
NN = zeros( rayCount, 1 );
P1 = zeros( 1000, 1000 );
Count1 = zeros( 1000, 1000 );
P1average = zeros( 1000, 1000);
```

```
for a = 1 : rayCount
```

% Source Coordinates (Surface 1) %

[x0, y0, z0, L0, M0, N0] = Find_Source_Coordinates(rSource, ThetaMax);

X1(a) = x0;

Y1(a) = y0;

Z1(a) = z0;

% Front of Lens Coordinates (Surface 2) %

[x1, y1, z1, L1, M1, N1] = LENSFRONTINPUT(rCurve, zCFront, x0, y0, z0, L0, M0, N0);

X2(a) = x1;

Y2(a) = y1;

Z2(a) = z1;

% Front of Lens Output Coordinates (Surface 3) %

[x0, y0, z0, L0, M0, N0] = LENSFRONTOUTPUT(rCurve, zCFront, n1, n2, x1, y1, z1, L1, M1, N1);

X3(a) = x0;

Y3(a) = y0;

Z3(a) = z0;

% Back of Lens Input Coordinates (Surface 4) %

[x1, y1, z1, L1, M1, N1] = LENSBACKINPUT(rCurve, zCBack, x0, y0, z0, L0, M0, N0);

X4(a) = x1;

Y4(a) = y1;

Z4(a) = z1;

% Back of Lens Output Coordinates (Surface 5) %

[x0, y0, z0, L0, M0, N0] = LENSBACKOUTPUT(rCurve, zCBack, n1, n2, x1, y1, z1, L1, M1, N1);

X5(a) = x0;

Y5(a) = y0;

Z5(a) = z0;

% Beamsplitter Input Coordinates (Surface 6) %

```
[ x1, y1, z1, L1, M1, N1 ] = BEAMSPLITTERINPUT1( xPrimeB, yPrimeB, zPrimeB ,  
x0, y0, z0, L0, M0, N0 );
```

```
X6( a ) = x1;
```

```
Y6( a ) = y1;
```

```
Z6( a ) = z1;
```

```
% Beamsplitter Output Coordinates (Surface 7) %
```

```
[x0, y0, z0, L0, M0, N0 ] = BEAMSPLITTEROUTPUT1( x1, y1, z1, L1, M1, N1 );
```

```
X7( a ) = x0;
```

```
Y7( a ) = y0;
```

```
Z7( a ) = z0;
```

```
% Mirror Input Coordinates (Surface 8) %
```

```
[ x1, y1, z1, L1, M1, N1 ] = MIRROR1INPUT( xPrime1, yPrime1, zPrime1, x0, y0, z0,  
L0, M0, N0 );
```

```
X8( a ) = x1;
```

```
Y8( a ) = y1;
```

```
Z8( a ) = z1;
```

```
% Mirror Output Coordinates (Surface 9) %
```

```
[ x0, y0, z0, L0, M0, N0 ] = MIRROR1OUTPUT( x1, y1, z1, L1, M1, N1 );
```

```
X9( a ) = x0;
```

```
Y9( a ) = y0;
```

```
Z9( a ) = z0;
```

```
% Beamsplitter plane Input Coordinates (Surface 10) %
```

```
% [ x1, y1, z1, L1, M1, N1, t1 ] = BEAMSPLITTERINPUT1Plane( xPrimeB, yPrimeB,  
zPrimeB , x0, y0, z0, L0, M0, N0 );
```

```
%
```

```
% X10( a ) = x1;
```

```
% Y10( a ) = y1;
```

```
% Z10( a ) = z1;
```

```
% t1Surface10( a ) = t1;
```

```
%
```

```
% % Beamsplitter plane Output Coordinates (Surface 11) %
```

```
%
```

```

% [ x0, y0, z0, L0, M0, N0 ] = BEAMSPLITTEROUTPUT1Plane( xPrimeB, yPrimeB,
zPrimeB, x1, y1, z1, L1, M1, N1);
%
% X11( a ) = x0;
% Y11( a ) = y0;
% Z11( a ) = z0;

% Focal Plane Array Input Coordinates (Surface 10) %

[ x1, y1, z1 ] = FOCALPLANEARRAYINPUT( xPrimeS, yPrimeS, zPrimeS, x0, y0, z0,
L0, M0, N0);

X12( a ) = x1;
Y12( a ) = y1;
Z12( a ) = z1;

% Calculate total distance traveled by each ray %

deltax = X2(a) - X1(a);
deltay = Y2(a) - Y1(a);
deltaz = Z2(a) - Z1(a);
deltaxSq = deltax.*deltax;
deltaySq = deltax.*deltay;
deltazSq = deltax.*deltaz;
mag12 = sqrt(deltaxSq + deltaxSq + deltaxSq);

deltax = X4(a) - X2(a);
deltay = Y4(a) - Y2(a);
deltaz = Z4(a) - Z2(a);
deltaxSq = deltax.*deltax;
deltaySq = deltax.*deltay;
deltazSq = deltax.*deltaz;
mag24 = sqrt(deltaxSq + deltaxSq + deltaxSq);

deltax = X6(a) - X4(a);
deltay = Y6(a) - Y4(a);
deltaz = Z6(a) - Z4(a);
deltaxSq = deltax.*deltax;
deltaySq = deltax.*deltay;
deltazSq = deltax.*deltaz;
mag46 = sqrt(deltaxSq + deltaxSq + deltaxSq);

deltax = X8(a) - X6(a);
deltay = Y8(a) - Y6(a);

```

```

deltaz = Z8(a) - Z6(a);
deltaxSq = deltax.*deltax;
deltaySq = deltax.*deltax;
deltazSq = deltax.*deltax;
mag68 = sqrt(deltaxSq + deltaxSq + deltaxSq);

deltax = X12(a) - X8(a);
deltay = Y12(a) - Y8(a);
deltaz = Z12(a) - Z8(a);
deltaxSq = deltax.*deltax;
deltaySq = deltax.*deltax;
deltazSq = deltax.*deltax;
mag812 = sqrt(deltaxSq + deltaxSq + deltaxSq);

t1total = mag12 + mag24 + mag46 + mag68 + mag812;

Remainder = t1total / WaveLength - floor( t1total / WaveLength );
p1 = 2.0 * pi * Remainder;

if y1 >= ( - M * PixelHeight / 2.0 ) && y1 <= ( M * PixelHeight / 2.0 )
    m = 1 + ( M - 1 ) * ( y1 + M * PixelHeight / 2.0 ) / ( M * PixelHeight );
    m = floor( m );
else
    m = 1000;
end

MM( a ) = m;

if z1 >= ( zPrimeS - N * PixelWidth / 2.0 ) && z1 <= ( zPrimeS + N * PixelWidth / 2.0 )
    n = 1 + ( N - 1 ) * ( z1 - zPrimeS + N * PixelWidth / 2.0 ) / ( N * PixelWidth );
    n = floor( n );
else
    n = 1000;
end

NN( a ) = n;

Count1( m, n ) = Count1( m, n ) + 1;

P1( m, n ) = P1( m, n ) + p1;

end % End of a loop %

for m = 1 : M
    for n = 1 : N
        if Count1( m, n ) ~= 0.0

```

```

        P1average( m, n ) = P1( m ,n ) / Count1( m, n );
    else
        P1average( m, n ) = 0.0;
    end
end
end

% Export array data into a xlsx. file %
filename = 'Count1.xlsx';
xlswrite( filename, Count1 )

filename = 'P1.xlsx';
xlswrite( filename, P1average )

% Plot %

% scatter3( X1, Y1, Z1, '.', 'r' ), xlabel ( 'X' ), ylabel ( 'Y' ), zlabel ( 'Z' ), xlim ( [ -xRange
xRange ] ), ylim ( [ -yRange yRange ] ), zlim ( [ zMINUSRange zPLUSRange ] );
% hold on
%
% scatter3( X2, Y2, Z2, '.', 'r' ), xlabel ( 'X' ), ylabel ( 'Y' ), zlabel ( 'Z' ), xlim ( [ -xRange
xRange ] ), ylim ( [ -yRange yRange ] ), zlim ( [ zMINUSRange zPLUSRange ] );
% hold on;
%
% for i = 1:rayCount
% XX(1) = X1( i );
% YY(1) = Y1( i );
% ZZ(1) = Z1( i );
% XX(2) = X2( i );
% YY(2) = Y2( i );
% ZZ(2) = Z2( i );
% plot3( XX, YY, ZZ )
% end
%
% scatter3( X3, Y3, Z3, '.', 'r' ), xlabel ( 'X' ), ylabel ( 'Y' ), zlabel ( 'Z' ), xlim ( [ -xRange
xRange ] ), ylim ( [ -yRange yRange ] ), zlim ( [ zMINUSRange zPLUSRange ] );
% hold on
%
% for i = 1:rayCount
% XX(1) = X2( i );
% YY(1) = Y2( i );
% ZZ(1) = Z2( i );
% XX(2) = X3( i );
% YY(2) = Y3( i );
% ZZ(2) = Z3( i );
% plot3( XX, YY, ZZ )

```

```

% end
%
% scatter3( X4, Y4, Z4, '.', 'r' ), xlabel ( 'X' ), ylabel ( 'Y' ), zlabel ( 'Z' ), xlim ( [ -xRange
xRange ] ), ylim ( [ -yRange yRange ] ), zlim ( [ zMINUSRange zPLUSRange ] );
% hold on
%
% for i = 1:rayCount
% XX(1) = X3( i );
% YY(1) = Y3( i );
% ZZ(1) = Z3( i );
% XX(2) = X4( i );
% YY(2) = Y4( i );
% ZZ(2) = Z4( i );
% plot3( XX, YY, ZZ )
% end
%
% scatter3( X5, Y5, Z5, '.', 'r' ), xlabel ( 'X' ), ylabel ( 'Y' ), zlabel ( 'Z' ), xlim ( [ -xRange
xRange ] ), ylim ( [ -yRange yRange ] ), zlim ( [ zMINUSRange zPLUSRange ] );
% hold on
%
% for i = 1:rayCount
% XX(1) = X4( i );
% YY(1) = Y4( i );
% ZZ(1) = Z4( i );
% XX(2) = X5( i );
% YY(2) = Y5( i );
% ZZ(2) = Z5( i );
% plot3( XX, YY, ZZ )
% end
%
% scatter3( X6, Y6, Z6, '.', 'r' ), xlabel ( 'X' ), ylabel ( 'Y' ), zlabel ( 'Z' ), xlim ( [ -xRange
xRange ] ), ylim ( [ -yRange yRange ] ), zlim ( [ zMINUSRange zPLUSRange ] );
% hold on
%
% for i = 1:rayCount
% XX(1) = X5( i );
% YY(1) = Y5( i );
% ZZ(1) = Z5( i );
% XX(2) = X6( i );
% YY(2) = Y6( i );
% ZZ(2) = Z6( i );
% plot3( XX, YY, ZZ )
% end
%
% scatter3( X7, Y7, Z7, '.', 'r' ), xlabel ( 'X' ), ylabel ( 'Y' ), zlabel ( 'Z' ), xlim ( [ -xRange
xRange ] ), ylim ( [ -yRange yRange ] ), zlim ( [ zMINUSRange zPLUSRange ] );

```

```

% hold on
%
% for i = 1:rayCount
% XX(1) = X6( i );
% YY(1) = Y6( i );
% ZZ(1) = Z6( i );
% XX(2) = X7( i );
% YY(2) = Y7( i );
% ZZ(2) = Z7( i );
% plot3( XX, YY, ZZ)
% end
%
% scatter3( X8, Y8, Z8, '.', 'r' ), xlabel ( 'X' ), ylabel ( 'Y' ), zlabel ( 'Z' ), xlim ( [ -xRange
xRange ] ), ylim ( [ -yRange yRange ] ), zlim ( [ zMINUSRange zPLUSRange ] ) ;
% hold on
%
% for i = 1:rayCount
% XX(1) = X7( i );
% YY(1) = Y7( i );
% ZZ(1) = Z7( i );
% XX(2) = X8( i );
% YY(2) = Y8( i );
% ZZ(2) = Z8( i );
% plot3( XX, YY, ZZ)
% end
%
% scatter3( X9, Y9, Z9, '.', 'r' ), xlabel ( 'X' ), ylabel ( 'Y' ), zlabel ( 'Z' ), xlim ( [ -xRange
xRange ] ), ylim ( [ -yRange yRange ] ), zlim ( [ zMINUSRange zPLUSRange ] ) ;
% hold on
%
% for i = 1:rayCount
% XX(1) = X8( i );
% YY(1) = Y8( i );
% ZZ(1) = Z8( i );
% XX(2) = X9( i );
% YY(2) = Y9( i );
% ZZ(2) = Z9( i );
% plot3( XX, YY, ZZ)
% end
%
% scatter3( X10, Y10, Z10, '.', 'r' ), xlabel ( 'X' ), ylabel ( 'Y' ), zlabel ( 'Z' ), xlim ( [ -
xRange xRange ] ), ylim ( [ -yRange yRange ] ), zlim ( [ zMINUSRange zPLUSRange ] )
;
% hold on
%
% for i = 1:rayCount

```

```

% XX(1) = X9(i);
% YY(1) = Y9(i);
% ZZ(1) = Z9(i);
% XX(2) = X10(i);
% YY(2) = Y10(i);
% ZZ(2) = Z10(i);
% plot3( XX, YY, ZZ)
% end
%
% scatter3( X11, Y11, Z11, '.', 'r' ), xlabel ( 'X' ), ylabel ( 'Y' ), zlabel ( 'Z' ), xlim ( [ -
xRange xRange ] ), ylim ( [ -yRange yRange ] ), zlim ( [zMINUSRange zPLUSRange ] )
;
% hold on
%
% for i = 1:rayCount
% XX(1) = X10(i);
% YY(1) = Y10(i);
% ZZ(1) = Z10(i);
% XX(2) = X11(i);
% YY(2) = Y11(i);
% ZZ(2) = Z11(i);
% plot3( XX, YY, ZZ)
% end
%
% scatter3( X12, Y12, Z12, '.', 'r' ), xlabel ( 'X' ), ylabel ( 'Y' ), zlabel ( 'Z' ), xlim ( [ -
xRange xRange ] ), ylim ( [ -yRange yRange ] ), zlim ( [zMINUSRange zPLUSRange ] )
;
% hold on
%
% for i = 1:rayCount
% XX(1) = X11(i);
% YY(1) = Y11(i);
% ZZ(1) = Z11(i);
% XX(2) = X12(i);
% YY(2) = Y12(i);
% ZZ(2) = Z12(i);
% plot3( XX, YY, ZZ)
% end
%
% c = ITotal;
% scatter3( MM, NN, ITotal, 1, c ), xlabel ( 'Row' ), ylabel ( 'Column' ), zlabel ( 'T' ), xlim
( [ 1 686 ] ), ylim ( [ 1 960 ] ), zlim ( [ 0 1 ] ), colormap( gray ), caxis([ 0, 1 ]), colorbar ;
% az = 0;
% el = 90;
% view( az, el );

```

Appendix C: Beam B (Mirror 2) Matlab Code

```
% Michelson Interferometer Simulation Mirror 2%

clear;
clc;
close all;

% Define Variables %

WaveLength = 532.0; % Wavelength(nm)
WaveLength = WaveLength * 10 ^ - 6; % Conversion from (nm) to (mm)
rSource = 2.4 ;    % Radius laser module aperture (mm)
ThetaMax = 0.0;   % Maximum cone angle for the bundle launched from source
rayCount = 1000000; % Number of rays launched
rCurve = 76.6;    % Radius of Curvature of the lens (mm)
LensThickness = 4.1; % Thickness of the focusing Lens (mm)
zLens = 5.0;      % Distance from tip of laser diode to the center of lens mount (mm)
zCFront = zLens - ( LensThickness / 2.0 ) + rCurve ; % zCFront is the distance from the
source to the front hemisphere of the lens (mm)
zCBack = zLens + ( LensThickness / 2.0 ) - rCurve; % zCBack is the distance from the
source to the back hemisphere of the lens (mm)
xPrimeS = - 152.4; % x-coordinate location for Focal Plane Array (mm)
yPrimeS = 0.0;    % y-coordinate location for Focal Plane Array (mm)
zPrimeS = 127.0;  % z-coordinate location for Focal Plane Array (mm)
xPrime2 = 0.0;   % x-coordinate location for Mirror 2 (mm)
yPrime2 = 0.0;   % y-coordinate location for Mirror 2 (mm)
zPrime2 = 203.2; % z-coordinate location for Mirror 2 (mm)
xPrimeB = 0.0;   % x-coordinate location for Beamsplitter (mm)
yPrimeB = 0.0;   % y-coordinate location for Beamsplitter (mm)
zPrimeB = 127.0; % z-coordinate location for Beamsplitter (mm)
xRange = 5.0;    % Negative to Positive x- value plot range (mm)
yRange = 5.0;    % Negative to Positive y- value plot range (mm)
zMINUSRange = 431.0; % Negative z-value plot range (mm)
zPLUSRange = 433.0; % Positive z-value plot range (mm)
n1 = 1.002772;   % Refractive index of air
n2 = 1.51681;    % Refractive index of lens
factor = 10.0;

PixelHeight = 0.005 * factor; % The dimension of the pixel height (mm)
PixelWidth = 0.005 * factor; % The dimension of the pixel width (mm)
M = floor( 686 / factor );    % # of Rows or Height of Array
N = floor( 960 / factor );    % # of Columns or Width of Array

format long      % Activate 15 significant digits
```

```
%%% Initialize Matrices %%%
```

```
X1 = zeros( rayCount, 1 );  
Y1 = zeros( rayCount, 1 );  
Z1 = zeros( rayCount, 1 );  
X2 = zeros( rayCount, 1 );  
Y2 = zeros( rayCount, 1 );  
Z2 = zeros( rayCount, 1 );  
X3 = zeros( rayCount, 1 );  
Y3 = zeros( rayCount, 1 );  
Z3 = zeros( rayCount, 1 );  
X4 = zeros( rayCount, 1 );  
Y4 = zeros( rayCount, 1 );  
Z4 = zeros( rayCount, 1 );  
X5 = zeros( rayCount, 1 );  
Y5 = zeros( rayCount, 1 );  
Z5 = zeros( rayCount, 1 );  
X6 = zeros( rayCount, 1 );  
Y6 = zeros( rayCount, 1 );  
Z6 = zeros( rayCount, 1 );  
X7 = zeros( rayCount, 1 );  
Y7 = zeros( rayCount, 1 );  
Z7 = zeros( rayCount, 1 );  
X8 = zeros( rayCount, 1 );  
Y8 = zeros( rayCount, 1 );  
Z8 = zeros( rayCount, 1 );  
X9 = zeros( rayCount, 1 );  
Y9 = zeros( rayCount, 1 );  
Z9 = zeros( rayCount, 1 );  
X10 = zeros( rayCount, 1 );  
Y10 = zeros( rayCount, 1 );  
Z10 = zeros( rayCount, 1 );  
X11 = zeros( rayCount, 1 );  
Y11 = zeros( rayCount, 1 );  
Z11 = zeros( rayCount, 1 );  
X12 = zeros( rayCount, 1 );  
Y12 = zeros( rayCount, 1 );  
Z12 = zeros( rayCount, 1 );  
XX = zeros( 2, 1 );  
YY = zeros( 2, 1 );  
ZZ = zeros( 2, 1 );  
MM = zeros( rayCount, 1 );  
NN = zeros( rayCount, 1 );  
P2 = zeros( 1000, 1000 );  
Count2 = zeros( 1000, 1000 );  
P2average = zeros( 1000, 1000 );
```

```

for i = 1:rayCount

% Source Coordinates %

[ x0, y0, z0, L0, M0, N0 ] = Find_Source_Coordinates( rSource, ThetaMax );

X1( i ) = x0;
Y1( i ) = y0;
Z1( i ) = z0;

% Intersection of rays at the Front of Lens %

[ x1, y1, z1, L1, M1, N1 ] = LENSFRONTINPUT( rCurve, zCFront, x0, y0, z0, L0, M0,
N0 );

X2( i ) = x1;
Y2( i ) = y1;
Z2( i ) = z1;

% Intersection of rays leaving front hemisphere of Lens %

[ x0, y0, z0, L0, M0, N0 ] = LENSFRONTOUTPUT( rCurve, zCFront, n1, n2, x1, y1, z1,
L1, M1, N1 );

X3( i ) = x0;
Y3( i ) = y0;
Z3( i ) = z0;

% Intersection of the rays intersecting the back hemisphere of the Lens %

[ x1, y1, z1, L1, M1, N1 ] = LENSBACKINPUT( rCurve, zCBack, x0, y0, z0, L0, M0,
N0 );

X4( i ) = x1;
Y4( i ) = y1;
Z4( i ) = z1;

[ x0, y0, z0, L0, M0, N0 ] = LENSBACKOUTPUT( rCurve, zCBack, n1, n2, x1, y1, z1,
L1, M1, N1 );

X5( i ) = x0;
Y5( i ) = y0;
Z5( i ) = z0;

```

```

% [ x1, y1, z1, L1, M1, N1 ] = BEAMSPLITTERINPUT2Plane( xPrimeB, yPrimeB,
zPrimeB , x0, y0, z0, L0, M0, N0 );
%
% X6( i ) = x1;
% Y6( i ) = y1;
% Z6( i ) = z1;
%
%
% [ x0, y0, z0, L0, M0, N0 ] = BEAMSPLITTEROUTPUT2Plane( x1, y1, z1, L1, M1,
N1 );
%
% X7( i ) = x0;
% Y7( i ) = y0;
% Z7( i ) = z0;

[ x1, y1, z1, L1, M1, N1 ] = MIRROR2INPUT( xPrime2, yPrime2, zPrime2, x0, y0, z0,
L0, M0, N0 );

X8( i ) = x1;
Y8( i ) = y1;
Z8( i ) = z1;

[ x0, y0, z0, L0, M0, N0 ] = MIRROR2OUTPUT( x1, y1, z1, L1, M1, N1 );

X9( i ) = x0;
Y9( i ) = y0;
Z9( i ) = z0;

[ x1, y1, z1, L1, M1, N1 ] = BEAMSPLITTERINPUT2( xPrimeB, yPrimeB ,zPrimeB, x0,
y0, z0, L0, M0, N0 );

X10( i ) = x1;
Y10( i ) = y1;
Z10( i ) = z1;

[ x0, y0, z0, L0, M0, N0 ] = BEAMSPLITTEROUTPUT2( x1, y1, z1, L1, M1, N1 );

X11( i ) = x1;
Y11( i ) = y1;
Z11( i ) = z1;

[ x1, y1, z1 ] = FOCALPLANEARRAYINPUT( xPrimeS, yPrimeS, zPrimeS, x0, y0, z0,
L0, M0, N0);

X12( i ) = x1;

```

```
Y12(i) = y1;  
Z12(i) = z1;
```

```
% Calculate total distance traveled by each ray %
```

```
deltax = X2(i) - X1(i);  
deltay = Y2(i) - Y1(i);  
deltaz = Z2(i) - Z1(i);  
deltaxSq = deltax.*deltax;  
deltaySq = deltax.*deltax;  
deltazSq = deltax.*deltax;  
mag12 = sqrt(deltaxSq + deltaxSq + deltaxSq);
```

```
deltax = X4(i) - X2(i);  
deltay = Y4(i) - Y2(i);  
deltaz = Z4(i) - Z2(i);  
deltaxSq = deltax.*deltax;  
deltaySq = deltax.*deltax;  
deltazSq = deltax.*deltax;  
mag24 = sqrt(deltaxSq + deltaxSq + deltaxSq);
```

```
deltax = X8(i) - X4(i);  
deltay = Y8(i) - Y4(i);  
deltaz = Z8(i) - Z4(i);  
deltaxSq = deltax.*deltax;  
deltaySq = deltax.*deltax;  
deltazSq = deltax.*deltax;  
mag84 = sqrt(deltaxSq + deltaxSq + deltaxSq);
```

```
deltax = X10(i) - X8(i);  
deltay = Y10(i) - Y8(i);  
deltaz = Z10(i) - Z8(i);  
deltaxSq = deltax.*deltax;  
deltaySq = deltax.*deltax;  
deltazSq = deltax.*deltax;  
mag108 = sqrt(deltaxSq + deltaxSq + deltaxSq);
```

```
deltax = X12(i) - X10(i);  
deltay = Y12(i) - Y10(i);  
deltaz = Z12(i) - Z10(i);  
deltaxSq = deltax.*deltax;  
deltaySq = deltax.*deltax;  
deltazSq = deltax.*deltax;  
mag1210 = sqrt(deltaxSq + deltaxSq + deltaxSq);
```

```
t2total = mag12 + mag24 + mag84 + mag108 + mag1210;
```

```

Remainder = t2total / WaveLength - floor( t2total / WaveLength );
p2 = 2.0 * pi * Remainder;

if y1 >= ( - M * PixelHeight / 2.0 ) && y1 < ( M * PixelHeight / 2.0 )
    m = 1 + ( M - 1 ) * ( y1 + M * PixelHeight / 2.0 ) / ( M * PixelHeight );
    m = floor( m );
else
    m = 1000;
end

MM( i ) = m;

if z1 >= ( zPrimeS - N * PixelWidth / 2.0 ) && z1 < ( zPrimeS + N * PixelWidth / 2.0 )
    n = 1 + ( N - 1 ) * ( z1 - zPrimeS + N * PixelWidth / 2.0 ) / ( N * PixelWidth );
    n = floor( n );
else
    n = 1000;
end

NN( i ) = n;

Count2( m, n ) = Count2( m, n ) + 1;

P2( m, n ) = P2( m, n ) + p2;

end % End of i loop %

for m = 1 : M
    for n = 1 : N
        if Count2( m, n ) ~= 0.0
            P2average( m, n ) = P2( m, n ) / Count2( m, n );
        else
            P2average( m, n ) = 0.0;
        end
    end
end

% Export array data into a xlsx. file %
filename = 'Count2.xlsx';
xlswrite( filename, Count2 )

filename = 'P2.xlsx';
xlswrite( filename, P2average )

```

```

% scatter3( Y12, Z12, T2total, '.', 'r' ), xlabel ( 'Y' ), ylabel ( 'Z' ), zlabel ( 'T' ), xlim ( [ -
xRange xRange ] ), ylim ( [ 120 134 ] ), zlim ( [ zMINUSRange zPLUSRange ] );
% az = 0;
% el = 90;
% view( az, el );
% hold on
% scatter3( X1, Y1, Z1, '.', 'r' ), xlabel ( 'X' ), ylabel ( 'Y' ), zlabel ( 'Z' ), xlim ( [ -xRange
xRange ] ), ylim ( [ -yRange yRange ] ), zlim ( [ zMINUSRange zPLUSRange ] );
% hold on
%
% scatter3( X2, Y2, Z2, '.', 'r' ), xlabel ( 'X' ), ylabel ( 'Y' ), zlabel ( 'Z' ), xlim ( [ -xRange
xRange ] ), ylim ( [ -yRange yRange ] ), zlim ( [ zMINUSRange zPLUSRange ] );
% hold on;
%
% for i = 1:rayCount
% XX(1) = X1( i );
% YY(1) = Y1( i );
% ZZ(1) = Z1( i );
% XX(2) = X2( i );
% YY(2) = Y2( i );
% ZZ(2) = Z2( i );
% plot3( XX, YY, ZZ )
% end
%
% scatter3( X3, Y3, Z3, '.', 'r' ), xlabel ( 'X' ), ylabel ( 'Y' ), zlabel ( 'Z' ), xlim ( [ -xRange
xRange ] ), ylim ( [ -yRange yRange ] ), zlim ( [ zMINUSRange zPLUSRange ] );
% hold on
%
% for i = 1:rayCount
% XX(1) = X2( i );
% YY(1) = Y2( i );
% ZZ(1) = Z2( i );
% XX(2) = X3( i );
% YY(2) = Y3( i );
% ZZ(2) = Z3( i );
% plot3( XX, YY, ZZ )
% end
%
% scatter3( X4, Y4, Z4, '.', 'r' ), xlabel ( 'X' ), ylabel ( 'Y' ), zlabel ( 'Z' ), xlim ( [ -xRange
xRange ] ), ylim ( [ -yRange yRange ] ), zlim ( [ zMINUSRange zPLUSRange ] );
% hold on
%
% for i = 1:rayCount
% XX(1) = X3( i );
% YY(1) = Y3( i );
% ZZ(1) = Z3( i );

```

```

% XX(2) = X4(i);
% YY(2) = Y4(i);
% ZZ(2) = Z4(i);
% plot3( XX, YY, ZZ )
% end
%
% scatter3( X5, Y5, Z5, '.', 'r' ), xlabel ( 'X' ), ylabel ( 'Y' ), zlabel ( 'Z' ), xlim ( [ -xRange
xRange ] ), ylim ( [ -yRange yRange ] ), zlim ( [ zMINUSRange zPLUSRange ] );
% hold on
%
% for i = 1:rayCount
% XX(1) = X4(i);
% YY(1) = Y4(i);
% ZZ(1) = Z4(i);
% XX(2) = X5(i);
% YY(2) = Y5(i);
% ZZ(2) = Z5(i);
% plot3( XX, YY, ZZ )
% end
%
% scatter3( X6, Y6, Z6, '.', 'r' ), xlabel ( 'X' ), ylabel ( 'Y' ), zlabel ( 'Z' ), xlim ( [ -xRange
xRange ] ), ylim ( [ -yRange yRange ] ), zlim ( [ zMINUSRange zPLUSRange ] );
% hold on
% %
% for i = 1:rayCount
% XX(1) = X5(i);
% YY(1) = Y5(i);
% ZZ(1) = Z5(i);
% XX(2) = X6(i);
% YY(2) = Y6(i);
% ZZ(2) = Z6(i);
% plot3( XX, YY, ZZ )
% end
%
% scatter3( X7, Y7, Z7, '.', 'r' ), xlabel ( 'X' ), ylabel ( 'Y' ), zlabel ( 'Z' ), xlim ( [ -xRange
xRange ] ), ylim ( [ -yRange yRange ] ), zlim ( [ zMINUSRange zPLUSRange ] );
% hold on
%
% for i = 1:rayCount
% XX(1) = X6(i);
% YY(1) = Y6(i);
% ZZ(1) = Z6(i);
% XX(2) = X7(i);
% YY(2) = Y7(i);
% ZZ(2) = Z7(i);
% plot3( XX, YY, ZZ )

```

```

% end
%
% scatter3( X8, Y8, Z8, '.', 'r' ), xlabel ( 'X' ), ylabel ( 'Y' ), zlabel ( 'Z' ), xlim ( [ -xRange
xRange ] ), ylim ( [ -yRange yRange ] ), zlim ( [ zMINUSRange zPLUSRange ] );
% hold on
%
% for i = 1:rayCount
% XX(1) = X7( i );
% YY(1) = Y7( i );
% ZZ(1) = Z7( i );
% XX(2) = X8( i );
% YY(2) = Y8( i );
% ZZ(2) = Z8( i );
% plot3( XX, YY, ZZ)
% end
%
% scatter3( X9, Y9, Z9, '.', 'r' ), xlabel ( 'X' ), ylabel ( 'Y' ), zlabel ( 'Z' ), xlim ( [ -xRange
xRange ] ), ylim ( [ -yRange yRange ] ), zlim ( [ zMINUSRange zPLUSRange ] );
% hold on
%
% for i = 1:rayCount
% XX(1) = X8( i );
% YY(1) = Y8( i );
% ZZ(1) = Z8( i );
% XX(2) = X9( i );
% YY(2) = Y9( i );
% ZZ(2) = Z9( i );
% plot3( XX, YY, ZZ)
% end
% %
% scatter3( X10, Y10, Z10, '.', 'r' ), xlabel ( 'X' ), ylabel ( 'Y' ), zlabel ( 'Z' ), xlim ( [ -
xRange xRange ] ), ylim ( [ -yRange yRange ] ), zlim ( [zMINUSRange zPLUSRange ] )
;
% hold on
%
% for i = 1:rayCount
% XX(1) = X9( i );
% YY(1) = Y9( i );
% ZZ(1) = Z9( i );
% XX(2) = X10( i );
% YY(2) = Y10( i );
% ZZ(2) = Z10( i );
% plot3( XX, YY, ZZ)
% end
%

```

```

% scatter3( X11, Y11, Z11, '.', 'r' ), xlabel ( 'X' ), ylabel ( 'Y' ), zlabel ( 'Z' ), xlim ( [ -
xRange xRange ] ), ylim ( [ -yRange yRange ] ), zlim ( [zMINUSRange zPLUSRange ] )
;
% hold on
%
% for i = 1:rayCount
% XX(1) = X10(i);
% YY(1) = Y10(i);
% ZZ(1) = Z10(i);
% XX(2) = X11(i);
% YY(2) = Y11(i);
% ZZ(2) = Z11(i);
% plot3( XX, YY, ZZ)
% end
%
% scatter3( X12, Y12, Z12, '.', 'r' ), xlabel ( 'X' ), ylabel ( 'Y' ), zlabel ( 'Z' ), xlim ( [ -
xRange xRange ] ), ylim ( [ -yRange yRange ] ), zlim ( [zMINUSRange zPLUSRange ] )
;
% hold on
%
% for i = 1:rayCount
% XX(1) = X11(i);
% YY(1) = Y11(i);
% ZZ(1) = Z11(i);
% XX(2) = X12(i);
% YY(2) = Y12(i);
% ZZ(2) = Z12(i);
% plot3( XX, YY, ZZ)
% end
%

```

Appendix D: Fringe Intensity Matlab Code

```
clear;

clc;

close all;

factor = 10.0;

PixelHeight = 0.005 * factor; % The dimension of the pixel height (mm)

PixelWidth = 0.005 * factor; % The dimension of the pixel width (mm)

M = floor( 686 / factor ); % # of Rows or Height of Array

N = floor( 960 / factor ); % # of Columns or Width of Array

ITotal = zeros( 1000, 1000 );

Phi1 = xlsread('P1.xlsx'); % Import.xlsx file %

Phi2 = xlsread('P2.xlsx'); % Import.xlsx file %

Count1 = xlsread('Count1.xlsx'); % Import.xlsx file %

Count2 = xlsread('Count2.xlsx'); % Import.xlsx file %

% Intensity Calculation %

for m = 1 : M

    for n = 1 : N
```

```
ITotal( m, n ) = ( Count1( m, n )^2 + Count2( m, n )^2 + 2 * Count1( m, n ) *  
Count2( m, n ) * cos( Phi1( m, n ) - Phi2( m, n ) ) ) / 2.0;  
  
end  
  
end  
  
filename = 'Intensity.xlsx';  
  
xlswrite( filename, ITotal )
```